Electron Beam-Induced Fluorescence Localization
Implementation and Feasibility in Integrated Light-Electron Microscopy

Srinivasa Raja, A.

DOI
10.4233/uuid:245af2a3-b858-4c24-b2b9-b0104a021d3e

Publication date
2024

Document Version
Final published version

Citation (APA)
Srinivasa Raja, A. (2024). *Electron Beam-Induced Fluorescence Localization : Implementation and Feasibility in Integrated Light-Electron Microscopy* . [Dissertation (TU Delft), Delft University of Technology]. https://doi.org/10.4233/uuid:245af2a3-b858-4c24-b2b9-b0104a021d3e

Important note
To cite this publication, please use the final published version (if applicable).
Please check the document version above.

ELECTRON BEAM-INDUCED FLUORESCENCE LOCALIZATION

IMPLEMENTATION AND FEASIBILITY IN INTEGRATED LIGHT-ELECTRON MICROSCOPY

ELECTRON BEAM-INDUCED FLUORESCENCE LOCALIZATION

IMPLEMENTATION AND FEASIBILITY IN INTEGRATED LIGHT-ELECTRON MICROSCOPY

Proefschrift

ter verkrijging van de graad van doctor
aan de Technische Universiteit Delft,
op gezag van de Rector Magnificus Prof. dr. ir. T.H.J.J. van der Hagen,
voorzitter van het College voor Promoties,
in het openbaar te verdedigen op maandag 24 Juni 2024 om 12:30 uur

door

Aditi SRINIVASA RAJA

Master of Science in Optics & Photonics
Karlsruhe Institute of Technology, Germany & Aix-Marseille University, France
geboren te Chennai, India.

Dit proefschrift is goedgekeurd door de promotoren.

Samenstelling promotiecommissie:

Rector Magnificus	voorzitter
Em. prof. dr. ir. P. Kruit	Technische Universiteit Delft, promotor
Prof. dr. ir. J.P. Hoogenboom	Technische Universiteit Delft, promotor

Onafhankelijke leden:

Prof. dr. S. Stallinga	Technische Universiteit Delft
Prof. dr. N. Sommerdijk	Radboud Universitair Medisch Centrum
Prof. dr. P. Verkade	University of Bristol, UK
Dr. ir. S. Pereira	Technische Universiteit Delft
Dr. B.N.G. Giepmans	Universitair Medisch Centrum Groningen
Prof. dr. S. Otte	Technische Universiteit Delft, reservelid

CONTENTS

LIST OF ABBREVIATIONS

CL Cathodoluminescence

CLEM Correlative Light and Electron Microscopy

EM Electron Microscopy

eSRM Electron Beam-Induced Fluorescence Super-Resolution Microscopy

FM Fluorescence Microscopy

FOV Field Of View

ITO Indium Tin Oxide

RT Real-Time

ROI Region of Interest

SEM Scanning Electron Microscope/Microscopy

SR Super-Resolution

WF Wide-Field

SUMMARY

Correlative light-electron microscopy (CLEM) combines the molecular specificity of fluorescence microscopy (FM) with the ultrastructural resolution of electron microscopy (EM) to provide functional information in the context of structural detail. However, the correlation between the two modalities is hindered by a 100-fold resolution gap. Super-resolution fluorescence microscopy (SR-FM) has enabled more accurate correlation in CLEM, aided by advancements in sample preparation, bimodal registration, and optimized workflows. As the resolution of FM approaches that of EM, SR-FM becomes increasingly challenging due to the need for accurate registration and preservation of fluorophore properties during EM sample preparation. Integrated microscopes can remove the need for external alignment markers and achieve high registration accuracies, eliminating sample deformations and facilitating SR-CLEM. Yet, this necessitates samples that are simultaneously amenable to both FM and EM. While advancements are being made to engineer fixation-resistant fluorescent proteins and develop preparation protocols for preserving in-resin fluorescence, it is worth exploring the possibilities of the unified platform that integrated light-electron microscopy offers, especially for SR-FM. In cases where traditional SR-FM cannot be used due to vacuum or other limitations, the combination of both light and electron microscopy can provide valuable multi-modal information. It also enables central control of the experimental system, thereby offering new ways to manipulate, process, and interpret fluorescence data. This thesis aims to investigate and utilize fluorescent response to electron irradiation using integrated light-electron microscopy.

Chapter 2 presents an electron beam-induced fluorescence localization technique within the integrated CLEM framework (eSRM). This approach attempts sub-diffraction limited localization by locally modifying fluorescence with a focused electron beam and simultaneously recording the EM signals for inherently registered FM-EM images. We discuss the principle and implementation, show proof of principle results on three model systems, and report a localization accuracy of approximately 100nm. However, we encountered challenges related to variations in background fluorescence dependent on electron fluence, the influence of vacuum on fluorophore photophysical properties, and significant fluorescence bleaching beyond the expected electron interaction volume with the specimen. This necessitated further studies, which are discussed in the subsequent chapters.

Chapter 3 investigates the luminescence generated by electron beam irradiation in commonly utilized embedding epoxy and methacrylate resins across a broad electron fluence range, both with and without embedded biological materials. We report that all tested specimens exhibit similar patterns of luminescence when exposed to electron irradiation. The intensity of luminescence increases, followed by a shift in the spectrum towards longer wavelengths (redshifting), and finally, a bleaching effect as the electron

fluence rises. When the landing energy is increased, there is less scattering in the specimen, causing the luminescence profiles to move towards higher fluences. Further, the intensity of induced luminescence is influenced by the sample density. Regions with higher macromolecular density, such as the nucleus, show a higher intensity of induced luminescence. However, the differences between resins/biomaterials are minor. At low electron fluences, the spectral behavior of induced luminescence is concentrated in the blue-green wavelengths, allowing the use of red-emitting fluorophores to circumvent it. We also note that such pervasive electron-induced luminescence is an important parameter to account for while selecting probes for cathodoluminescence imaging and CLEM.

Chapter 4 studies the photon-yield and photobleaching performance of five common organic dyes (Atto 655, Atto 647N, Alexa 647, Alexa 594, and TRITC) under ambient and vacuum conditions. In vacuum conditions, TRITC was found to be the most efficient due to its improved photostability and a three-fold increase in total photon counts compared to ambient. Alexa 594 also displayed enhanced fluorescence under vacuum conditions because of reduced photobleaching. Both TRITC and Alexa 594 dyes showed increased blinking and reduced off times when placed in a vacuum. Our findings suggest that using a vacuum of approximately 10^{-6} mbar in combination with a vacuum-preferred dye can significantly improve fluorescence performance, expanding applications in integrated CLEM and presenting new possibilities for incorporating SR-FM.

Chapter 5 presents and explores electron beam-induced, long-range fluorescence bleaching in multiple model systems, namely bulk perylene diimide, plastic scintillators, and fluorescent polystyrene microspheres. Our investigation examines the phenomenon across various electron beam parameters, including deposited charge, currents, landing energies, applied stage bias, immersion, and field-free lens modes. We attribute such long-range bleaching to a field-driven charge carrier transport, where the bleaching range increases with the deposited charge and remains current independent for the measured currents between 13 to 800pA. The electron beam spot size influences the bleaching range, with lower currents having a larger bleaching range due to smaller spot sizes. Beyond 15nm, increasing spot sizes have minimal impact on the bleaching range. Applying a -500 V stage bias does not affect the bleaching range; secondary electrons from the chamber, beam deflection, and primary beam defocus also do not influence it. Our findings indicate that fluorescence bleaching may be predominantly driven by charging inside the insulator bulk. We further propose that our approach of using fluorescence to visualize charge dynamics inside insulators could present an experimental technique allowing for high spatial resolution in situ study of insulators under electron beam irradiation.

Lastly, Chapter 6 discusses the results of the previous three chapters and their relevance to eSRM implementation. We find that optimal conditions for eSRM involve using a red-emitting dye with high photon yield and low photobleaching, such as TRITC, coupled with a low electron fluence irradiation. Both factors also assist in mitigating electron-induced luminescence. A low-energy (1keV) electron beam with minimal charge deposition is recommended, potentially aiding in both bleaching fluorophores and generating real-time electron contrast. We also note that thin, uniformly flat samples are ideal. In the case of post-embedding immunolabeling sections, both epoxy and methacry-

late resins can be used since they exhibit similar electron-induced luminescence behavior. Importantly, we discuss that the long-range fluorescence bleaching caused by the electron beam can limit localization accuracy. This occurs because the fluorescent molecules may bleach before the intended electron exposure, leading to missed or inaccurately attributed localizations.As a result, this uncertainty can compromise the robustness of the reconstruction process, particularly when electron contrast is unavailable for cross-validation.

SAMENVATTING

Correlatieve licht-elektronenmicroscopie (CLEM) combineert de moleculaire specificiteit van fluorescentiemicroscopie (FM) met de ultrastructurele resolutie van elektronenmicroscopie (EM) om functionele informatie te brengen in de context van structurele details. De correlatie tussen de twee modaliteiten wordt echter gehinderd door een 100-voudig verschil in resolutie. Super-resolutie fluorescentiemicroscopie (SR-FM) heeft een nauwkeurigere correlatie in CLEM mogelijk gemaakt, geholpen door verbeteringen in monstervoorbereiding, bimodale registratie en geoptimaliseerde workflows. Naarmate de resolutie van FM die van EM benadert, wordt SR-FM een steeds grotere uitdaging vanwege de noodzaak van nauwkeurige registratie en behoud van fluorofore eigenschappen tijdens EM monstervoorbereiding. Geïntegreerde microscopen kunnen de noodzaak voor externe uitlijningsmarkers wegnemen en een hoge registratieprecisie bereiken, waardoor monstervervormingen worden geëlimineerd en SR-CLEM wordt vergemakkelijkt. Hiervoor zijn echter monsters nodig die tegelijkertijd geschikt zijn voor FM en EM. Hoewel er vooruitgang wordt geboekt bij het ontwikkelen van fixatie-resistente fluorescerende eiwitten en het ontwikkelen van preparatieprotocollen voor het behoud van in-resin fluorescentie, is het de moeite waard om de mogelijkheden van het uniforme platform dat geïntegreerde licht-elektronenmicroscopie biedt te onderzoeken, met name voor SR-FM. In gevallen waar traditionele SR-FM niet gebruikt kan worden vanwege vacuüm of andere beperkingen, kan de combinatie van zowel licht- als elektronenmicroscopie waardevolle multimodale informatie opleveren. Het maakt ook centrale besturing van het experimentele systeem mogelijk en biedt daarmee nieuwe manieren om fluorescentiegegevens te manipuleren, verwerken en interpreteren. In dit proefschrift wordt de fluorescentierespons op elektronenbestraling onderzocht en gebruikt met geïntegreerde licht-elektronenmicroscopie.

Hoofdstuk 2 presenteert een elektronenbundel-geïnduceerde fluorescentie superresolutie microscopie in de geïntegreerde CLEM omgeving (eSRM). Deze benadering probeert subdiffractiebeperkte lokalisatie door fluorescentie lokaal te modificeren met een gefocusseerde elektronenbundel en tegelijkertijd de EM-signalen op te nemen voor inherent geregistreerde FM-EM beelden. We bespreken het principe en de implementatie, tonen proof-of-principle resultaten op drie modelsystemen en rapporteren een lokalisatienauwkeurigheid van ongeveer 100 nm. We stuitten echter op uitdagingen die te maken hadden met variaties in achtergrondfluorescentie afhankelijk van de elektronenflux, de invloed van vacuüm op de fotofysische eigenschappen van fluoroforen en aanzienlijke fluorescentieverbleking buiten het verwachte elektroneninteractievolume met het preparaat. Dit maakte verdere studies noodzakelijk, die in de volgende hoofdstukken worden besproken.

Hoofdstuk 3 onderzoekt de luminescentie gegenereerd door elektronenbundelstraling in veelgebruikte inbedmiddelen van epoxy- en methacrylaatharsen over een breed

elektronenfluxbereik, zowel met als zonder ingebed biologisch materiaal. We rapporteren dat alle geteste preparaten vergelijkbare luminescentiepatronen vertonen bij blootstelling aan elektronenbestraling. De intensiteit van de luminescentie neemt toe, gevolgd door een verschuiving in het spectrum naar langere golflengten (roodverschuiving) en ten slotte een blekingseffect naarmate de elektronenflux toeneemt. Wanneer de landingsenergie wordt verhoogd, is er minder verstrooiing in het preparaat, waardoor de luminescentieprofielen naar hogere fluenties verschuiven. Verder wordt de intensiteit van geïnduceerde luminescentie beïnvloed door de monsterdichtheid. Gebieden met een hogere macromoleculaire dichtheid, zoals de kern, vertonen een hogere intensiteit van geïnduceerde luminescentie. De verschillen tussen harsen/biomaterialen zijn echter klein. Bij lage elektronenfluxen is het spectrale gedrag van geïnduceerde luminescentie geconcentreerd in de blauwgroene golflengten, waardoor het gebruik van rood uitstralende fluoroforen mogelijk is om dit te omzeilen. We merken ook op dat een dergelijke alomtegenwoordige elektron-geïnduceerde luminescentie een belangrijke parameter is om rekening mee te houden bij het selecteren van probes voor kathodeluminescentie beeldvorming en CLEM.

Hoofdstuk 4 bestudeert het fotonrendement en de fotobleaching prestaties van vijf veelgebruikte organische kleurstoffen (Atto 655, Atto 647N, Alexa 647, Alexa 594 en TRITC) onder omgevings- en vacuümomstandigheden. In vacuümomstandigheden bleek TRITC het meest efficiënt te zijn vanwege de verbeterde fotostabiliteit en een 3-voudige toename in het totale aantal fotonen vergeleken met de omgevingstemperatuur. Alexa 594 vertoonde ook een verbeterde fluorescentie onder vacuümcondities vanwege de verminderde fotobleaching. Zowel TRITC als Alexa 594 kleurstoffen vertoonden meer knipperen en kortere off-tijden wanneer ze in een vacuüm werden geplaatst. Onze bevindingen suggereren dat het gebruik van een vacuüm van ongeveer 10^{-6} mbar in combinatie met een vacuüm geprefereerde kleurstof de fluorescentieprestaties aanzienlijk kan verbeteren, waardoor toepassingen in geïntegreerde CLEM worden uitgebreid en er nieuwe mogelijkheden ontstaan voor de integratie van super-resolutie FM.

Hoofdstuk 5 presenteert en onderzoekt door elektronenbundels geïnduceerde fluorescentiebleking over lange afstand in meerdere modelsystemen, namelijk peryleendimide in bulk, plastic scintillatoren en fluorescerende polystyreenmicrosferen. Ons onderzoek karakteriseert het fenomeen bij verschillende elektronenbundelparameters zoals afgezette lading, stromen, landingsenergieën, toegepaste stage bias, onderdompeling en veldvrije lensmodi. We schrijven dit bleken over grote afstanden toe aan een veldgedreven transport van ladingsdragers, waarbij het bereik van het bleken toeneemt met de neergeslagen lading en stroomonafhankelijk blijft voor de meetstromen tussen 13 en 800 nanoampère. De grootte van de elektronenspot beïnvloedt het bleekbereik, waarbij lagere stromen een groter bleekbereik hebben door kleinere spotgroottes. Voorbij de 15 nm hebben grotere spots geen significante invloed op het bleekbereik. De toepassing van een -500 V stage bias heeft geen invloed op het bleekbereik en secundaire elektronen uit de kamer, bundelafbuiging en defocus van de primaire bundel hebben er ook geen invloed op. Onze bevindingen geven aan dat bleken voornamelijk wordt aangedreven door oplading binnen de isolatorbulk. We stellen verder voor dat onze benadering van het gebruik van fluorescentie om om ladingsdynamica binnen isolatoren te visualiseren, een experimentele techniek zou kunnen zijn die een hoge ruimtelijke resolutie in

situ studie van isolatoren onder bestraling met elektronenbundels mogelijk maakt.

Tenslotte bespreekt hoofdstuk 6 de resultaten van de vorige drie hoofdstukken en hun relevantie voor de implementatie van eSRM. We vinden dat optimale condities voor eSRM het gebruik van een rood-emitterende kleurstof met hoge fotonopbrengst en lage fotobleaching, zoals TRITC, in combinatie met een lage elektronenflux bestraling. Beide factoren helpen ook bij het verminderen van elektron-geïnduceerde luminescentie. Een elektronenbundel met lage energie (1keV) en minimale ladingafzetting wordt aanbevolen, wat kan helpen bij zowel het bleken van fluoroforen als het genereren van real-time elektronencontrast. We merken ook op dat dunne, uniform vlakke monsters ideaal zijn. In het geval van post-embedding immunolabeling secties, kunnen zowel epoxy en methacrylaat harsen worden gebruikt, omdat ze soortgelijke elektron-geïnduceerde luminescentie gedrag. Belangrijk is dat we bespreken dat het verbleken van de fluorescentie over lange afstand door de elektronenbundel de nauwkeurigheid van de lokalisatie kan beperken. Dit komt doordat de fluoroforen kunnen bleken voordat de bedoelde elektronenbestraling plaatsvindt, wat kan resulteren in gemiste of verkeerd toegekende lokalisaties. Als gevolg hiervan kan deze onzekerheid de robuustheid van het reconstructieproces ondermijnen, vooral wanneer elektronencontrast niet beschikbaar is voor kruisvalidatie.

1

INTRODUCTION

Microscopy with either light (photons) or electrons has been the mainstay for visualizing life at the nanoscale. Historically, the emphasis was on the conjunction 'or' due to the distinct nature of these methods. Light microscopy offers non-destructive, cost-effective & accessible means to inspect live and wet samples. Particularly, Fluorescence Microscopy (FM) brings remarkable specificity in localizing targeted biomolecules. However, large fields of view and fast image acquisition are offset by diffraction-limited spatial resolution. Electron Microscopy (EM) directly maps the biological ultrastructure at nanometric resolution but is not molecule-specific and is performed in a vacuum – an environment incompatible with living and/or hydrated specimens.

Reasonably, no single imaging modality will have the answers to make sense of the workings of a (complex) biological system. Consequently, there is no 'silver bullet' imaging method. Instead, the choice is usually motivated by the chief biological question – for instance, if it's structural, the technique is EM, while if it requires molecular specificity, it may be FM. Despite this practical division, the underlying specimen functions as one integrated unit. Understanding this structure-function relationship has thus been an important endeavour [2]–[4] and Correlative Light and Electron Microscopy (CLEM) provides tools to do so.

CLEM combines FM and EM; for instance, to interpret FM's functional molecular expression or to find a region of interest in the context of EM's ultrastructural resolution. However, EM is not new - the first published attempt at correlating FM and EM dates to 1978 [5]. Still, meaningful correlation has been complicated, among other reasons, by the 100-fold resolution gap between the two modalities. Recent advances in circumventing the diffraction limit of light, mainly through clever manipulation of molecular fluorescence, have birthed a variety of Super-Resolution (SR) techniques. SR has driven FM resolution to <20nm, making it comparable to EM. This, coupled with concurrent

1

improvements in optimized sample preparation protocols for both FM and EM, accurate bimodal image registration, and sophisticated sample handling workflows that minimize specimen damage, has opened doors to broad CLEM applications.

1.1. CLEM WITH SUPER-RESOLUTION FLUORESCENCE

In many CLEM approaches, FM primarily serves as a tool to screen for regions of interest rapidly. These are then subjected to EM for structural analysis. Here, diffraction-limited FM is sufficient. However, in cases where the biological question requires precise molecular localization within the EM ultrastructure, one must turn to SR fluorescence. Besides, CLEM with SR (SR-CLEM) may even reveal formerly concealed information [6]–[8]. In some cases, SR-CLEM has the potential to act as fidelity checks for SR results, thereby generating highly reliable, correlated, and possibly even quantitative datasets [9]. When perfectly registered, near EM resolution in FM data can 'colorize' EM with true molecular context.

With SR-FM, the challenges in conventional diffraction-limited CLEM are taken a notch higher. First, there is lower tolerance for registration inaccuracies. Especially for SR-CLEM with optical resolutions of 10-20nm, approaching that of EM, SR-FM to EM registration accuracies must be comparable to or better than the super-resolution values. Further, there is increased demand for maintaining brightness and photo-stability of (potentially special) fluorophores and minimal to no background fluorescence, e.g., from embedding media used in EM. SR-FM in sequential CLEM has been demonstrated, although with stringent constraints [10]–[12]. Registration between FM and EM can be demanding and typically involves, if visible in both systems, (manual) feature identification and/or fiducial markers. Manual registration may be sufficient in diffraction-limited FM, especially with conspicuous structures like the mitochondria or lipid droplets [13]. Finder grids have also been employed [14] and are comparable to manual registration in their accuracies. Fiducial markers, such as nanoparticles, can provide registration accuracy well below 100nm [15], [16], possibly even 10nm, better than the resolution obtainable with superresolution fluorescence microscopy and suitable for SR-CLEM [12]. However, this carries the risk of insufficient fiducials in the ROI to correlate at the aimed-for accuracy. Also, when the fiducials are not embedded in the sample but, for instance, in the sample support, sample distortions occurring during intermediate sample preparation may compromise registration. Hence, for SR-CLEM to deliver its full potential, it remains a challenge to consistently obtain a highly accurate correlation throughout a sample without errors due to registration or post-FM sample deformation.

1.2. SR-FM IN INTEGRATED CLEM

Integrated microscopes can remove the need for external/manual alignment markers through automated registration procedures based on electron-induced signals detectable in the FM. High registration accuracies (down to ~5nm) are achievable and can be consistent across the sample. Inspection with an integrated microscope is also devoid of intermediate sample deformations, offering a unique platform for SR-CLEM. However,

this requires samples that are simultaneously amenable to both FM and EM. Further, they must maintain their SR properties after fixation, plastic embedding, and staining and in the vacuum environment of the integrated microscope. For SR-CLEM in sequential approaches, protocols have been developed to preserve fluorescence via weaker EM fixation and diluted staining at the expense of ultrastructural preservation [6], [11]. Fluorescence in standard fluorescence proteins such as the Green Fluorescent Protein and mCherry can also be preserved in-resin using optimized sample preparation [17]. Engineering fluorescent proteins that are more robust to osmium fixation and uranyl or other heavy metal staining, like the mEos4 and potentially the more recent hyperfolder fluorescent protein variants, [18] can facilitate SR-CLEM without compromise. However, while some fluorophores can survive in a vacuum [19], fluorescent proteins are more severely dependent on hydrated and oxygen-rich environments. In-resin SR-CLEM on fluorescent proteins in an integrated setup has been demonstrated using an environmental chamber in which water vapor can be introduced. These results indicated that standard Green and Yellow Fluorescent Protein show better blinking characteristics for SR-FM under the partial vacuum induced by injecting water vapor than in ambient conditions [8]. Both these avenues hold promise to meet the challenges in SR-CLEM but also call for further development to a broader palette of fluorescent molecules and preparation protocols. For instance, Eos4 [18] is successful in hydrophilic resins like the GMA, HM20, and variants. Recently, osmium-resistant fluorescent proteins for epoxy resins have also been found [20].

1.3. PROSPECTS FOR INTEGRATED (SR-)CLEM

With these initial demonstrations and further development en route, we may wonder what additional advantages integrated microscopy could offer. SR-FM is inherently a low-throughput method. Often, a single SR image may take several minutes to be acquired, and extensive post-processing is usually required. The characteristic large Field Of View (FOV) of a Wide-Field (WF) fluorescence image may subsequently be reduced due to the high numerical aperture objectives that are mandatory for superresolution fluorescence microscopy. Pre-screening with standard diffraction-limited FM is usually a prerequisite [9]. When performed sequentially, these time overheads easily add up, especially when additional processing steps such as fixation, staining, sample movement, and Region of Interest (ROI) retrieval are involved. Integrated systems, i.e., a setup where the light and electron microscope share the same sample chamber [21], can reduce the time costs and directly lend themselves towards automation and higher throughputs. Pre-programmed wide-field FM detection, in combination with array tomography, could also be viable, with superresolution fluorescence microscopy being performed only in dedicated regions. Note that direct electron excitation or Cathodoluminescence (CL)[22], [23] has been explored but is impossible for organic molecules due to rapid molecular degradation, or bleaching, under electron irradiation. Also, detection of atom-specific X-ray luminescence generated during electron irradiation can 'colorize' EM images [24], but suffers from low throughput and still lacks the broad database of molecule-specific probes that are available for (SR-)FM. Especially integrated systems that can concurrently image the sample by EM and FM can potentially add to the palette of SR tech-

1

niques. Particularly for dyes where vacuum or other constraints preclude conventional superresolution fluorescence microscopy, the availability of simultaneous multi-modal information and the ability to control the experimental system centrally with both light and electrons may offer innovative ways of manipulating, processing, and interpreting fluorescence data. To that end, this thesis investigates and utilizes fluorescent response to electron irradiation using integrated light-electron microscopy.

1.4. THESIS OUTLINE

Chapter 2 presents a novel super-resolution approach (called Electron Beam-Induced Fluorescence Super-Resolution Microscopy (eSRM)) to selectively exploit electron beam-induced fluorescence bleaching to generate optical super-resolution within the boundaries of an integrated CLEM system. We present the principle of eSRM, its implementation, and proof of principle results on synthetic and biological model systems. Three further directions are explored. While these significantly influence eSRM, they remain independent studies and serve to answer the following questions. (1) Chapter 3: Besides bleaching, are there secondary luminescent effects to electron irradiation of organic material (resins, embedded tissues, whole cells), and is this material dependent? (2) Chapter 4: How does the vacuum environment in integrated microscopy impact fluorophore signals? (3) Chapter 5: How localized is electron beam bleaching in insulating fluorescent specimens? If a focused electron beam can cause 'localized' bleaching & generate SR, as in Chapter 2, can the reverse be utilized, i.e., can fluorophores report on electron-scattering in insulators? Finally, Chapter 6 addresses the consequences to eSRM from the phenomena observed in Chapters 3 to 5.

BIBLIOGRAPHY

[1] P. Verkade and L. Collinson, *Correlative Imaging: Focusing on the Future*. John Wiley & Sons, 2019.

[2] B. N. Giepmans, T. J. Deerinck, B. L. Smarr, Y. Z. Jones, and M. H. Ellisman, "Correlated light and electron microscopic imaging of multiple endogenous proteins using quantum dots", *Nature methods*, vol. 2, no. 10, pp. 743–749, 2005.

[3] Y. S. Bykov, M. Cortese, J. A. Briggs, and R. Bartenschlager, "Correlative light and electron microscopy methods for the study of virus–cell interactions", *FEBS letters*, vol. 590, no. 13, pp. 1877–1895, 2016.

[4] M. R. Russell, T. R. Lerner, J. J. Burden, *et al.*, "3d correlative light and electron microscopy of cultured cells using serial blockface scanning electron microscopy", *Journal of Cell Science*, vol. 130, no. 1, pp. 278–291, 2017.

[5] C. Klein and S. Van Noorden, "Use of immunocytochemical staining of somatostatin for correlative light and electron microscopic investigation of d cells in the pancreatic islet of xiphophorus helleri h.(teleostei)", *Cell and Tissue Research*, vol. 194, no. 3, pp. 399–404, 1978.

[6] B. G. Kopek, M. G. Paez-Segala, G. Shtengel, *et al.*, "Diverse protocols for correlative super-resolution fluorescence imaging and electron microscopy of chemically fixed samples", *Nature Protocols*, vol. 12, no. 5, pp. 916–946, 2017, ISSN: 17502799. DOI: 10.1038/nprot.2017.017. [Online]. Available: http://dx.doi.org/10.1038/nprot.2017.017.

[7] A. Löschberger, C. Franke, G. Krohne, S. van de Linde, and M. Sauer, "Correlative super-resolution fluorescence and electron microscopy of the nuclear pore complex with molecular resolution.", *Journal of cell science*, vol. 127, no. Pt 20, pp. 4351–5, 2014, ISSN: 1477-9137. DOI: 10.1242/jcs.156620. [Online]. Available: http://jcs.biologists.org/content/early/2014/08/18/jcs.156620.abstract.

[8] C. J. Peddie, M. C. Domart, X. Snetkov, *et al.*, "Correlative super-resolution fluorescence and electron microscopy using conventional fluorescent proteins in vacuo", *Journal of Structural Biology*, vol. 199, no. 2, pp. 120–131, 2017, ISSN: 10958657. DOI: 10.1016/j.jsb.2017.05.013. [Online]. Available: http://dx.doi.org/10.1016/j.jsb.2017.05.013.

[9] M. Hauser, M. Wojcik, D. Kim, M. Mahmoudi, W. Li, and K. Xu, "Correlative Super-Resolution Microscopy: New Dimensions and New Opportunities", *Chemical Reviews*, vol. 117, no. 11, pp. 7428–7456, 2017, ISSN: 15206890. DOI: 10.1021/acs.chemrev.6b00604.

1

[10] E. Betzig, G. H. Patterson, R. Sougrat, *et al.*, "Imaging intracellular fluorescent proteins at nanometer resolution.", *Science (New York, N.Y.)*, vol. 313, no. 2006, pp. 1642–1645, 2006, ISSN: 0036-8075. DOI: 10.1126/science.1127344.

[11] S. Watanabe, A. Punge, G. Hollopeter, *et al.*, "Protein localization in electron micrographs using fluorescence nanoscopy.", *Nature methods*, vol. 8, no. 1, pp. 80–4, 2011, ISSN: 1548-7105. DOI: 10.1038/nmeth.1537. [Online]. Available: http://www.pubmedcentral.nih.gov/articlerender.fcgi?artid=3059187&tool=pmcentrez&rendertype=abstract.

[12] B. G. Kopek, G. Shtengel, J. B. Grimm, D. A. Clayton, and H. F. Hess, "Correlative Photoactivated Localization and Scanning Electron Microscopy", *PLoS ONE*, vol. 8, no. 10, 2013, ISSN: 19326203. DOI: 10.1371/journal.pone.0077209.

[13] S. M. Markert, V. Bauer, T. S. Muenz, *et al.*, "3D subcellular localization with super-resolution array tomography on ultrathin sections of various species", *Methods in Cell Biology*, vol. 140, pp. 21–47, 2017, ISSN: 0091679X. DOI: 10.1016/bs.mcb.2017.03.004.

[14] C. Spiegelhalter, V. Tosch, D. Hentsch, *et al.*, "From dynamic live cell imaging to 3d ultrastructure: Novel integrated methods for high pressure freezing and correlative light-electron microscopy", *PloS one*, vol. 5, no. 2, e9014, 2010.

[15] W. Kukulski, M. Schorb, S. Welsch, A. Picco, M. Kaksonen, and J. A. Briggs, "Correlated fluorescence and 3d electron microscopy with high sensitivity and spatial precision", *Journal of Cell Biology*, vol. 192, no. 1, pp. 111–119, 2011.

[16] P. Schellenberger, R. Kaufmann, C. A. Siebert, C. Hagen, H. Wodrich, and K. Grünewald, "High-precision correlative fluorescence and electron cryo microscopy using two independent alignment markers", *Ultramicroscopy*, vol. 143, pp. 41–51, 2014.

[17] C. J. Peddie, K. Blight, E. Wilson, *et al.*, "Correlative and integrated light and electron microscopy of in-resin gfp fluorescence, used to localise diacylglycerol in mammalian cells", *Ultramicroscopy*, vol. 143, pp. 3–14, 2014.

[18] M. G. Paez-Segala, M. G. Sun, G. Shtengel, *et al.*, "Fixation-resistant photoactivatable fluorescent proteins for CLEM.", *Nature methods*, 2015, ISSN: 1548-7105. DOI: 10.1038/nmeth.3225.

[19] M. A. Karreman, A. V. Agronskaia, E. G. Van Donselaar, *et al.*, "Optimizing immunolabeling for correlative fluorescence and electron microscopy on a single specimen", *Journal of Structural Biology*, vol. 180, pp. 382–386, 2012. DOI: 10.1016/j.jsb.2012.09.002.

[20] I. Tanida, J. Yamaguchi, S. Kakuta, and Y. Uchiyama, "Osmium-resistant fluorescent proteins and in-resin correlative light-electron microscopy of epon-embedded mammalian cultured cells", in *Fluorescent Proteins: Methods and Protocols*, Springer, 2022, pp. 287–297.

[21] S. den Hoedt, A. Effting, and M. Haring, "The secom platform: An integrated clem solution", *Microscopy and Microanalysis*, vol. 20, no. S3, pp. 1006–1007, 2014.

[22] D. R. Glenn, H. Zhang, N. Kasthuri, *et al.*, "Correlative light and electron microscopy using cathodoluminescence from nanoparticles with distinguishable colours", *Scientific Reports*, vol. 2, pp. 1–6, 2012, ISSN: 20452322. DOI: 10.1038/srep00865.

[23] M. W. Garming, I. G. C. Weppelman, P. De Boer, *et al.*, "Nanoparticle discrimination based on wavelength and lifetime-multiplexed cathodoluminescence microscopy", *Nanoscale*, vol. 9, no. 34, pp. 12 727–12 734, 2017.

[24] N. M. Pirozzi, J. P. Hoogenboom, and B. N. Giepmans, "Colorem: Analytical electron microscopy for element-guided identification and imaging of the building blocks of life", *Histochemistry and cell biology*, vol. 150, pp. 509–520, 2018.

1

2

ELECTRON BEAM INDUCED FLUORESCENCE SUPER-RESOLUTION IN INTEGRATED CLEM

2.1. INTRODUCTION

Correlative Light and Electron Microscopy (CLEM) combines the excellent ultrastructural resolution of electron microscopy (EM) with the molecular specificity of fluorescence microscopy (FM). This can help study the structure-function relationship of subcellular biological structures, select functionally relevant fluorescent regions for subsequent EM, and/or precisely localize molecules in the underlying ultrastructure. However, such a (precise) correlation is thwarted by the 100-fold resolution gap between EM & FM. Bridging this gap is critical to leverage the potential of CLEM for molecular-level localization, correlation, and interpretation.

Fluorescence super-resolution (SR) techniques can bring FM resolution closer to EM, and to that end, several SR approaches have been applied in CLEM (SR-CLEM). However, SR often requires specific fluorophores with properties such as blinking, photoswitching, or bright and photostable fluorescence, which EM sample preparation routines may compromise. Also, low background levels may be needed, which can be particularly difficult in resin embedding media due to auto-fluorescence. Thus, EM sample preparation needs specific optimization to preserve fluorescence and reduce auto-fluorescence while ensuring sufficient EM contrast and ultrastructural preservation [1].

Registration between EM and FM presents a challenge for SR-CLEM as the registration accuracy should ideally be smaller than the SR values. Fiducial markers, such as

nanoparticles, can be identified in FM and EM and are used for registering the fluorescent ROI to the corresponding EM images. Although fiducial marker-based registration can achieve sub-100nm accuracy for SR-CLEM, the accuracy may vary based on the number of fiducials present.

Directly using the scanning, focused electron beam to generate a signal to localize fluorescent molecules would be preferred over SR-CLEM as it would naturally bring both near-EM resolution and registration to the other EM signals. Electron beam excited luminescence, or CL, has been pursued for years [2], but organic fluorophores bleach under electron beam irradiation before visible CL signal can be detected [3], [4]. Stable CL nanoparticle probes have been developed, but only a few are in the sub-100nm range and have been demonstrated to work in EM-prepared biological tissues. [5].

We reasoned that the bleaching generally induced by the focused electron beam could also be used advantageously for localization, provided fluorescence can be excited and monitored during electron beam scanning. This is feasible with an integrated microscope that combines a fluorescence and an electron microscope in one system. We have previously reported an integrated microscope in which the FM and EM fields of view overlap, removing the need for sample movement and eliminating potential distortions and contamination due to intermediate sample preparation [6]. Also, FM-EM can be registered at consistent, high accuracies (<50nm) anywhere on the sample by detecting CL signals from the underlying support [7]. Admittedly, sample preparation for integrated CLEM is complex as the specimen must be readily optimized for both FM and EM under dry, vacuum conditions. However, several protocols have been developed over the years to overcome these issues [8]. A similar integrated setup has been employed for SR-CLEM using Green and Yellow Fluorescent Proteins. An adapted in-resin fluorescence preserving preparation protocol and introducing partial water vapor aided signal detection and induced blinking. This necessitates an environmental scanning electron microscope (eScanning Electron Microscope/Microscopy (SEM)) and pressure cycling the chamber to alternate between EM and FM imaging. Also, SR using spontaneously blinking Alexa Fluor 647 has been demonstrated in an integrated system with transmission electron microscopy. However, identifying bright fluorophores for ultra-high vacuum and ensuring consistent blinking behavior remains challenging [9].

Here, we present a new technique for SR-CLEM. We attempt SR localization by using the integrated microscope (SEM – FM combination) to directly detect the confined loss in fluorescence due to bleaching induced by the scanning electron beam. We term this technique eSRM. A key advantage of eSRM is its compatibility with conventional fluorophores. Most, if not all, organic fluorophores bleach under electron irradiation. Secondly, since the electron beam is the probe that manipulates fluorescence, it inherently permits direct registration of EM-FM images.

This chapter details the eSRM principle and its implementation and demonstrates proof of principle results on fluorescent model systems with ~100nm localization. Furthermore, we extend its feasibility to biological samples such as TRITC-labeled microtubules and immunolabeled rat pancreas tissue sections. Finally, we discuss eSRM's achievable resolution, techniques for optimizing input parameters, inherent limitations, and considerations for further development.

2.2. PRINCIPLE

After EM imaging, fluorescence inspection of CLEM samples reveals significant bleaching in the scanned area as shown in Figure 2.1. This remains true even when the imaged area is reduced to that covered by a spot-sized (<10nm spot) focused electron beam.
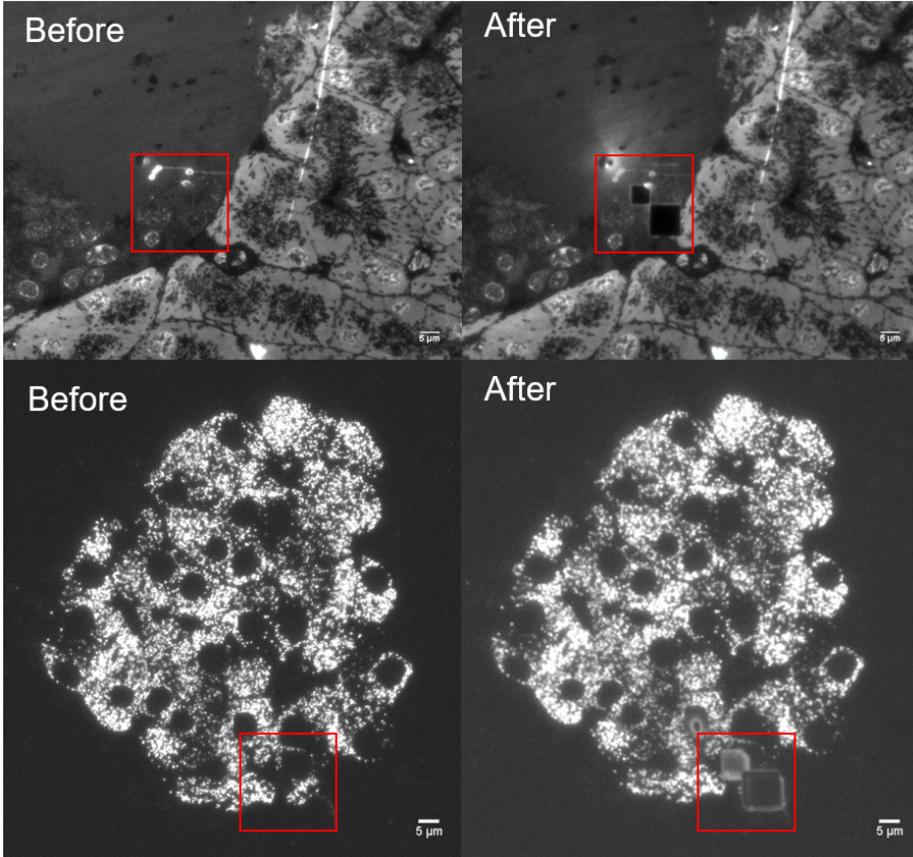

Figure 2.1: **Electron beam exposure leads to fluorescence bleaching in the exposed area.** Top: 80nm thick exocrine rat pancreas tissue section, DNA stained with Hoechst. Bottom: Similar endocrine tissue labeled with Alexa Fluor 594 for insulin. The left and right panels depict before and after electron beam scanning within the red-boxed areas. Three types of electron beam exposures are illustrated: (from upper left to lower right corner) focused stationary spot, small and large area irradiation. After panels show resulting fluorescence loss. Imaging was performed using a 0.95NA objective.

The eSRM approach uses a focused electron beam to scan through a fluorescently labeled sample. The FM and EM can observe the specimen simultaneously since they share the same sample stage. Any decay in fluorescence signal due to electron beam-induced bleaching can be monitored in situ and attributed to the known electron beam position at the time. This way, an SR image is reconstructed, inherently registered to the EM image, when aligned and compensated for FM-EM drift. This principle is illustrated

in Figure 2.2.

We choose to implement eSRM with a WF FM as this provides a context for select-
ing the SR area and is generally a faster and easier scheme. The implementation details
are described as follows. We start with aligning FM-EM, deciding electron scan strat-
egy based on camera integration time and pixel dimensions, compensating for FM-EM
drift during measurement, and registering eSRM with high-resolution EM images. In this
section, we will use a sample of isolated, single fluorescent microspheres to illustrate the
concept. We will introduce a time-sharing scan approach that expands eSRM to larger
fields of view. We will then discuss the scenario where multiple fluorescent features are
present within a diffraction-limited area. We will explain how we track the electron beam
within the FM image frame to monitor fluorescence decay in a diffraction-limited area
surrounding the beam scan position. Finally, we will demonstrate how we reconstruct
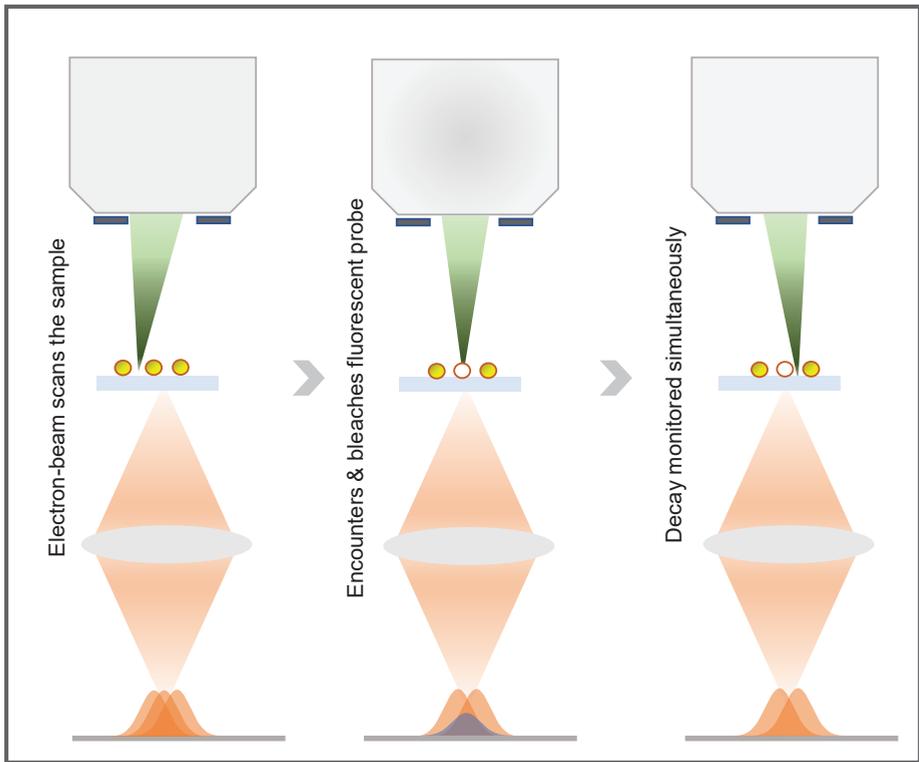the SR image from the WF image sequence.

Figure 2.2: **Illustration of the eSRM principle.** A sample with active fluorescence labels (depicted as yellow
spheres) is mounted in an integrated fluorescence (orange) and electron (green) microscope. Each label on
the pixelated fluorescence detector (at the bottom) gives a Gaussian-shaped image; the sum of all illuminated
labels constitutes the diffraction-limited image. Electron exposure of a specific label during scanning leads
to bleaching of that label (middle panel), resulting in a localized decay in fluorescence on the detector. Syn-
chronization of the detected fluorescence loss with the electron beam's instantaneous position allows sub-
diffraction limit localization of the fluorescence label.

2.3. EXPERIMENTAL METHODS

eSRM REQUIREMENTS AND EXPERIMENTAL PARAMETERS

The first set of parameters to be selected are those of the electron microscope. An electron beam is focused to a few nm-sized probe on the specimen surface. The impinging beam then scatters through the specimen, losing its energy in the process. Assuming an ideal fluorescent sample with zero background signals and a perfect detector, the fundamental resolution limit is a) defined by the scattering extent of the primary electron beam in the material; b) which can, in turn, degrade fluorophores and cause bleaching. Fluorophores are primarily damaged by low-energy secondary electrons [10], making the spread of secondaries a reasonable first approximation for the smallest damage radius in the specimen. Knowledge of such electron-matter interaction is primarily derived from Monte-Carlo-based simulators. The repeated random sampling approach is well suited to the inherently random nature of electron scattering, provided appropriate probability distributions describe the underlying physics. To that end, we look to CASINO v2.3, a popular, freely available Monte-Carlo-based simulator [11]. Although it models only the primary electrons and their elastic collisions, it is worth noting that the spatial distribution of secondary electrons and those generated by backscattered electrons (SE2s) is similar. The mean free path length of secondary electrons is limited to several angstroms up to a few nanometers [12], [13]. The objective is to minimize the interaction volume so that both secondary and backscattered electrons emerge from a shallow area surrounding the beam incidence. Choosing a landing energy of 1keV yields a penetration depth of approximately 40nm with an axial electron spread that is contained within 50nm. This is shown in Figure 5.2 within Chapter 4. If the penetration depth sufficiently covers the fluorescent structure, it should cause bleaching, resulting in an apparent loss of fluorescence. This is the case in the microsphere samples and the rat pancreas tissue sections used in these experiments. The latter has fluorophores only labeled in the section's top ~20nm. Choosing low voltages like 1-3keV prevents charge build-up in insulating, weakly scattering (uncoated) biological specimens. To mitigate charging, SEM specimens are typically coated with metal or stained with heavy metals to improve image contrast and offer sufficient conductivity for charge dissipation. This is not an option for integrated CLEM, as fluorophores quench in close proximity to metals[14]–[16]. When imaging at low voltages, the probe size increases, but for eSRM purposes, the decrease in interaction volume and charging with decreasing voltage is a more useful metric. On the other hand, lowering voltages compromises image resolution as we aim to collect scattered electron signals simultaneously to stitch a real-time correlated SEM image. In practice, the ultra-high resolution (UHR) mode is used for sharper probe sizes during EM imaging.

Next, we address electron fluence. The choice of current and dwell time influences the electron dose rate. For the sake of simplicity, we optimize only for the total dose by changing the current and dwell time as necessary. This must be high enough to completely bleach the fluorescent structure, generate sufficient electron signal for EM imaging, and yet not cause specimen charging. For the samples analyzed in this study, the current typically ranged from 6 to 50pA, with the lowest being 3pA in the Thermo Scientific Verios SEM. The dwell time ranged from 50 to 300μs. To determine the dose, we

utilized the dwell time since it can be adjusted in smaller increments than the current and does not necessitate recalibration of the electron beam, such as focus, astigmatism, or lens alignment. Furthermore, increasing the dwell time has a minor effect on through-put as our acquisition is limited by the camera integration time.

We have discussed the key EM variables and will move on to the eSRM sample. Ideal eSRM samples have bright, photostable fluorescence and sufficient EM contrast with ul-trastructural preservation for proper correlation. Preferably, the sample thickness should be thin; ultra-thin resin-embedded tissue sections can be as thin as 50-80nm. Thin sections significantly reduce non-specific autofluorescence background from embed-ded resin, particularly in post-embedding immunolabeling, where labeled fluorophores are confined to the surface. EM imaging of 50nm sections is challenging due to low EM signals despite higher electron doses, but this is not the case for the ~80nm thick resin sections used here. Fluorescence emanates from the entire volume for whole, non-continuous structures like microtubule filaments or microspheres. In this case, the sam-ple thickness should ideally be less than 50nm to ensure low landing energies (0.5 to 1.5 keV) can sufficiently bleach the entire structure.

Fluorophore choice is primarily dictated by their brightness and photostability un-der SEM vacuum pressures (10^{-6} mbar). Lack of oxygen and water vapor are not con-ducive for fluorescent proteins, but some conventional fluorophores still show suffi-cient fluorescence in vacuum for integrated CLEM (Chapter 4 discusses this in detail). For eSRM, the higher the signal photons, the better the decay detection accuracy when wholly bleached. The absence of oxygen typically slows photobleaching, allowing longer acquisition times.

Integrated Light-Electron Microscope

We employed an FEI (now Thermo Scientific) Verios SEM retrofitted with a wide-field epi-fluorescence optical microscope, the SECOM from Delmic B.V.

Figure 2.3: **Photographs of the integrated fluorescence and electron microscope system.** Left: Verios SEM (vacuum chamber visible on the right) retrofitted with a wide-field optical microscope. The sample stage is at-tached to the blue-boxed vacuum door with a fluorescence camera. Right: A closer view of the sample stage (x-y movement) and the optical objective stage (z-movement) below this. A representative sample on an Indium Tin Oxide (ITO)-coated glass coverslip is shown, mounted on an Aluminium sample holder ring.

The Verios SEM's standard stage and door were replaced with a custom stage that allowed mounting an optical microscope objective underneath [17]. This was followed by a beam-directing mirror that guided the light either into/out of the vacuum chamber. The detection path consisted of a dichroic mirror (FF01-432/515/595/730-25, Semrock), quad-band emission filter (FF01-432/515/595/730-25, Semrock), and tube lens on to a water-cooled Andor 4.2 sCMOS camera. The dichroic mirror and emission filter can be substituted when necessary. We used the Omicron LED Hub with four wavelength channels at 405/488/555/633 nm for illumination. The optical beam was channeled via a 0.5 NA, 1mm SMA-ended multi-mode optical fiber. Before crossing the vacuum window, the illumination path consisted of a collimator, aperture-stop, field lens, beam steering mirrors, and the dichroic mirror. The rest of the wide-field ensemble was housed outside the vacuum in a light-shielded enclosure except for the objective. Photographs of the experimental setup are shown in Figure 2.3. The rest of the SEM, including the electron column, remained in native factory condition.

eSRM SAMPLE

The eSRM sample was placed on ITO coated glass coverslips (Nr. 1 thickness, Materion Balzers Optics). The ITO is a conductive and optically transparent coating that dissipates charge from the electron beam. The standard ITO-glass coverslip is square with a 22mm edge length, 17μm thickness, and a 10nm ITO layer on one side. The ITO-glass coverslips were attached to a metal (aluminium) sample holder ring (via conductive carbon tape) with the ITO side in contact with the metal. This setup was mounted on the sample stage, with an additional metal hook (not shown in Figure 2.3), to ensure the sample was grounded through the stage to the central microscope ground.

FLUORESCENT POLYSTYRENE MICROSPHERES

A stock solution of 10μL of fluorescent polystyrene microspheres (Dragon Green, Bangs Laboratories, 1% solid suspension) was diluted with 300μL of deionized water. Spin-coating 25μL of this solution onto ITO-coated glass coverslips at 3000 rpm for 120 seconds resulted in an even, sparsely distributed single-bead layer where individual sources and diffraction-limited clusters could be distinguished.

MICROTUBULES

Microtubules were polymerized from 32μM TRITC-labeled tubulin (Cytoskeleton Inc.) for 20 minutes at 37°C in MRB80 buffer (80mM K-Pipes pH 6.9, 4mM MgCl2, 1mM EGTA) supplemented with 1mM GTP and 25% glycerol. Taxol was added to a final concentration of 250μM to stabilize microtubules and incubated for 10 more minutes. Microtubules were sedimented in Beckman Airfuge for 3 minutes at 14 psi, and the pellet was resuspended in MRB80 buffer containing 40μM taxol. Microtubules were diluted in a ratio of 1:30 in the same buffer for deposition on ITO-coated glass coverslips, and 100μL were spread on the ITO surface with a pipette tip. After 5 minutes, unbound microtubules were washed with 300μL of MRB80, and the coverslip was immediately immersed in -20°C methanol for 10 minutes and then air-dried at room temperature.

RAT PANCREAS TISSUE SECTIONS

Rat pancreas tissue from a BB rat [18] was fixed in 4% paraformaldehyde and 0.1% glu-taraldehyde, followed by post-fixation with 1% osmium tetroxide/1.5% potassium ferro-cyanide. The tissue was embedded in EPON resin (SERVA). Ultra-thin (80nm) sections were cut and collected on ITO-coated glass coverslips (Optics Balzers AG). The sections were incubated with a guinea pig anti-insulin antibody (Invitrogen lot # SE2381176) fol-lowed by a biotinylated donkey anti-guinea pig secondary antibody (Jackson-IR lot # 137834) and finally a streptavidin-conjugated Alexa 594 (Jackson-IR lot # 016-580- 084). Subsequently, the samples were counterstained with Hoechst 33258 (Sigma-Aldrich lot # BCBF4593v).

CLEM AND eSRM IMAGING

FM images were acquired with a 1.25 NA, water-immersion 60X Nikon objective and im-aged on a 6.5μm pixel size Andor 4.2 sCMOS detector (Oxford Instruments). Water im-mersion in the SEM is achieved by using vacuum-compatible water-like immersion oil (ZEISS Immersol® W 2010). 470nm (microspheres) and 555nm excitation wavelengths (TRITC-labeled tubulin in the microtubules and Alexa Fluor 594-labeled insulin gran-ules in the rat pancreas tissue) were used. The same dichroic and emission filters were retained as in Section 2.3. The camera exposure time was 2 seconds, and the image resolution was 2048×2048. EM settings were 1keV landing energy, 6pA current (micro-spheres) and 13pA (microtubules, rat pancreas tissue sections) with a 300μs dwell time. SR pixels were defined with a ~108 nm pixel size. Each SR pixel was subdivided into 4×4 subpixels of ~27nm. EM–stage drift correction was performed after every FM acquisi-tion. EM scanning is controlled via the external output port through Odemis (Delmic GUI). This limits the minimum electron beam dwell time to 800ns and restricts beam blanking. To mitigate the latter, the electron beam is parked several micrometers away relative to the top-left coordinate of the ROI. SR pixels, subpixels, and the acquisition procedure are explained in the following section. All measurements were conducted in ultra high resolution mode, with a working distance of ~5mm and a chamber pressure of ~10^{-6} mbar.

PROCEDURE

eSRM relies on three factors: causing a localized fluorescence decay, detecting the decay over the background floor, and accurately attributing the electron beam position to the associated decay for SR reconstruction. The latter depends on having exact electron beam positional information in the fluorescence FOV, which depends on two factors. (A) The EM and FM spatial coordinates must be mapped a priori to each other to drive and scan the electron beam through the optical ROI. (B) This registration must be maintained throughout the experiment, especially in the case of drift in either EM or FM modality or both. (A) will be discussed below, and (B) is addressed under 'Drift Estimation and Correction.'

At the start of the experiment, EM and FM coordinate systems are registered, as ex-plained in [7]. While the integrated SEM and FM share a common stage and are axially

aligned to within 1-2µm, their coordinate systems are independent and thus need to be accurately registered. This is accomplished using cathodoluminescence (CL) pointers, which, in principle, allow for alignment accuracy in the sub-10nm range. For CL alignment, the user should switch the electron beam to high landing energy (e.g., 30 keV) and current (0.2nA) in spot mode. This generates a bright CL spot that can be tracked in the optical FOV. Through stage movements, the CL spot is positioned in the FOV center. At this stage, the user can decrease the landing energy (typically needed for eSRM) and current. This will result in a smaller CL spot, making it easier to center it more accurately. Doing so aligns the EM-FM optical axes on a coarse level, although this alignment is limited by the diffraction-limited CL intensity spread. Each CL pointer's radial symmetry enables the localization of its center in FM coordinates. This process is repeated on a 5 x 5 matrix of CL pointers for fine alignment. An affine transformation matrix (translation, shear, and rotation) connecting the EM and FM coordinate frames is then calculated. The location accuracy of the electron beam in the FM reference frame is linked to the uncertainty in the centroid fitting at the CL marker phase. We note that non-linear distortions may also be corrected for [7], but are not conducted here and may cause slight registration shifts in the CLEM overlay images. The transformation matrix is stored in the image metadata and applied to the Odemis (SECOM user interface) viewer, which adjusts the rendered FM image for an accurate 'visual' correlation. Since this transformation is not physically applied to either modality, the electron beam and light objective remain shifted with respect to each other at this sub-FM pixel level. However, the relative shift is known. It is now possible to perform standard WF and SEM imaging with a high-accuracy overlay that can be directly visualized.

Once the CL alignment is done, a specific ROI is selected for SR imaging by using the CL-registered overlay image. Additionally, a second region is also chosen for drift correction. Before any electron beam scanning, a WF image, also known as frame zero, is captured. This image will be the control image against which the first bleaching event will be compared. Thereafter, the eSRM implementation can be divided into three blocks.

1. The fluorescent ROI is systematically scanned with a focused electron beam.

2. After each electron beam scan, WF-FM images of the ROI are recorded to monitor fluorescence bleaching. This series of FM images will serve as the basis for SR reconstruction.

3. Reference images are routinely obtained in the SEM and FM framework to apply real-time and a posteriori drift correction.

4. Steps 1-3, except FM drift correction, are automated via a Python script.

Electron Beam Scan Strategy

The spot size of the focused electron beam (~3nm at 1keV, ultra high resolution mode) is ~40-50x times smaller than the pixel size in the WF-FM image (~108nm at 40x magnification and 6.5µm pixel size). The time between two consecutive scan positions is mainly limited by the integration time of the optical camera (~500ms). For efficiency, we subdivide the ROI into smaller square regions called SR pixels, analogous to a traditional

2

scan resolution. The user is free to set this. The theoretical minimum SR pixel size is the electron beam probe size. Practically, this is limited by a combination of the set horizontal field width and digital-to-analog converter resolution of the acquisition system. The scan pattern can be a classic raster, following a saw tooth waveform. This means it travels from left to right, meanders to the second row of SR pixels (left), and continues until the last SR pixel on the bottom right. For each SR pixel, a WF-FM image has to be recorded for SR reconstruction after that SR pixel has been scanned. Under a raster scan, the number of FM images to be taken for a given FOV goes with the square of the pixels. Assuming the ROI covers an area of $2 \times 2\ \mu m^2$ and the SR pixel size is set at 100nm, the ROI must then be scanned in 100nm steps and divided into 20×20 SR pixels. Correspondingly, an SR pixel size of 10nm will result in 200×200 SR pixels, which amounts to 40,000 FM images and an acquisition time exceeding 5.5 hours. At such time scales, the fluorophores are long photo-bleached. Throughput and associated photo-bleaching can be improved by more advanced scan strategies, which are discussed under 'Time-Shared Scan Strategy.'

Electron beam scanning of the SR pixel is done by further subdividing the SR pixel into smaller regions called sub-SR pixels. The electron beam thus has a secondary scan resolution of sub-SR pixels within the larger SR pixel. This ensures that a nearly equal electron dose is applied across the entire SR pixel space. Irrespective of the SR pixel subscanning, the localization ceiling is set at the original SR value because FM inspection occurs only after an SR pixel has been fully covered by electron scanning. The resulting scan strategy is illustrated in Figure 2.6. Note that the scattered electron signals from SR pixel scanning are also recorded. At the acquisition end, these will be used to stitch together a Real-Time (RT)-SEM image.

WF- FM Imaging

In the case of a raster scan, after every SR pixel is EM scanned, the fluorescence intensity of the entire FOV (inclusive of ROI and edges) is recorded. For the previous example of a 100nm SR pixel size and a $2 \times 2\ \mu m^2$ ROI, a total of 400 FM images will be taken. The illumination power and camera exposure time per frame is the same as that used for 'frame 0' or the FM control image before electron beam scanning. The resulting data is an FM time series of the ROI where every image reports the effects of the electron beam scan on a single SR pixel.

Drift Estimation and Correction

While the EM-FM systems are aligned before eSRM, there is a possibility of drift and misalignment during acquisition, particularly in large FOV measurements, which take longer. Since these modalities (FM or EM or both) can independently move with respect to each other, their monitoring and correction play a significant role in eSRM implementation and post-processing. Drift can occur in two frameworks, both of which will impact the accuracy of SR reconstruction. The electron beam may drift with time, causing unintended scanning of SR regions on the ROI. Alternatively, the FM stage may drift in the x-y plane, resulting in similar consequences. The FM stage may also defocus in the axial direction, which can hamper image reconstruction. eSRM drift monitoring and correction

occur at two levels, real-time and post-acquisition. On-the-fly corrections are applied to electron beam movements (1), while FM image movements (2) can be adjusted after acquisition.

- (1a) Electron beam drift is periodically monitored by scanning a sample region outside the ROI and then corrected by phase correlation to the initial EM image. As mentioned earlier, this anchor region is reserved for drift correction. The anchor region's relative position to the eSRM ROI is a control value. In the case of electron beam drift, the anchor region moves. The measured shift is compensated by deflecting the electron beam. This real-time correction links the electron beam and sample stage. The motion of either the sample or the electron beam can be brought back to the starting alignment by shifting the electron beam. However, restoring the electron beam via phase correlation requires an overlapping region between the anchor region and the measured image. Large movements or jumps can hence not be corrected.

- (1b) Stage drift shifts both EM and FM positions. Following (1a), the electron beam can be reverted to the right ROI position. The EM scan can proceed as intended. However, the FOV seen in the FM images remains shifted.

- (2a) Drift in the FM image series is fixed after acquisition via phase correlation. This ensures the same SR pixel is monitored before and after electron beam scanning.

Additionally, when the excitation LED is off, the camera continues acquisition during electron beam scanning. The rationale is to record the generated CL signals as the electron beam scans the SR pixels. Localizing the CL spot gives the EM position on the FM FOV and, therefore, real-time information on registration. However, this method depends on the landing energy, current, and dwell time used for eSRM and, in some cases, may not be sufficient to generate and/or collect sufficient CL photons. For instance, the energy of the electrons has to be high enough to pass through both the tissue and the conductive coating of the glass. Energy levels at or below 1keV cannot penetrate the ITO layer on the coverslips used in these experiments.

IMAGE ANALYSIS

After completing the eSRM procedure, we analyze the acquired FM image series to detect local fluorescence decay or bleaching. Decay detection is sensitive to background signals and signal fluctuations. It makes sense to measure decays only within the area of maximal electron beam-induced effects, given the known electron beam position on the ROI. The eSRM image analysis algorithm on simulated data is depicted in Figure 2.4.

Figure 2.4A shows a simulated FM image series of the ROI post eSRM implementation. The WF ROI is a 10×10 pixel region. The SR pixel size is equal to the detector/image pixel size. Hence, every image pixel on the camera is indicative of one SR pixel. This assumption is feasible as the EM-FM coordinate systems have been aligned previously. The electron beam is raster scanned through the ROI. The first FM image – 'Frame 0,' is

a 'before' image before any electron beam impingement. Frame 1 is an FM image taken after electron beam scanning of the first pixel on the top-left, Frame 2 is the second pixel, and so on, following the electron beam scan pattern. A total of 100 FM image frames are recorded for the ROI.
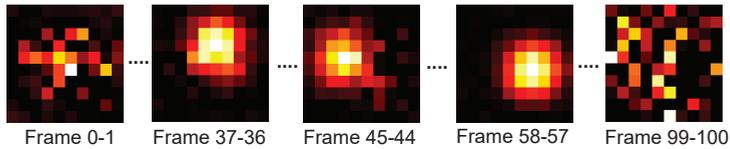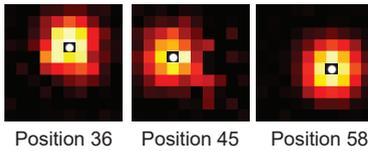
Image Analysis Algorithm
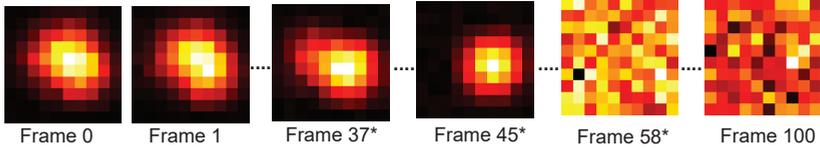
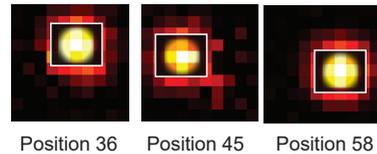Figure 2.4: **Illustration of the eSRM image analysis algorithm using a series of *simulated* FM images.** [A] First, a wide-field fluorescence image (WF-FM) is captured prior to commencing electron beam scanning (Frame 0), followed by a new image capture after scanning an SR pixel. [B] Consecutive image frames are subtracted to obtain the 'difference' images, where bright features correspond to bleached fluorescence positions. [C] The electron beam position can be determined from the image and thus SR pixel order, followed by [D] a Gaussian-weighte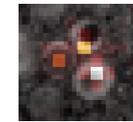d intensity allocation on these positions to assign [E] an intensity to the respective SR pixel. [F] The electron signal obtained in concert with SR pixel scanning renders a low magnification, real-time (RT-SEM) image, which is registered with and has the same resolution as the reconstructed SR image in [E]. This RT-SEM image can be used to register [G], a high-resolution SEM obtained afterward. [H] Overlay of WF-FM and [I] SR reconstruction with the real-time SEM image.

From Figure 2.4A, the effects of electron beam-induced decay can be detected. Frames 37, 45, and 58 show changes to the FM image and are marked by an asterisk (*). Following frame 58, all fluorescence in the ROI has been completely bleached. Firstly, frame subtraction is performed with each frame in the image series subtracted from the following

2

(i.e., n-(n+1)). As one looks for decay, this should result in bright spots in some frames and noise fluctuations in the rest (Figure 2.4B). The frames with bright spots correspond to electron beam locations that bleached a fluorescent structure. In Figure 2.4C, this corresponds to real-time electron beam locations in SR pixels 36, 44, and 57. Frame averaging can be performed [19] before feature detection to enhance detection and reduce noise. This is especially relevant considering image subtraction adds the noise uncertainties of both images. A Gaussian weighted square matrix (0.75σ) is applied with the central element at the concerned SR pixel (electron beam location). The matrix mean is then rendered as the resultant intensity in the central SR pixel. The process continues across all SR pixels, generating an SR image. The real-time SEM (RT-SEM) image is a stitched montage of electron signals detected at every SR pixel scanning. Note that the SR pixel consists of multiple RT-SEM pixels but has a lower resolution than the final SEM image. It offers the advantage of instantaneous and perfectly registered electron beam information. If electron contrast were available, this would serve as a ground-truth image against which SR localization and its accuracy may be cross-checked. For CLEM, the SR image is resolution matched with the RT-SEM image (either directly or via upsampling) and is rendered as an overlay (Figure 2.4I). A similar overlay can be performed for the final SEM-SR and SEM-WF images.

TIME-SHARED SCAN STRATEGY

Raster scanning of a square fluorescent ROI results in n^2 FM images, where n is the number of SR pixels in either the x or y dimension. Although the scanning strategy is straightforward, it has a few disadvantages. Firstly, it takes a lot of time to acquire a complete dataset. With wide-field detection, the same ROI is illuminated n^2 times, thus quickening photobleaching. Secondly, larger frame numbers become computationally heavier as the whole ROI is stored in the FM image series. Furthermore, longer acquisition times increase the probability of drift and misalignment. Thus, a classic raster scan is well-suited mainly for small ROIs of brightly fluorescent samples. To mitigate this issue, a time-shared scan strategy is implemented. The concept is illustrated in Figure 2.5.

Figure 2.5 shows a WF-FM image ROI. This contains 36 SR pixels across the x and y axes (n=36). These SR pixels are grouped in square grids (g), where g^2 is the total number of grids. The image is divided into 81 grids, each with 16 SR pixels. The top left pixel of each grid is scanned first and shown in white. An example grid is highlighted in green at the top left.

The scan movement is still a raster, but the grid determines the scan pitch. Figure 2.5 has a grid-pitch of 4 SR pixels. Grid pitch refers to the spacing between two consecutive grids or white SR pixels in Figure 2.5. A sufficiently large grid pitch assumes that subsequently scanned SR pixels do not influence each other and can be visualized as independent localization events. Thus, the bleaching effects of multiple well-spaced SR pixels can be analyzed from a single FM image.

The scanning process involves the following steps. After scanning each grid's leftmost/first pixel, an FM image of the entire ROI is taken. This is Frame 1 of the FM image stack, and it will reflect the electron scan consequences of g^2 SR pixels. The electron beam scanning continues to the second SR pixel of each grid, and once done, Frame 2

of the FM image is recorded. The process continues until the last SR pixel of each grid is scanned. Such time-shared scanning reduces the FM frames to $(n/g)^2$ and, proportionally, the photobleaching effects. The extent of this advantage depends on how few SR pixels (n) are within a single grid (g).

For Figure 2.5, raster scanning gives n^2 or 1296 FM frames. With a 500ms exposure time per frame, the total time taken (without electron beam overheads) is 648 seconds. Dividing the ROI by nine grids (g=9) with 4 SR pixels each, the FM frames are $(n/g)^2$, i.e., 16 frames, and the duration is 8 seconds, which is an 81-fold (g^2) improvement.
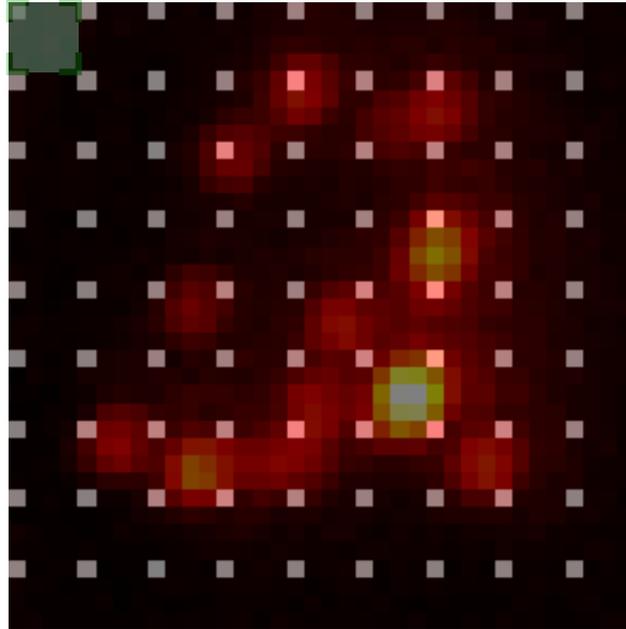

Figure 2.5: **Illustration of the time-shared approach for eSRM scanning.** The SR pixels of the ROI are grouped into square grids. A sample grid highlighted in green is displayed in the top-left corner. The initial or leftmost pixel of each grid is presented in white. These pixels are scanned by the electron beam first, following a raster pattern. Subsequently, the FM image displays the bleaching effects of the first pixels of each grid. The procedure continues until all SR pixels in each grid are scanned, reducing the total number of FM frames to the amount of SR pixels in a single grid.

2.4. RESULTS AND DISCUSSION

2.4.1. FLUORESCENT POLYSTYRENE MICROSPHERES

A simple way to evaluate the eSRM technique is to apply it on a monolayer of ~50nm fluorescent polystyrene microspheres or beads (Dragon Green, Bangs Laboratories). The Dragon Green variants have an excitation and emission spectrum centered at 480 and 520 nm, respectively. These microspheres are small (below the diffraction limit), uniformly sized (~40-60nm), and internally dyed to offer bright, photostable fluorescence.

Furthermore, they possess electron contrast for EM visibility, providing a ground truth for comparing both SR reconstruction and EM-FM registration.

Single Bead Localization

For an ideal diffraction-limited WF microscope, the Abbe limit is approximately 210 nm at an emission wavelength of 520 nm and with a numerical aperture of 1.25. Figure 2.6A shows the WF image of a single fluorescent bead. With a set SR pixel size of 108nm, the effective detector pixel size and the SR pixel size are nearly equal, with an error that depends on the accuracy of the affine CL alignment between EM and FM and the uncorrected (non-linear) distortions in either system. The dashed rectangular inset depicts the ROI (~0.5μm) over which the electron beam is scanned to localize the microsphere. The scan order within this ROI is a raster scan from top-left to bottom right (see number inset in Figure 2.6G). The image series in Figure 2.6G reflects the raw WF images as the electron beam scans each SR pixel. Both Figure 2.6G frame zero, before electron beam impingement, and frame 1, after scanning the first SR pixel, still preserve the microspheres' fluorescence. This indicates that the first SR pixel does not encompass the bead. Frame 2, however, records an apparent loss in fluorescence, merely leaving behind the intensity of an adjacent fluorescent structure. As scanning continues, frame 3 persists with negligible intensity change. The average ROI intensity is seen in Figure 2.6H. As SR pixel 2 or frame 2 is scanned, fluorescence bleaching is observed as the average intensity falls to background levels. The fluorescent bead is thus localized in SR pixel number 2, with an accuracy defined by the SR pixel size at ~100nm. A weighted Gaussian matrix analysis (see Section 2.3), with a 0.75 σ, is used for SR reconstruction and is rendered in Figure 2.6B.

The through lens detector records scattered secondary electron signals at each electron beam impact. These signals are then stitched together to form an RT-SEM image as shown in Figure 2.6C. The RT-SEM image includes the sub-pixels that are scanned within each SR pixel. Each SR pixel contains 16 sub-pixels, resulting in four times more pixels in the RT-SEM for the same ROI. A higher-resolution EM image taken post-eSRM is shown in 8D. Both SEM images, which use secondary electron contrast, clearly depict the surface topography of a spherical 3D bead structure. The edges of the structure appear brighter due to increased surface availability for electron escape, while the central dark region is primarily caused by positive charging [13]. The overlay with the RT-SEM image is intended to show the fidelity of the SR reconstruction. Figure 2.6E and Figure 2.6F represent WF and SR overlays with the RT-SEM image. Both CLEM overlays follow the same image registration protocol as earlier, without additional corrections. Figure 2.6F reveals the microspheres contained in the localized SR pixel.

Multiple Bead localization

A similar polystyrene bead sample with a larger FOV is subjected to eSRM implementation. Figure 2.7A shows multiple fluorescent microspheres of varying separation distances in a ∼ 3μm FOV. The electron beam and optical parameters are identical to the previous single-bead localization. Furthermore, the set SR pixel size is retained at 108nm to match the detector pixel size. Figure 2.7B markedly shows fluorescence localization
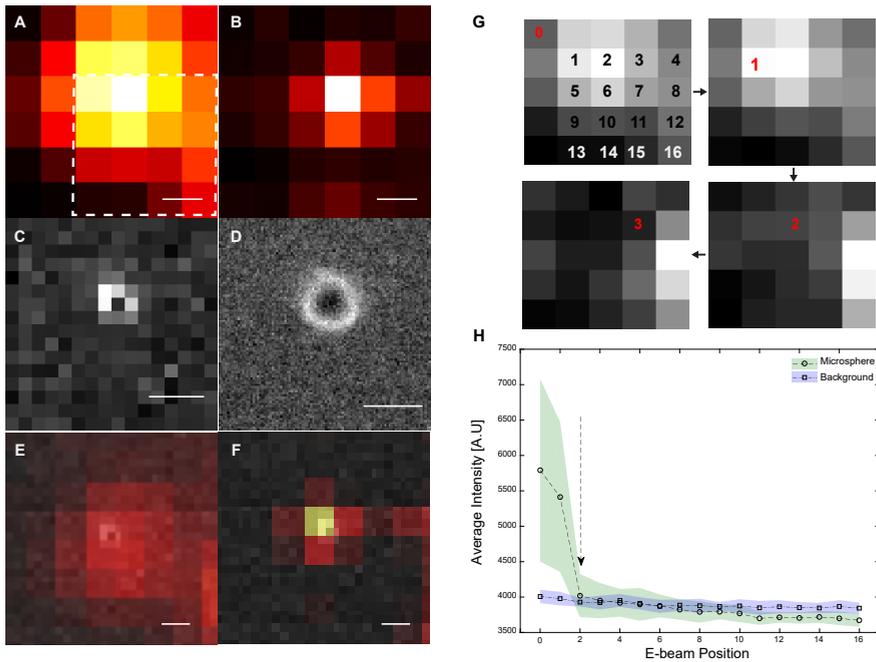
2

Figure 2.6: **eSRM localization of a single 50nm fluorescent polystyrene microsphere.** (A) WF-FM image of the bead. (B) eSRM reconstruction result. (C) RT-SEM image acquired during eSRM scanning. (D) Final high-resolution SEM image. (E) Overlay of WF-FM and (F) eSRM with the RT-SEM image. (G) A sequence of FM image frames was acquired during the eSRM procedure (shown here in grayscale). Upper left is frame 0 acquired before starting electron beam scanning, with the scanning order of SR pixels indicated in numbers. Other panels show FM frames 1, 2, and 3 in a clockwise direction, respectively. A clear drop in bead fluorescence is observed between frames 1 and 2. (H) Average ROI and background fluorescence intensity for the 16 FM image frames also clearly show the loss of microsphere fluorescence after scanning SR pixel 2. Scalebars in (A-F) are 125nm.

improvement, while Figure 2.7F reveals the SR accuracy in the context of the underlying ultrastructure. Having so far discussed only localization, the bright, clustered regions in Figure 2.7A help address the question of feature separation or 'resolution.' The SEM image in Figure 2.7D shows two sub-diffractive bead twins separated by ~132 and 100 nm, respectively. These structures are unresolvable in the WF image Figure 2.7A, but the distinction becomes more apparent in the eSRM image Figure 2.7. The scan strategy in this ROI followed the time-sharing approach presented earlier.

IMAGE INTERPRETATION AND REGISTRATION ACCURACY

Figure 2.7B achieves better fluorescence localization and resolves previously hidden features as seen in the SEM image Figure 2.7D. The time-sharing scan strategy implemented in Figure 2.5 distributes the electron exposures into square grids. The grids in the stitched RT-SEM image are discerned in Figure 2.7C. Figure 2.7C also shows that the bead twins are each contained within a single grid. However, the lower bead within each set is

2
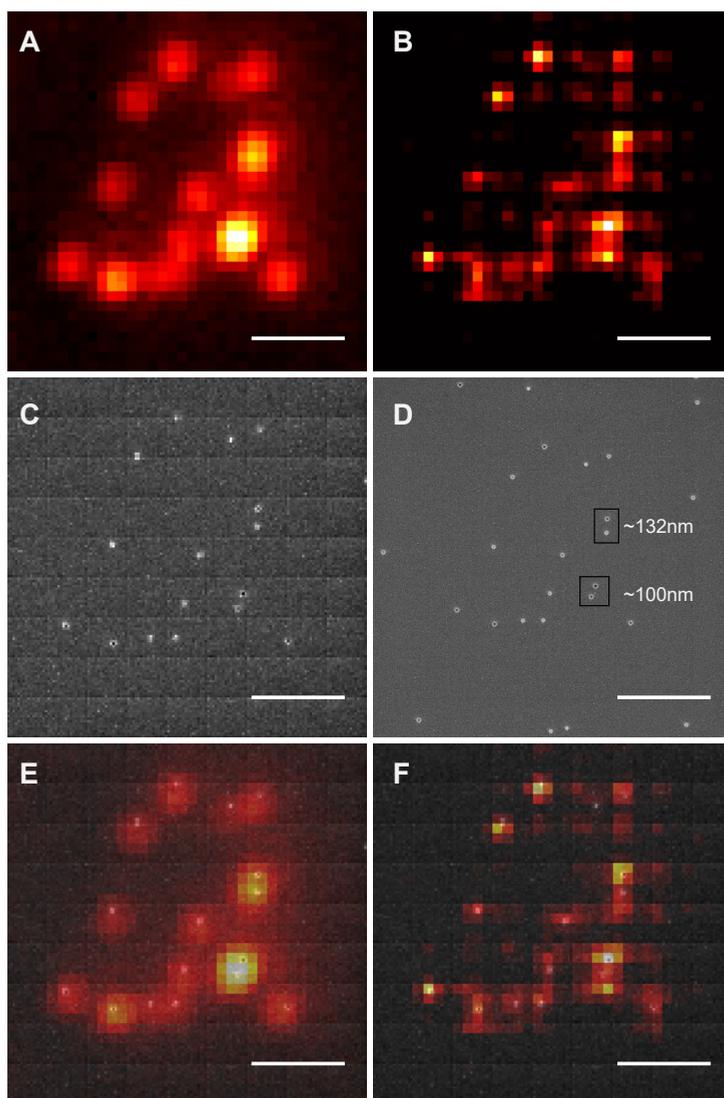
Figure 2.7: **~100nm eSRM localization accuracy on multiple fluorescent polystyrene microspheres.** (A) WF-FM image of a selected region of the microspheres sample, (B) eSRM super-resolution reconstruction of the same area, (C) RT-SEM image, (D) post-eSRM high-resolution SEM image, and (E) the final CLEM overlay with the WF and (F) SR image. Inset (D) depicts sub-diffractive bead twins' center-to-center spacing. Scale bar 1μm.

physically closer to the adjacent grid below. Scanning the bottom grid also causes the lower bead to bleach. This intensity loss is then attributed to the bottom grid's SR pixels, thereby misidentifying their real position. Moreover, the overlay images in Figure 2.7F reveal that while the sub-diffractive bead twins are resolved, their spacing is larger than the ground truth, resulting in positional inaccuracy. The fundamental reason behind

these mislocalizations is that the electron beam bleaching effects exceed the scanned area, spilling into neighboring regions. Delocalized bleaching, in the context of eSRM, causes a fluorescent feature to be bleached before its original location. This 'prior' position is dependent on the scanning scheme. A feature approached from the left may be mislocalized to the left of the original structure. We have observed this delocalized bleaching to depend on factors like primary electron beam energy and total deposited charge and to be particularly present in highly insulating materials. In Chapter 5, we will address this phenomenon in more detail.

A reliable, real-time ground truth image in the microspheres' sample is a huge advantage in critically evaluating and optimizing the eSRM technique. The artifacts are thus known and measurable, which allows for better estimation in biological samples that do not necessarily have electron contrast.

2.4.2. MICROTUBULES

The microsphere samples were an ideal model system for demonstrating the eSRM technique due to their significantly high fluorescent intensity and electron contrast. The logical next step is to move to biological model systems. In that regard, long, continuous structures like actin filaments and microtubules are often advantageously used as SR test samples [20]. Therefore, we also implemented the time-shared eSRM technique on extracted TRITC-labelled microtubules deposited on ITO-coated glass coverslips.

The microtubules have an outer diameter of ~25nm, with varying lengths in the order of tens of microns. We employed the maximum possible labeling density by using 100% labeled tubulin, which supports bright fluorescence signals. This is crucial to maintain sufficient signal under the vacuum conditions required for the SEM. Vacuum environments reduce fluorescence signals, particularly the lack of hydration and oxygen. They are especially deleterious to fluorescent proteins, with weak photo-physical properties [21]. TRITC has consistently shown superior performance in a vacuum under experimental conditions of others (Karreman, Agronskaia, Van Donselaar, *et al.* [22] and in our work [see Chapter 4]. It is thus a preferred dye for eSRM. Signal-to-background ratio requirements become critical when biological samples are considered. Unlike the polystyrene microspheres that are saturated with dye molecules, specifically labeled biological structures can accommodate only a few molecules per receptor site. Any loss in signal, either by weak labeling or dye incompatibility with vacuum, may result in suboptimal conditions for eSRM. Figure 2.8B shows the eSRM image of a ~5μm FOV of TRITC labelled microtubules. The SR image reports the thicker regions along the filaments as an increased intensity signal, which corresponds to the brighter areas in the WF image 2.8A. The meandering shape of the longitudinal microtubule on the bottom-left, as seen in 2.8D, is ably reproduced in the SR reconstruction compared to the WF image. A better visualization can be seen in the overlay image 2.8F. As seen in some SR methods applied on microtubules [20], there are patches of fluorescently weak/empty areas in the SR image. The SEM ground truth does not support these, as the continuous structure persists. The EM contrast of the microtubule structure is thus not representative of its labeling. In the absence of such information, assessing SR reconstruction fidelity in terms of false positives or negatives is not trivial. The filament's minuscule breaks, as

seen in Figure 2.8D, are smaller than the SR pixel size and should not contribute to the lack of localization. Further, 100% labeled tubulin should have multiple dye molecules per an SR pixel size of ~100nm. The high background levels in Figure 2.8A may hinder the detection of feeble decays. This is already seen in Figure 2.8B, where multiple low-intensity reconstructions exist across the entire FOV. It then appears that a combination of delocalized scattering and weak decay detection causes the intermediate loss of reconstructions along the microtubule.
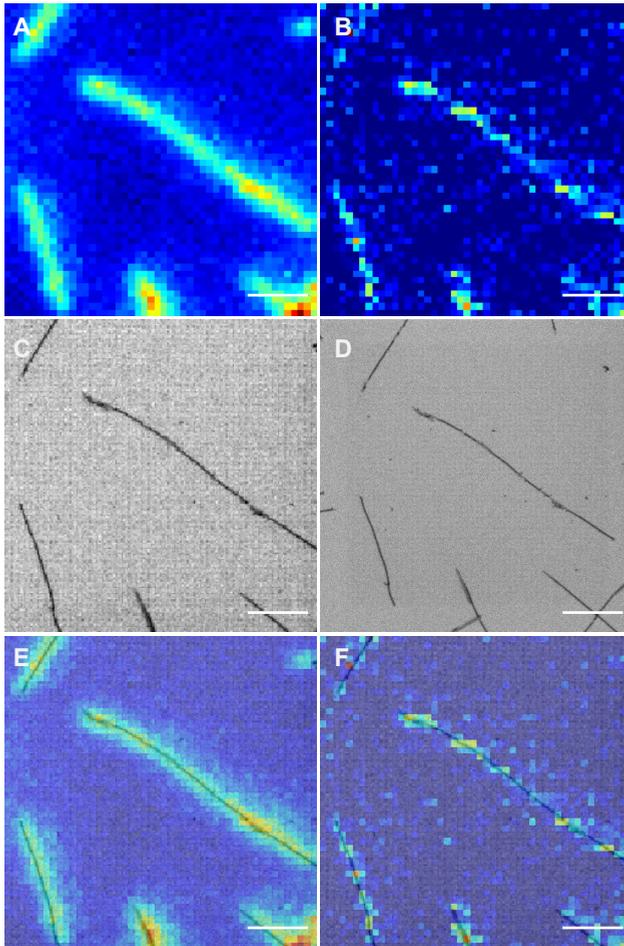

Figure 2.8: **eSRM applied to fluorescently labeled microtubules.** (A) WF fluorescence image of microtubules labeled with TRITC. (B) eSRM, (C) RT-SEM, and (D) high-resolution SEM images of the same microtubules, (E) WF, and (F) eSRM fluorescence overlays with RT-SEM, respectively. Scale bar 1μm.

2.4.3. RAT PANCREAS TISSUE SECTIONS

Integrated CLEM samples are predominantly resin-embedded or Tokuyasu-based tissue sections [23]. While whole cells are also standard integrated CLEM samples [24], the advantages of CLEM overlays are best observed in the fine ultrastructural detail and molecular-specific fluorescence offered by (ultra)thin tissue sections. We implement eSRM on 80nm thick rat pancreas tissue sections, which are insulin-labeled with Alexa Fluor 594 and counterstained with Hoechst via post-embedding immunolabeling. The scan strategy follows the time-sharing principle.

Following the same optical parameters, the SR pixel size is defined at 108nm while the electron beam is set at a landing energy of 1keV and 13pA current. Resin-embedded tissue sections have more stringent sample preparation requirements to retain fluorescence while maintaining sufficient ultrastructural preservation. However, insulin granules are relatively large, sub-diffractive quasi-spherical structures (~200 nm in diameter) that can be densely labeled with fluorophores. This offers moderate signal-to-background conditions in a sample with relatively high background signals from autofluorescence in the embedding resin. The implementation of dense labeling presents a promising solution to mitigate intensity losses that may arise within a vacuum environment. Additionally, insulin granules have native electron contrast, which helps to cross-check both SR accuracy and labeling efficiency. Figure 2.9(A) shows the WF image of a few diffraction-limited clusters of insulin granules. The SR size of ~100nm is not required considering the average insulin diameter at over 200nm, but the increased sampling helps differentiate local brightness differences. From Figure 2.9B, it is clear that eSRM separates the insulin cluster into three bright parts and a few weaker intensity blobs. Some of the latter can be excluded as noise peaks if they do not correspond to a fluorescent feature in the WF image. This is clear in the overlay images Figure 2.9D&E. Figure 2.9E shows a reasonable correlation between individual insulin granules and the SR reconstructions. Yet, a non-uniform intensity spread is observed per granule. The WF images in Figure 2.9A also indicate that the fluorescence spread across each insulin granule does not directly correspond to the underlying spherical basis, which has differing spatial extent and intensity. This can come from labeling variations on insulin. However, knowing the tendency for delocalized bleaching described above in the SR images, the first fidelity check is to map the eSRM bright spots to the corresponding time-shared grid positions to look for scanning biases. This is observed at the initial electron beam scan position (Figure 2.9F). Since the scan pattern is from left to right, reconstructions appear strongest towards the left of the grid. Also, for a structure positioned at the respective grid bottom, the electron beam is designed to scan it towards the end of the acquisition. However, since it is physically closer to the top of the bottom-adjacent grid, it might be (partially) bleached earlier. An added challenge is that electron beam irradiation of resin-embedded specimens shows increasing background luminescence during eSRM scanning. This is characterized in [25] and in Chapter 3. As the fluorophores labeled via post-embedding immunolabelling get bleached on the surface get bleached, the underlying biospecimen plus resin matrix starts to luminesce. This signal initially emits in the blue spectrum. With increasing deposited charge, it grows in intensity as it spectrally enlarges and red-shift[25], see Chapter 3. Thus, eSRM decay detection must compete with a time-varying increasing background as scanning progresses. Key ways
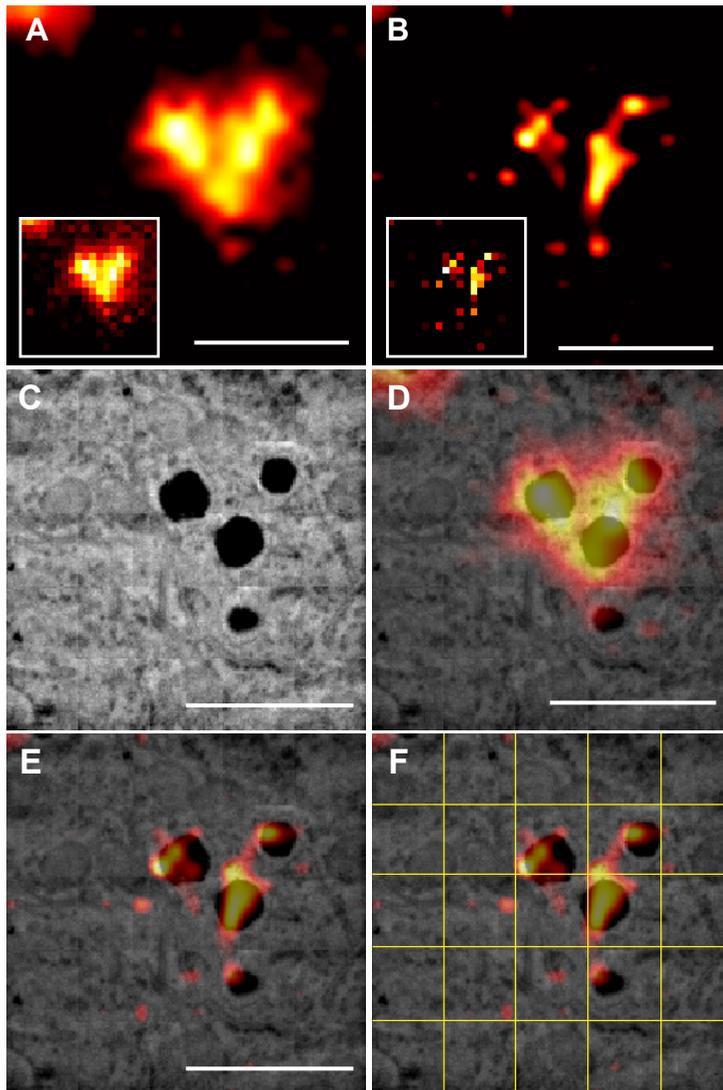
Figure 2.9: **eSRM applied on immunolabeled rat pancreas tissue sections embedded in Epon.** Insulin granules within the Islet of Langerhans are featured, labeled with Alexa594, and DNA counterstained with Hoechst. (A-F) represent the WF, eSRM, RT-SEM, and its' overlay with WF and SR images, respectively. A and B are upsampled tenfold for visualization. Inset images show raw image data. A noise threshold is applied to A, B, and the respective insets for background reduction. (F) shows the SR time-share scanning grid. Scale bars 1µm.

to mitigate this are to scan at the minimum electron dose required for bleaching and use red fluorophores to spectrally bypass the initial (blue) electron-induced resin/biological luminescence.

Observations and Resolution Measure

The previous paragraphs show our implementation and first results for eSRM on several model systems. Besides basic proof-of-principle, these results indicate several foreseen and unforeseen variables that influence eSRM applicability and potentially achievable resolution. Resins and biospecimens were found to exhibit electron-induced luminescence that varies with electron dose (see Chapter 3 for a more detailed analysis). Given these constraints, a palette of bright fluorescent dyes is required to separate them from the background. Red-emitting fluorophores like TRITC and Alexa Fluor 594 are suitable options (see Chapter 4). Another observation in these experiments is that of delocalized bleaching. We noticed that for samples of similar conductivity, smaller fluences cause lower bleaching delocalization (see Chapter 5).

Concerning the resolution, a standard 'out of the box' resolution measure is not directly applicable. eSRM is neither a physical SR technique to which (modified) Rayleigh-Abbe criteria can be used, nor is it entirely a molecular-localization-based technique to which 2D Gaussian/centroid fits or their extensions can be applied. If analyzed analytically, the resolution can be arbitrarily small if the electron bleaching range is sufficiently small and the integration time long enough to lift the signal-to-background ratio. Delocalized bleaching, observed in these experiments, increases the bleaching range. Increasing the integration time, results in photobleaching, and electron-induced luminescence changes the background signal. Analyzing the resolution analytically is, hence, challenging. An estimate of the possible localization accuracy and resolution can be made from the results shown above. In an ideal sample like the polystyrene microspheres, a localization accuracy of ~100nm is demonstrated and validated with the ground truth. However, biological structures remain harder to interpret quantitatively due to contributions from weak signals and non-uniform background fluctuations.

2.5. Conclusion

We have presented a novel SR technique (eSRM) in the context of integrated SR-CLEM, exploiting a focused electron beam to modify fluorescence locally. Further, we have demonstrated proof-of-principle results on fluorescent polystyrene microspheres, microtubules, and immunolabeled rat pancreas tissue sections. Within each sample type, the applicability of the technique to improved fluorescence resolution while overlaid on the EM image is established. The eSRM approach is conceptually similar to SR methods involving photo-bleaching insofar as the quantal loss of fluorescence and its density is concerned. However, eSRM is not molecular-specific by principle. Instead, it reports on the local presence of fluorophores in the background of its ultrastructure. The method applies to any integrated wide-field FM-SEM system where the two modalities are registered to a high degree of accuracy and the position of the electron beam is known in the FM reference frame. Since electron beam-induced bleaching is not dependent on fluorescence wavelengths and generally occurs for all organic molecules, it can be used for any in-resin preserved or post-embedding immuno-targeted fluorescent label. It can be extended to obtain multi-color SR. On ~50nm diameter microspheres, we demonstrate ~100nm localization accuracy.

Fast scanning with the electron beam and high brightness is paramount to reducing photobleaching and having high decays. For this purpose, we use a time-shared approach where the electron beam scans predetermined (multiple) regions simultaneously. Secondly, issues with (some) missing/false localizations may be attributed to low signal-to-background data and scanning artifacts (see also Chapter 5). Regions scanned towards the end of the acquisition tend to have lower signals due to photo-bleaching, but mainly owing to accumulated low electron-dose exposure from surrounding areas. Hence, maximum localization accuracy is obtained in the first scanned areas. We propose minimizing this effect by only scanning the required regions and using the smallest dose for bleaching. Alternatively, scan with the electron beam based on an a priori estimation of fluorophore positions from the WF FM image. Thus the results show promise for electron beam-induced SR to be an added advantage in integrated CLEM setups, particularly for flat samples like tissue sections. However, its applicability requires consideration of sample-based criteria, primarily the precise luminescent response to electron beam-induced damage, investigation of electron-scattering in insulators & the fluorescent capabilities of molecules in a vacuum environment. These questions will form the basis for investigations in Chapters 3 to 5.

BIBLIOGRAPHY

[1] M. H. Ellisman, T. J. Deerinck, K. Y. Kim, *et al.*, "Advances in molecular probe-based labeling tools and their application to multiscale multimodal correlated microscopies", DOI: 10.1007/s12154-015-0132-6.

[2] K. Keevend, R. Krummenacher, E. Kungas, *et al.*, "Correlative cathodoluminescence electron microscopy: Immunolabeling using rare-earth element doped nanoparticles", *Small*, vol. 16, no. 44, p. 2 004 615, 2020.

[3] R. E. Thach and S. S. Thach, "Damage to biological samples caused by the electron beam during electron microscopy", *Biophysical journal*, vol. 11, no. 2, pp. 204–210, 1971.

[4] K. Keevend, L. Puust, K. Kurvits, *et al.*, "Ultrabright and Stable Luminescent Labels for Correlative Cathodoluminescence Electron Microscopy Bioimaging", *Nano Letters*, vol. 19, no. 9, pp. 6013–6018, 2019, ISSN: 15306992. DOI: 10.1021/acs.nanolett.9b01819.

[5] S. Hemelaar, P. De Boer, M. Chipaux, *et al.*, "Nanodiamonds as multi-purpose labels for microscopy", *Scientific reports*, vol. 7, no. 1, p. 720, 2017.

[6] R. Lane, A. H. Wolters, B. N. Giepmans, and J. P. Hoogenboom, "Integrated array tomography for 3d correlative light and electron microscopy", *Frontiers in Molecular Biosciences*, vol. 8, p. 822 232, 2022.

[7] M. T. Haring, N. Liv, A. C. Zonnevylle, *et al.*, "Automated sub-5 nm image registration in integrated correlative fluorescence and electron microscopy using cathodoluminescence pointers", *Scientific Reports*, vol. 7, no. August 2016, p. 43 621, 2017, ISSN: 2045-2322. DOI: 10.1038/srep43621. [Online]. Available: http://www.nature.com/articles/srep43621.

[8] X. Heiligenstein and M. S. Lucas, "One for all, all for one: A close look at in-resin fluorescence protocols for clem", *Frontiers in Cell and Developmental Biology*, vol. 10, p. 1369, 2022.

[9] S. Mohammadian, A. V. Agronskaia, G. A. Blab, *et al.*, "Integrated super resolution fluorescence microscopy and transmission electron microscopy", *Ultramicroscopy*, vol. 215, no. May, p. 113 007, 2020, ISSN: 18792723. DOI: 10.1016/j.ultramic.2020.113007. [Online]. Available: https://doi.org/10.1016/j.ultramic.2020.113007.

[10] W. F. Van Dorp, "Theory: Electron-induced chemistry", in *Frontiers of Nanoscience*, vol. 11, Elsevier, 2016, pp. 115–133.

[11] D. Drouin, A. R. Couture, D. Joly, X. Tastet, V. Aimez, and R. Gauvin, "Casino v2. 42—a fast and easy-to-use modeling tool for scanning electron microscopy and microanalysis users", *Scanning: The Journal of Scanning Microscopies*, vol. 29, no. 3, pp. 92–101, 2007.

[12] O. Y. Ridzel, V. Astašauskas, and W. S. Werner, "Low energy (1–100 ev) electron inelastic mean free path (imfp) values determined from analysis of secondary electron yields (sey) in the incident energy range of 0.1–10 kev", *Journal of Electron Spectroscopy and Related Phenomena*, vol. 241, p. 146 824, 2020.

[13] L. Reimer and S. E. Microscopy, "Physics of image formation and microanalysis", *Springer*, vol. 45, p. 135, 1985.

[14] R. J. Moerland and J. P. Hoogenboom, "Subnanometer-accuracy optical distance ruler based on fluorescence quenching by transparent conductors", *Optica*, vol. 3, no. 2, pp. 112–117, 2016.

[15] R. Chance, A. Miller, A. Prock, and R. Silbey, "Fluorescence and energy transfer near interfaces: The complete and quantitative description of the eu+ 3/mirror systems", *The Journal of Chemical Physics*, vol. 63, no. 4, pp. 1589–1595, 1975.

[16] W. Barnes, "Fluorescence near interfaces: The role of photonic mode density", *journal of modern optics*, vol. 45, no. 4, pp. 661–699, 1998.

[17] S. den Hoedt, A. Effting, and M. Haring, "The secom platform: An integrated clem solution", *Microscopy and Microanalysis*, vol. 20, no. S3, pp. 1006–1007, 2014.

[18] P. de Boer and B. N. Giepmans, "State-of-the-art microscopy to understand islets of langerhans: What to expect next?", *Immunology and cell biology*, vol. 99, no. 5, pp. 509–520, 2021.

[19] P. D. Simonson, E. Rothenberg, and P. R. Selvin, "Single-molecule-based super-resolution images in the presence of multiple fluorophores", *Nano Letters*, vol. 11, no. 11, pp. 5090–5096, 2011, ISSN: 15306992. DOI: 10.1021/nl203560r.

[20] G. Lukinavičius, G. Y. Mitronova, S. Schnorrenberg, *et al.*, "Fluorescent dyes and probes for super-resolution microscopy of microtubules and tracheoles in living cells and tissues", *Chemical science*, vol. 9, no. 13, pp. 3324–3334, 2018.

[21] C. J. Peddie, M. C. Domart, X. Snetkov, *et al.*, "Correlative super-resolution fluorescence and electron microscopy using conventional fluorescent proteins in vacuo", *Journal of Structural Biology*, vol. 199, no. 2, pp. 120–131, 2017, ISSN: 10958657. DOI: 10.1016/j.jsb.2017.05.013. [Online]. Available: http://dx.doi.org/10.1016/j.jsb.2017.05.013.

[22] M. A. Karreman, A. V. Agronskaia, E. G. Van Donselaar, *et al.*, "Optimizing immuno-labeling for correlative fluorescence and electron microscopy on a single specimen", *Journal of Structural Biology*, vol. 180, pp. 382–386, 2012. DOI: 10.1016/j.jsb.2012.09.002.

[23] P. de Boer, J. P. Hoogenboom, and B. N. G. Giepmans, "Correlated light and electron microscopy: ultrastructure lights up!", *Nature Methods*, vol. 12, no. 6, pp. 503–513, 2015, ISSN: 1548-7091. DOI: 10.1038/nmeth.3400. [Online]. Available: http://www.nature.com/doifinder/10.1038/nmeth.3400.

[24] C. J. Peddie, N. Liv, J. P. Hoogenboom, and L. M. Collinson, "Integrated light and scanning electron microscopy of gfp-expressing cells", in *Methods in cell biology*, vol. 124, Elsevier, 2014, pp. 363–389.

[25] A. Srinivasa Raja, P. de Boer, B. N. Giepmans, and J. P. Hoogenboom, "Electron-beam induced luminescence and bleaching in polymer resins and embedded bio-material", *Macromolecular Bioscience*, vol. 21, no. 11, p. 2 100 192, 2021.

2

3

ELECTRON BEAM-INDUCED LUMINESCENCE IN EMBEDDING RESINS

3.1. INTRODUCTION

Electron microscopy (EM) is essential in biology to image the ultrastructural layout of cells and tissues with a typical resolution equal to the sizes of macromolecules [2]. However, electron beam irradiation during EM also leads to structural changes, molecular rearrangements, and degradation[3]–[5]. Cross-linking, chain scission, unsaturation, and gas emission are examples of chemical processes that can subsequently occur. The resultant loss of structural integrity limits the tolerable electron dose and may give rise to dose-dependent distortions, such as local shrinkage. Characterization of these effects on biological specimens and the polymer resins typically used to embed tissues or cellular samples for EM has largely been restricted to observing this shrinkage or the accompanying shape changes and mass loss [6], [7]. Here, we demonstrate that electron beam irradiation of biological media and their embedding resins induces luminescence. The resulting patterns of electron-fluence-dependent intensity rise, spectral redshift, and bleaching are strikingly similar across materials.

Luminescence as a particular outcome of irradiation has been reported across multiple polymers, with plastic scintillators as a potent example [8]–[10]. Recently, electron-irradiation-induced luminescence has been reported for the fabrication of polymethylmethacrylate (PMMA), polystyrene (PS), polyacrylamide, and poly(3-methylthiophene) nanostructures with tunable optical properties [11]–[14]. Interestingly, recent reports on electron-irradiation of fluorescent proteins show electron-enhanced fluorescence and cathodoluminescence (CL) that is robust under electron-irradiation [15], [16]. This could

---

hold great promise for high-resolution multi-modal microscopy. Still, it also raises the question of whether luminescence can be more generally induced during EM in biological samples and their embedding polymer resins.

In this work, we characterized electron-induced luminescence in materials typically used for biological EM. We find that electron-induced luminescence grows in intensity, reaches a peak, and bleaches with increasing electron fluence. This is further accompanied by spectral broadening and redshifting. Moreover, induced luminescence shows intensity variations between compact material and embedded tissue within the same sample. We further discuss how such electron-induced luminescence may affect high-resolution approaches to identify small biomolecular probes via CL, stressing the importance of choosing the correct spectral settings that do not overlap with the induced luminescence spectra.

Later in this thesis, we will tackle how electron-induced luminescence from resins and biomaterial impacts the eSRM technique, with attention to solutions for circumventing the varying background signals that may interfere with true decay detection.

3.2. Results and Discussion

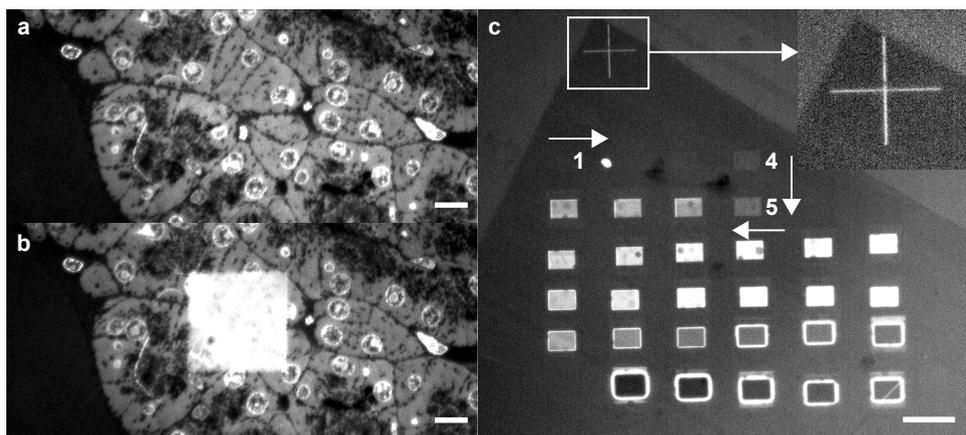### 3.2.1. Luminescence in EM Prepared Materials after Irradiation

Figure 3.1: **Electron fluence-dependent-induced luminescence in EM samples shows dynamic rise and decay.** Hoechst signal of 80nm Epon embedded tissue section (a) before and (b) after electron beam exposure. (c) Electron fluence exposure series on HM20 embedded HeLa cells. Rectangular areas were exposed to increasing electron fluence from the top-left (starting from 1, continuing through 4-5) in a meandering fashion, as indicated by the arrows. The luminescent cross was made with a focused electron beam to aid in region-of-interest retrieval. (a-c) Excitation: 405nm; Emission multi-band filters: 432/515/595/730-25 nm.
Scale bars: (a,b) 10μm; (c) 100μm.

Electron irradiation-induced luminescence is best illustrated upon fluorescent imaging of an area exposed to a focused electron beam as shown in Figure 3.1. Figure 3.1a depicts a typical EM biological sample, an 80nm thin section of Epon-embedded rat pancreas, which was counterstained with Hoechst and imaged on a fluorescence mi-

croscope. Strikingly, the exposed area shows bright luminescence that overwhelms the original signal after EM analysis, as shown in Figure 3.1b.

To address whether this is characteristic of Epon, we subjected three unstained resins, with and without embedded biomaterial, to controlled exposures of increasing electron fluence (Figure 3.1c) in a scanning electron microscope (SEM). The three resins are representative of (typically epoxy or acrylic-based) EM resins, besides Epon, epoxy-based Durcupan, and acrylic-based HM20. In EM, the choice of resin would be dictated by the requirement. Epon has excellent sectioning qualities; HM20 is hydrophilic and suited for immunocytochemistry, while Durcupan is a low-viscosity, water-soluble epoxy variant. All specimens were exposed at 1 and 5 keV landing energies with fluence in the range of 10^{-4} to 10^3 mC cm^{-2}.

We find that upon increasing fluence, luminescence is induced, then rises, and subsequently bleaches. When the exposed area is bleached, the intensity in the surrounding region rises due to proximity exposure, leading to a halo. Note that we advantageously used the same phenomenon of electron-induced luminescence to mark the exposed areas (inset in Figure 3.1c) to navigate in the fluorescence mode towards the areas of interest, especially the regions that showed negligible luminescence (areas 1 to 4).

To understand induced luminescence dynamics, we quantified the emission behavior as it varies with electron fluence. The total luminescence intensity as a function of fluence was obtained for Epon, Durcupan, and HM20, both with and without biological material (Figure 3.2). The applied fluences were controlled by varying the current and the dwell time. Hence, the results are only indicative of the total integrated fluence. UV-Vis spectral characterization was carried out in an independent laser scanning confocal system, where the marker in Figure 3.1c aided in navigation and region of interest retrieval. Standard excitation wavelengths (405, 488, 561, 594, and 633 nm) were applied. Emission was recorded between 414 and 690nm in 9nm intervals and summed together.

We find electron beam-induced luminescence (i) in all examined resins; (ii) irrespective of the biomaterial within resins; (iii) the global trend is a rise and subsequent decay and is similar for all samples; (iv) modulation is contained within 10^{-2} to 10^2 mC cm^{-2} (v) the overall emission intensity per excitation wavelength is highest at 405nm and progressively weakens at higher wavelength emissions. Thus, none of the three examined resins remains inert to electron exposure. The addition of biomaterial does not significantly alter the general trends. The fluence range, spanning four orders of magnitude, indicates that this luminescent phenomenon is a long-drawn effect that cannot be circumvented unless imaging is restricted to low electron fluences ($< 10^{-2}$ mC cm^{-2}). We also note that induced luminescence is an enduring effect. Owing to sample transfer requirements, spectroscopic analysis was typically carried out 1-2 weeks after electron exposure. The resulting data aligns with the patterns observed in preliminary fluorescence inspection as seen in Figure 3.1c.

We next investigate the relation between the induced luminescence and the a priori present auto-fluorescence. Auto-fluorescence contributes to the detected intensities as a starting background level for all samples (Figure 3.2) but is most pronounced for bare Epon. Up to 10^{-2} mC cm^{-2}, auto-fluorescence remains the main contributor to the detected signal, after which electron beam-induced luminescence starts to increase.
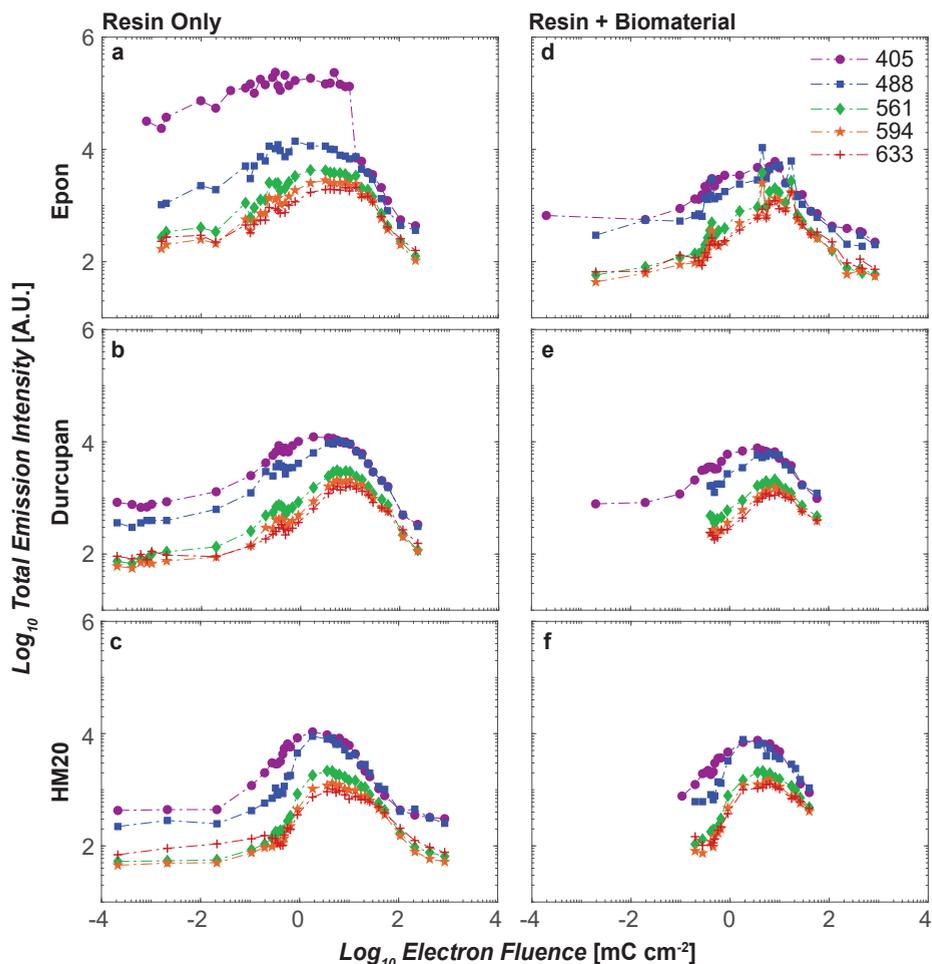
3

Figure 3.2: **Electron-induced luminescence increases, redshifts, and bleaches with increasing electron fluence.** Total electron beam-induced luminescence emission intensity as a function of fluence. Colors indicate excitation wavelengths as indicated. (a-c) bare resins and (d–f) samples with embedded biomaterial, namely rat pancreas tissue (d) or HeLa cells (e,f). All data was recorded with 1 keV electron landing energy. Note that bare Epon already shows high UV-excited auto-fluorescence before electron irradiation. Electron-induced luminescence occurs for all resins, with an intensity increase followed by decay.

Auto-fluorescence emission spectra are broad-banded and most pronounced in the blue regime. However, the cumulative rise in detected signal strictly due to electron beam exposure is most pronounced in the green regime, with a 20-40-fold increase (Figure 3.3).

The variation of electron-induced luminescence with electron fluence is significant for CL, in which a luminescent probe is excited by a focused electron beam. CL signals are typically weak due to a low cross-section and quantum yield compared to, e.g., photon-excited fluorescence. As a result, most reported CL active probes are relatively
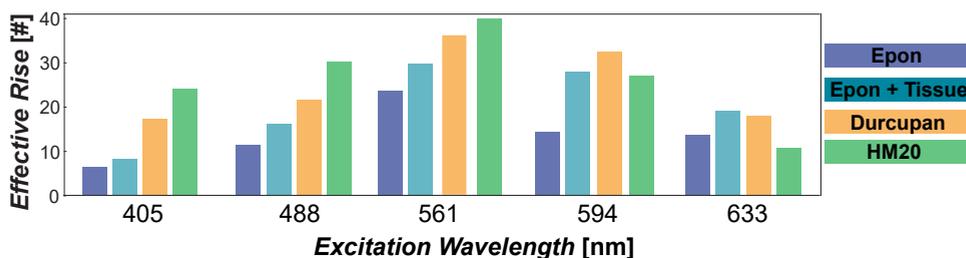
Figure 3.3: **Electron beam-induced fluorescence on top of resin auto-fluorescence.** Effective rise in electron beam-induced luminescence relative to native auto-fluorescence at the respective excitation wavelengths. The rise in electron-induced signal is strongest at 561nm.

large (40-200nm),[17]–[19] but sub-20nm CL nanoparticles have recently been reported. These smaller CL probes better-fit applications in cells and tissues while also allowing higher resolution detection, but the electron-induced luminescence background could obscure the probe signal. While a CL probe may be observable at low electron fluence, i.e., low magnification, higher fluence for higher magnification examination may drown the CL signals in the electron-induced background. Signal-to-background estimates must, therefore, factor in the rise and bleaching of induced luminescence as the cumulative electron fluence changes due to either increased magnification or repeated inspection. Hence, we will analyze the rise, decay, and spectral evolution of electron-induced luminescence in more detail in our samples.

3.2.2. LUMINESCENCE INCREASE, REDSHIFT, AND BLEACHING

The luminescence rise and subsequent bleaching with increasing electron fluence occur in a similar fluence range for all tested resins, exemplified for 561nm excitation (Figure 3.4). A steep rise is observed between $1 \mu C \, cm^{-2}$ and $2 \, mC \, cm^{-2}$. Bleaching commences a few $mC \, cm^{-2}$ later and continues until about $100 \, mC \, cm^{-2}$ when the exposed area has faded completely. Both processes are markedly non-linear: rise and bleach curves are best fit to power-law and double-exponential functions, respectively. Only in specific cases and in a limited fluence interval can the rise be approximated as linear, e.g., for HM20 at excitation wavelengths between 561 and 633nm. While all three resins qualitatively display the same behavior, HM20 shows the largest increase with respect to native auto-fluorescence between 405-561 excitation (Figure 3.3). However, the bare HM20 also has the lowest peak intensity across all excitation wavelengths and the narrowest activation range in terms of electron fluence, making it a suitable choice if a low background bare resin is required (Figure 3.4a, b and Figure 3.9a-l).

Bare resins do not possess compositional variations from the embedded biological specimens. Yet, real EM samples contain biomaterial, occasionally with empty resin areas within. Therefore, we examined bare resin and bio-embedded regions separately to account for their individual luminescence contributions (Figure 3.4c, d and Figure 3.9A-J). Replacing resin with fixed biomaterial (low auto-fluorescence) reduces induced luminescence. In addition, fixation and staining chemicals (aldehydes, osmium tetroxide,
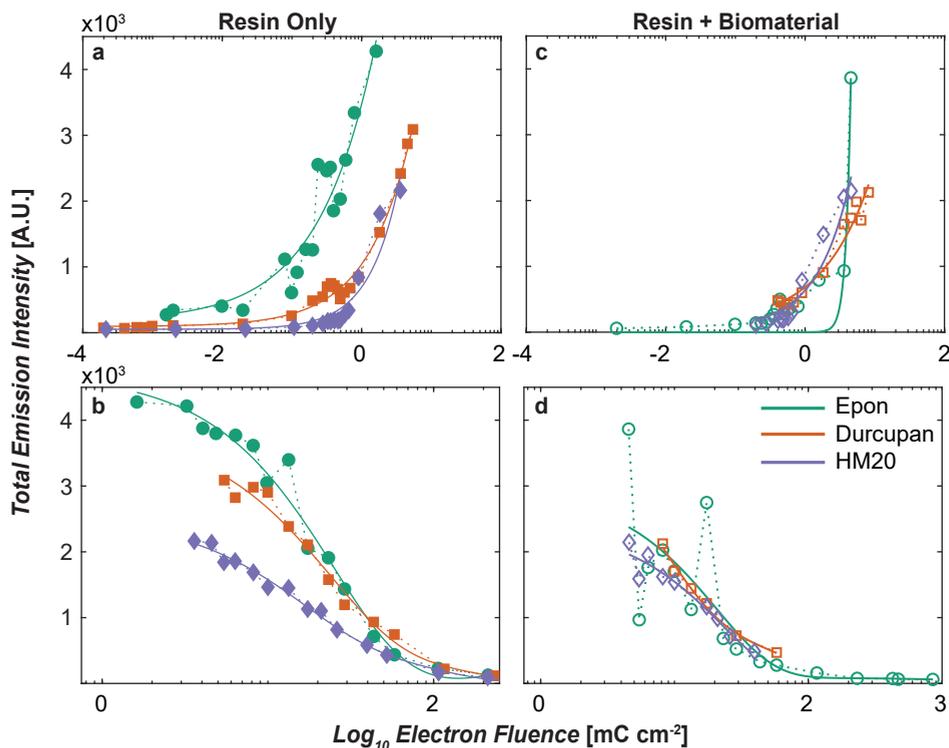
Figure 3.4: **Luminescence rise and bleaching curves fall in similar fluence magnitude regimes across samples.** (a) The rise in electron-induced luminescence for all bare resins is shown (excitation: 561nm) as a function of electron fluence. (b) The decay in luminescence in the bleaching regime. (c-d) Similar curves for the resins with embedded biomaterials. Symbols indicate measured values; solid lines indicate fit with a power-law and double-exponential function for the rise and bleaching regime, respectively. In all cases, the induced luminescence rises between 10^{-3} and 5 mC cm^{-2}, and decays between 5 and 100 mC cm^{-2}. Full curves for all excitation wavelengths and materials can be found in the supporting information later in this chapter.

and potassium ferrocyanide) could down-regulate the high intensities observed with pure resin. Similar behavior is observed for the auto-fluorescence of Epon (Figure 3.2a, d). Thus, while biological specimens are auto-fluorescent, their luminescence contribution is lower than resin, possibly less UV excitable, and/or with a lower quantum yield. Note that the Epon-embedded pancreas shows larger fluctuations in measured intensity per fluence. We attribute this to density differences between the exocrine and the materially denser endocrine regions and the fact that before exposure, we have no means to discriminate the two. All data is from the cytoplasm for Durcupan and HM20 embedded with HeLa cells. Importantly, we see that the observed changes in induced luminescence intensity will depend more on density variations in the embedded sample than in the chosen resin.

Spectral characterization of induced luminescence is critical to identify emission windows that permit background filtering. Comparison of induced luminescence per

excitation wavelength (Figure 3.3) suggests that the spectrum redshifts with increasing fluence. Orange and red wavelengths still experience increased induced luminescence, while UV and blue excitations have already decayed. This is confirmed by a full spectral analysis (Figure 3.5).

The emission spectrum broadens and redshifts upon increasing electron irradiation for all three resins. For 405nm excitation, where the full 414-690nm range is analyzed for emission, we observe three patterns: (i) At low fluence, induced emission begins at low intensities between 420-575nm. There is no clear spectral peak, but the spectral center of mass is at 503-512nm. (ii) Upon increasing electron fluence, the emission increases, and the spectrum develops a peak in the above range. The spectral width has now broadened into the red part of the spectrum, covering the entire measured range. (iii) When the overall intensity bleaches, the spectral peak skews to orange-red wavelengths while the width progressively narrows until it settles below background levels. Bare Epon deviates from the rest in its high UV excited auto-fluorescence. This shows a sharp drop at ~10 mC cm^{-2} to the intensity values observed at 488nm excitation, suggesting damage to the UV excitable component. The higher excitations show a threshold at ~1 mC cm^{-2} below which effective excitation only occurs in the UV. 488nm shows diminished emission around this fluence, and this is further lowered between 561 - 633nm. The same behavior is observed for resins with embedded biological material (Figure 3.10). Only in the case of bare Epon is the reduction in intensity at higher wavelengths less pronounced. In addition to redshifting, a subtle increase in red wavelength emission is observed with increasing excitation. The fact that the spectrum ultimately extends over the full range is further confirmed by analyzing the spectral range where the emission exceeds a set threshold level. (Figure 3.5b).

3.2.3. ELECTRON ENERGY DEPENDENCE

In addition to electron fluence, we examined the influence of electron beam primary energy on induced luminescence. At 1 keV landing energy, the interaction volume is contained within our specimen's ~80nm thickness. Thus, the total number of scattering events is encapsulated in the specimen, providing a direct relationship between the fluence and the ensuing luminescence. With 5 keV landing energy, we retrieve the same behavior for induced luminescence, albeit shifted to larger fluence (Figure 3.11). At 5 keV, a significant portion of the interaction volume falls into the sample support. Thus, a large fraction of the primary electrons exit the section without scattering, and consequently, the threshold fluence for luminescence induction is higher. In addition, we note that at 1 keV, the distribution of secondary electrons and that generated by backscattered electrons, namely SE2s, is similar, thereby tightly localizing the damage to the scanned regions. At 5 keV or higher energy, the backscattered electrons and SE2s will have a broader distribution area. With higher fluence, the cumulative rise in fluence in these delocalized areas will incite luminescence. The effect is thus a central bleached region, similar to that of 1 keV but with a luminescent perimeter (See Figure 3.2). The fact that induced luminescence is a by-product of the density of low energy scattering events is reflected at the fluence at which maximum intensity is reached (Figure 3.11). Epon, Durcupan, and HM20 reach peak intensity at ~0.30, 1.8, and 1.8 mC cm^{-2} at 1 keV irradiation and 405nm
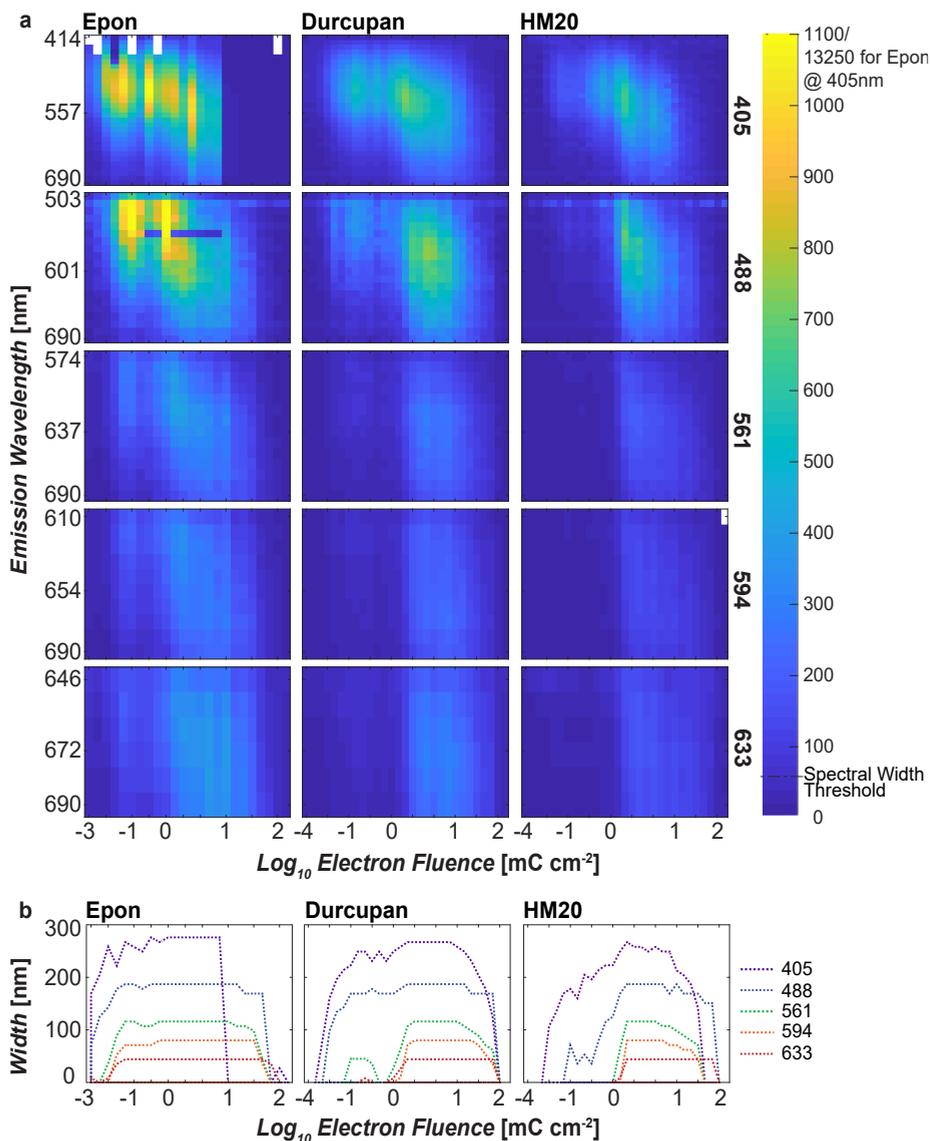
Figure 3.5: **Electron-induced luminescence spectrum shifts from blue to red upon increasing electron fluence.** (a) Color-coded luminescence emission intensity as a function of electron fluence for each of the different excitation wavelengths indicated on the right. White pixels denote missing values. (b) Spectral width as a function of electron fluence for each excitation wavelength and resin. The spectral width has been defined as the range in which the threshold intensity indicated in the color scale in (a) is exceeded. The threshold (725 for bare Epon and 60 units for the rest) is set slightly above the highest auto-fluorescence values. The induced luminescence spectrum broadens and redshifts upon increasing exposure until it spans the entire visible range and then narrows again upon bleaching.

excitation, respectively. This is shifted to ~1.6, 3.6 and 6.0 mC cm^{-2} at 5 keV irradiation. Similar patterns in radiation damage as a function of specimen thickness relative to the landing energy have been shown [20]. Since low-energy secondary electrons predominantly cause electron-induced damage, we point out that 1 keV irradiation of a material with a higher secondary electron coefficient is expected to luminesce at lower fluence.

3.2.4. Electron-Induced Luminescence in Biological Materials

The electron-induced luminescence is not restricted to resins but also shows variations within biological materials. We noted differences between exocrine and endocrine regions in Epon-embedded rat pancreas tissue, which we attributed to changes in biomaterial density. This is exemplified by an electron beam scan area crossing the boundary between bare and tissue embedding Epon resin (Figure 3.6). For the same fluence, bare resin shows higher induced luminescence than the tissue regions. However, nuclei appear brighter in tissue than in the cytoplasm (Figure 3.6b). Note that the entire nuclei stand out in induced luminescence and not merely the Hoechst expressing regions visible in Figure 3.6a. Figure 3.6c, d report total induced luminescence differences between the cytoplasm and nucleus from unstained Epon sections, which indicate that a slightly higher luminescence is reached in the nucleus at similar fluence. This corroborates the notion that reactions in and between organic macromolecules and polymers are responsible for the induced luminescence. Thus, regions dense in biological macromolecules, like the nucleus [21], will stand out in electron-induced luminescence.

Remarkably, electron beam-induced luminescence is also observed in resin-free HeLa cells (Figure 3.7). Even without any resin, electron-induced luminescence persists, rises, and bleaches at high fluence (Figure 3.7a from left to right). The scanned regions also follow similar spectral tendencies, indicated for both 470nm and 555nm for low (Figure 3.7b) and high fluence (Figure 3.7c), respectively. Low fluence shows minimal induction of luminescence at 470nm and no discernible induced luminescence at 555nm (Figure 3.7b), in correspondence with our observations on the resins (Figure 3.5). Higher electron fluence induces stronger luminescence, which can also be excited with 555nm (Figure 3.7c). This confirms that native organic biological materials, in this case possibly in combination with the aldehyde fixatives, show the same trends in electron-induced luminescence as the polymer resins.

Though electron-induced luminescence appears to reveal previously unseen cellular contrast, we attribute the resultant contrast to varying effective doses in regions with material differences. Figure 3.7a shows non-uniform luminescence towards the bottom right of the exposed area. Thickness differences in fixed, dried cells can range from tens of microns close to the nucleus to a few nanometers toward the cell edges. Electron beam irradiation with fixed landing energy, and thus interaction depth, leads to a luminescence profile that is enhanced in the thicker parts. The nucleus, where thickness and macromolecular density increase, shows the strongest electron-induced luminescence signal. The highest fluence exposure illustrates electron scattering proximity exposure (rightmost panel in Figure 3.7a): the exposed area is bleached but flanked by a thin luminescent periphery, again highlighting that fixed cells show the same qualitative behavior as the bare and embedding resins.
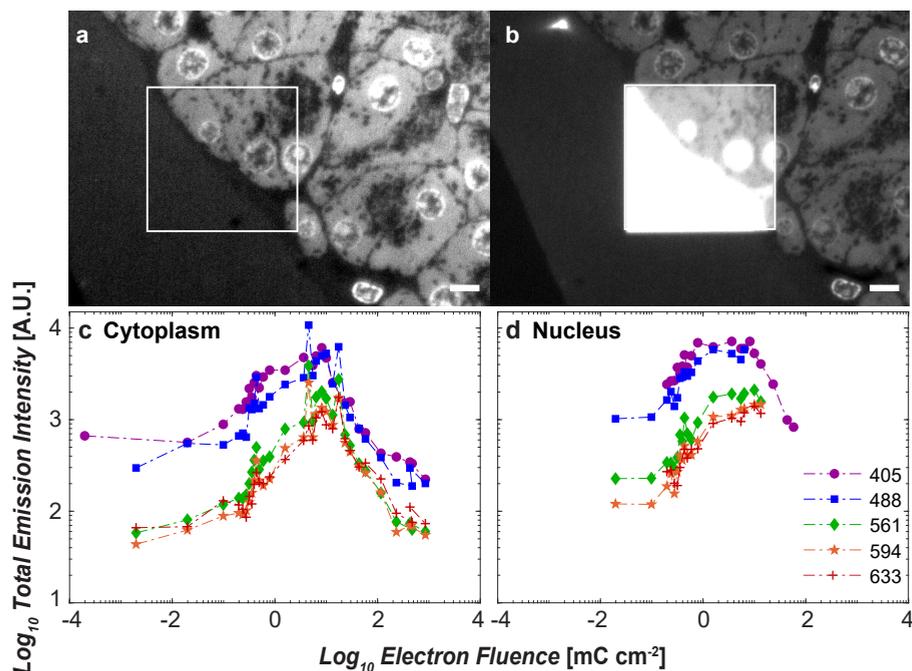
3

Figure 3.6: **Induced luminescence within the biomaterial correlates with macromolecular density.** (a) 80nm Epon embedded Hoechst-stained (DNA, RNA) rat pancreas tissue section, including the boundary between bare resin and tissue. The image was recorded with 405nm excitation before electron irradiation. (b) The same image was recorded after electron beam exposure of the boxed area. The scanned area straddles the boundary between the bare resin and rat pancreas tissue. Contrast and brightness adjusted in (b) to highlight induced luminescence variances. The induced luminescence intensity is seen to vary within the biological material despite the same applied fluence. Regions that are denser in macromolecular composition (bare resin, nucleus) appear brighter. (c, d) Total luminescence intensity as a function of fluence for (c) cytoplasmic regions and (d) nuclear regions for all excitation wavelengths. The nuclear regions show higher induced luminescence intensity at the same fluence as the cytoplasm. Scale bar in (a, b) is 10µm.

3.2.5. POLYSTYRENE AND POLYMETHYLMETHACRYLATE

Electron beam-induced luminescence has been reported for nanopatterning fluorescent structures in pure polymethylmethacrylate (PMMA)[11] and polystyrene (PS).[12] While PS undergoes spectral redshifting and broadening with increasing fluence, similar to this study, PMMA depicts blue emission, which linearly increases in intensity and with no spectral shift or broadening. We compare the PMMA findings with our HM20 results (Figure 3.8), as the latter being a methacrylate resin, still shows spectral redshifting and broadening, which were absent in PMMA.

1 keV data on HM20 cover a similar fluence range as the 50 keV results on PMMA. Between 7 and 25 mC cm^{-2}, HM20 shows decreasing emission, spectral redshifting, and width narrowing, while PMMA reports linearly increasing blue emission without spectral change. However, the 50 keV PMMA irradiation was conducted with 1 nA on a 500
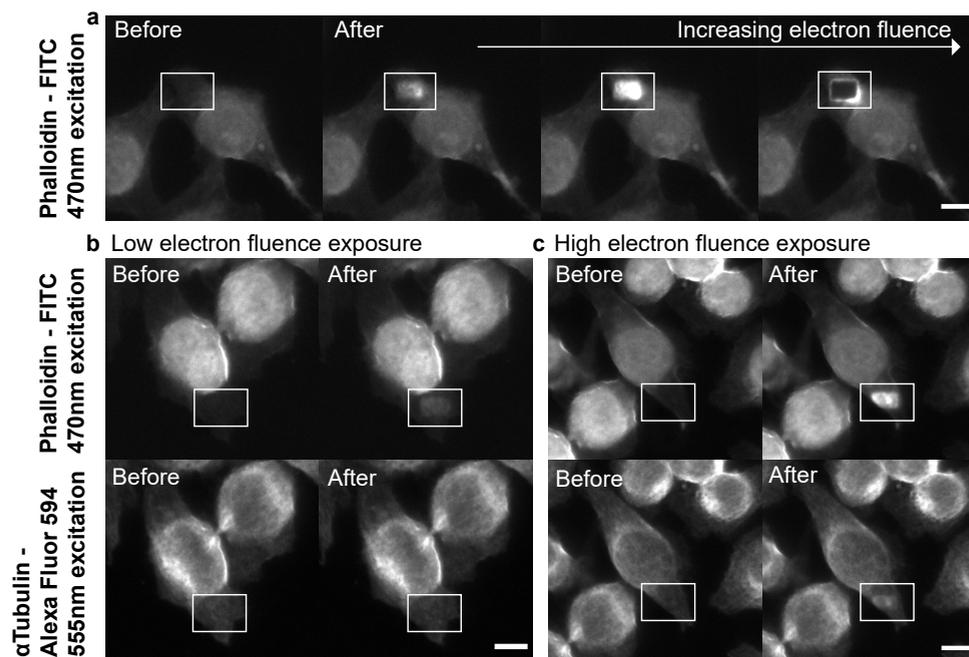
Figure 3.7: **Electron beam-induced luminescence persists in fixed HeLa cells without embedding resin.** Fixed HeLa cells labeled for Phalloidin with FITC and α-tubulin with Alexa Fluor 594 were selectively exposed to electron beam irradiation. The solid rectangle surrounds the scanned region. (a) Excitation of Phalloidin-FITC at 470nm. Electron fluence increases from left to right, starting from zero exposure. Luminescence is induced in the cellular sample upon electron exposure, followed by bleaching at higher electron fluence. (b) and (c) depict excitation at 470 and 555nm for low and high electron fluence, respectively. The left and right images show before and after electron beam irradiation. (b) confirms that induced luminescence grows from the blue spectral range, as observed in bare resins. For the same low electron fluence, 470nm illumination begets higher induced luminescence, while it is negligible at 555nm. (c) further confirms that luminescence redshifts upon higher electron fluence exposure. Scale bars 10μm.

nm layer, meaning that a substantial portion of the electron fluence is deposited in the polymer. As the differential cross section of elastic scattering is inversely proportional to the square of the kinetic energy [22], the scattering cross section at 50 keV is ∼100 times lower than at 5 keV. Without normalizing for thickness differences, a 100x lower fluence is thus a ballpark estimate. Indeed, comparing the PMMA results to our 5 keV irradiation of HM20 with a fluence of 0.002 to 1 mC cm^{-2}, we also observe increasing luminescence intensity and a nearly non-shifting spectrum. Thus, HM20 and the pure PMMA may display the same behavior, only our full data extends over a wider fluence range, from 10^{-4} to 250 mC/cm^2, in which the non-linearity, spectral shifts, and bleaching are observed.

We have reported electron-induced luminescence across various materials relevant to biological EM. We have also encountered, but not quantified, electron-induced luminescence effects in materials that do not have biological applications, namely styrene dyes and thermoplastic wires (data not shown).

Focused electron beam irradiation on PS from different sources [12], [23] indicates
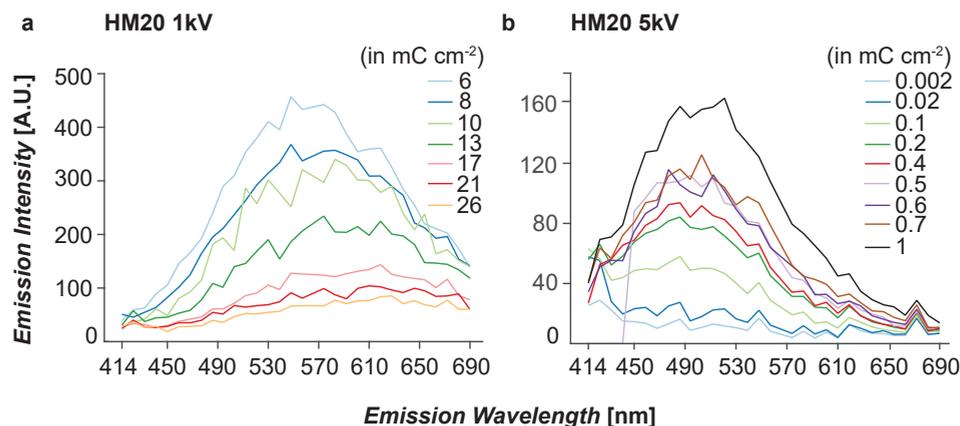
3

Figure 3.8: **Comparison of electron-induced luminescence in methacrylic HM20 with literature results on PMMA [11].** Induced luminescence as a function of emission wavelength for (a) 80nm thick HM20 after irradiation with 1 keV electrons, (b) with 5 keV electrons, both at 405nm excitation. Data in (a) and PMMA [11] cover a similar range in applied electron fluence, but HM20 shows decreasing, redshifting luminescence while PMMA shows increasing, non-shifting induced luminescence. For HM20, the interaction volume is entirely deposited in the sample, while for PMMA, most scattering occurs in the underlying substrate. For HM20 at 5 keV exposure, fluences give a rough approximation of a similar dose deposited in the sample compared to PMMA. HM20 shows a luminescence increase in this range that could also be approximated as spectrally non-shifting. Legends denote respective fluences in mC cm^{-2}.

an increase in intensity with fluence, followed by decay, marked by clear spectral redshifting. Multiple polymers, including Epoxy, PMMA, and PS, have shown optical discoloration with a fluence-dependent redshift upon gamma irradiation [24]. We note that our materials are not pure polymers and were treated according to EM sample preparation protocols. HM20 was embedded with HeLa cells after fixation with aldehydes and osmium tetroxide. The generated low-energy electrons could initiate multiple chemical reactions even with a pure polymer, with other chemicals adding complexity. The question on the chemical origins of induced luminescence is outside the scope of our study. Still, our data in the context of literature raises two questions: (i) When examined over an extensive fluence range and similar conditions, will multiple polymers show similar induced luminescence behavior despite their chemical dissimilarities and consequent differences in luminescence origin? (ii) If multiple chemical sources of induced luminescence are possible, should attention be diverted to subtle signatures rather than their mere presence, given how commonplace it is?

3.2.6. Considerations

Electron-induced luminescence can impact CL measurements, where the aim is to detect luminescence from biological markers excited by a focused electron beam. The reported exposure-dependent induced luminescence could make for a varying background that deteriorates signal detection efficiency. We note that our analysis uses photon-excited fluorescence imaging after fixed fluence electron exposure. In general, photo-

and CL spectra tend to overlap, but the efficiency for excitation with an electron beam may be considerably lower than the photon-excitation efficiency. On the other hand, the same holds for the excitation efficiencies of CL probes, and the push for smaller probes [25], [26] will also considerably reduce the detectable probe signal. The broad examined fluence range applies to both high-resolution EM and CL probe excitation, and the predictable trends across different media permit optimized probe and experimental parameter selection. However, precise determination for CL requires a thorough body of work assessing optimized CL energies. As low electron fluences do not trigger induced luminescence between 561 and 633nm, low fluence examination and red-excitable probes are preferred. Thin resin sections also automatically keep the background low.

Our results provide perspective in light of recent results on electron exposure-induced CL from existing fluorescent probes such as fluorescent proteins [16]. Further analysis of electron-induced luminescence origins may be required to confirm whether these CL changes occur at the single probe level or result from chemical reactions between probes and/or the environment. For CLEM, the impact of electron-induced luminescence is more subtle since FM inspection typically precedes EM imaging. However, integrated systems that employ novel methods to manipulate fluorescence with an electron beam may have to factor in and/or circumvent the effects of induced luminescence. Some examples include using the electron beam to selectively/permanently switch off fluorescence for localization or generate sparsity for super-resolution approaches [27].

Moreover, the prevalence of electron-induced luminescence in all examined resins, embedded biomaterial, and resin-devoid fixed cells could allow electron-exposed biological samples to be annotated using precisely defined (size, intensity, and emission wavelength) luminescence markers (Figure 3.1c). This could facilitate easy optical inspection of non-fluorescent EM samples to identify and/or retrieve EM irradiated, and thus previously examined regions, which could be particularly useful in large-scale intermittent EM imaging. Preliminary experiments reveal that even nylon microfibers from a 3D printer display visible luminescence after electron exposure (data not shown). This may provide an interesting way to visualize microplastics in a fluorescence microscope. As discussed above, further investigation into the involved chemical transitions and higher-resolution spectral analysis would be relevant.

3.3. CONCLUSION

We have spectrally (UV-Vis) characterized luminescence induced by electron beam irradiation in two epoxy resins (Epon, Durcupan) and one methacrylate resin (HM20) over a broad electron fluence range, from 10^{-4} to 10^3 mC/cm^2, both with and without embedded biological samples. We report that electron-induced luminescence is pervasive in all three bare resins and biomaterial within the resin and occurs even in fixed, whole cells in the total absence of resin. Further, we observe similar trends across all samples, with the luminescence first increasing, then redshifting, and finally bleaching upon increasing fluence. Increased landing energies cause reduced scattering in the specimen, shifting the luminescence profiles to higher fluences. The fact that electron irradiation initiates luminescence centers in resins and biological materials is important for select-

ing probes and conditions for CL and CLEM. However, electron-induced luminescence also provides a means to track or mark regions of interest inspected with EM or to annotate sections for later reference. More generally, the possibility of turning many polymers into luminescent (nano) structures with tunable intensity and spectral properties is attractive and applicable to multiple fields of biology, materials science, and nanophotonics.

3.4. Experimental Methods

80nm thick epoxy (Epon, Durcupan) and methacrylate-based resin (HM20) sections were subjected to controlled electron fluence exposure and subsequent UV-Vis spectral characterization. Epon was examined in a bare format and, after that, again with embedded rat pancreas tissue—the rest of the samples contained embedded biomaterial. Without any labeling, the biological regions could be distinguished from the surrounding bare resin areas through differences in their electron-induced luminescence intensities. However, epoxy resins tend to copolymerize with proteins [28], and the demarcated regions may not represent purely bare resin behavior. The resin type and the associated biomaterial are Epon with rat pancreas tissue and Durcupan/HM20 with HeLa cells.

3.4.1. Preparation of Resin Sections

For Epon (Serva electrophoresis GmbH, Germany) and Durcupan (ACM, Sigma-Aldrich), the biomaterial was first fixed with 2% paraformaldehyde and 0.2% glutaraldehyde in 0.1 M sodium cacodylate buffer, followed by post-fixation with 1% osmium tetroxide and 1.5 % potassium ferrocyanide in 0.1 M sodium cacodylate buffer. Subsequently, for the epoxy resins, tissue and cells were dehydrated through a graded series of ethanol and embedded in the epoxy resin, which was polymerized for 24 hours at 58°C. Bare Epon blocks were created by polymerizing blocks of pure resin for 24 hours at 58°C. For HM20 embedding (Electron Microscopy Sciences, Hatfield, PA), cells were dehydrated through a graded ethanol series with lowering temperature down to -30°C and finally polymerized in pure HM20 by UV irradiation for 16 hours at -30°C. Ultrathin 80nm sections were cut from each sample using an ultra-microtome (Leica EM UC7) and placed on ITO-coated glass coverslips (Materion Balzers Optics). We note that for Epon, bare and tissue-embedded results were recorded from separate samples, whereas bare and bio-embedded regions in Durcupan and HM20 were distinguished within the same specimen. HeLa cells were fixed with a combination of 2.5% paraformaldehyde and 1.25% glutaraldehyde, labeled with Phalloidin-FITC (Invitrogen, F432), and immunolabeled against αTubulin (Sigma, T6074) with Alexa Fluor 594 (Invitrogen, A21207), and dehydrated through a graded ethanol series.

3.4.2. Electron Irradiation

Focused electron beam irradiation was performed in a Thermo Scientific Verios SEM retrofitted with a Delmic SECOM [29] for in-situ fluorescence microscopy. Exposures were conducted at a chamber pressure of ~ 5.10^{-4} Pa. The resin sections are markedly

visible in the SEM-SECOM under UV illumination at 405nm (Figure 3.1). Subsequent navigation was hence possible without unnecessary electron beam exposure. However, polymers and chiefly epoxy derivatives are susceptible to UV photo-degradation [30]; hence, the illumination power and duration were kept to a minimum. Before irradiation, the beam currents were measured using a Faraday cup (Thermo Scientific system standard test sample) via a pico ammeter. The applied fluence is calculated as follows: Fluence = [Measured current * Dwell time * Scan resolution] / Irradiated area, where the dwell time refers to the electron beam dwell time per exposed pixel. Samples were exposed at 1 and 5 keV landing energies with a total fluence of 10^{-4} to 10^3 mC cm^{-2}. This large range was chosen to sweep the entire spectrum, including luminescence induction, rise, and subsequent bleaching. Each fluence was applied on a rectangular area of 50 μm by 30 μm in a meandering fashion, increasing fluence from the top-left to the bottom-right. In poorly conducting specimens like these, beam deflection due to charge accumulation is possible.[31] However, this does not influence the central irradiated region, where the integrated fluence is unaffected. The fluence lost to the edges is marginal compared to that deposited in the ROI (area: 1500 μm^2) and is thus ignored.

3.4.3. UV-VIS SPECTRAL CHARACTERIZATION

The UV-Vis emission of electron beam irradiated resins was spectrally characterized at five excitation wavelengths (405,488,561,594,and 633nm) using a laser scanning confocal system (Zeiss LSM 780, Plan-Apochromat 63x/1.40 lens). Emission spectra were recorded with lambda mode, creating intensity profiles between 414 and 690nm at 9nm intervals for each excitation with appropriate beam splitters. The illumination power per excitation was set at 6.5, 5.5, 16, 15, and 13 μW from 405 to 633nm, respectively. The results were scaled to the power at 405nm to make the emission intensities comparable. The detector's analog/digital gain and offset were constant, with the pinhole held completely open. The same settings were applied to every examined resin.

3.5. SUPPORTING INFORMATION

5 KEV LANDING ENERGY IRRADIATION

Similar to Figure 3.2, Figure 3.11 depicts the total emission intensity as a function of electron fluence but now for electron exposure at 5 keV landing energy. The left and right columns depict respective bare and bio-embedded resins. As mentioned earlier, the choice of two (1 and 5 keV) landing energies is substantiated by the following reasons: a) Low energies (1 – 3 keV) are preferred for imaging biological/soft material samples. b) The effective interaction volume at 1 keV is completely contained in the thickness of the specimen, thereby encapsulating the total number of possible scattering events, which in turn provides a clearer relationship between the applied fluence and the ensuing luminescence.

Since low-energy secondary electrons predominantly cause electron damage, 1 keV with a higher secondary electron coefficient is hypothesized to begin luminescing at lower fluences. Further, it is also the regime where the distribution of SE2s is similar
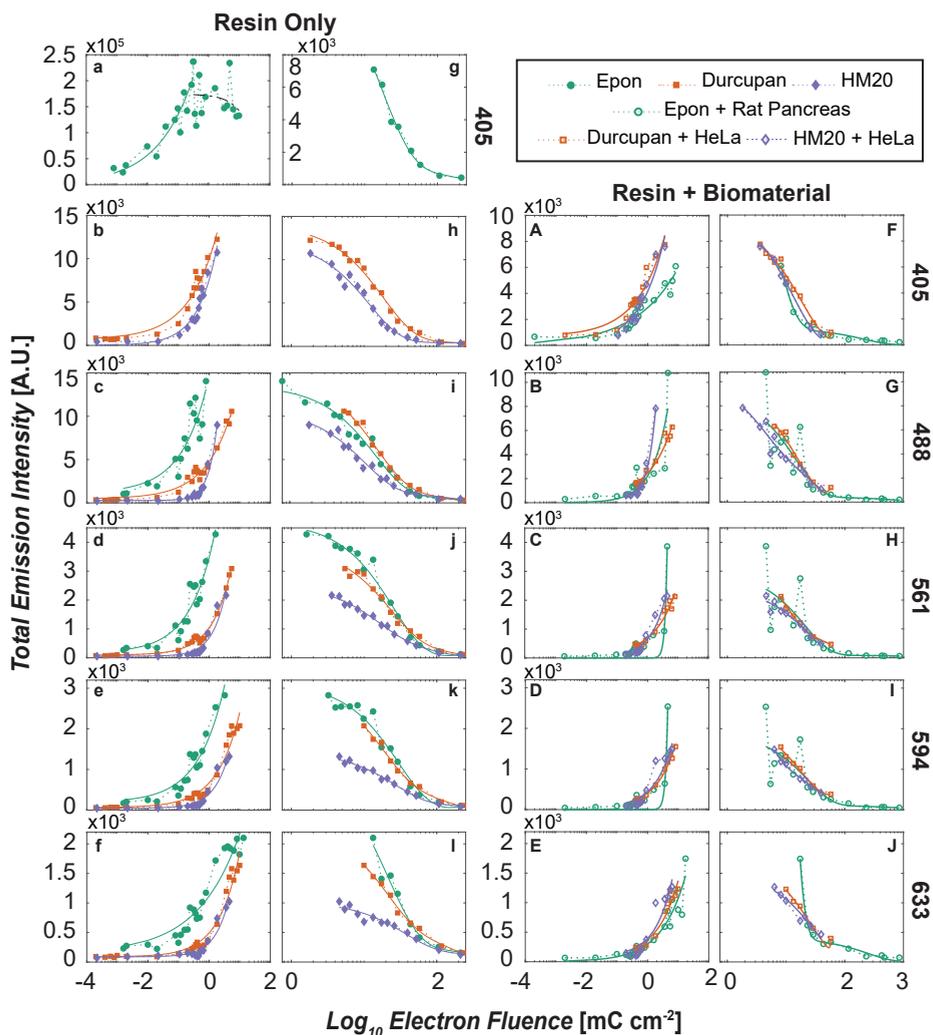
3

Figure 3.9: **Total emission intensity as a function of electron fluence for bare (a-l) and bio-embedded (A-J) resins and corresponding fit curves.** The associated excitation wavelength is denoted on the right of each row panel. (a-f) and (A-E) separate the rising intensity regime from the decay in (g-l) and (F-J). Dotted lines and solid lines represent experimental data and fit curves, respectively. Filled and open markers are used to distinguish bare and bio-embedded data. The black dashed line for bare Epon at 405nm denotes data outliers to the applied fit equations. Displayed in semi-logarithmic scale. Rising curves are fit to a power law; decay curves are fit to a double exponential. HM20 has the slowest rise curves in the bare resins. Embedding biomaterial reduces intensity differences.

to that of the secondary electrons, thereby more tightly localizing the damage to the scanned regions. On the contrary, a higher landing energy would imply the following: a) A significant portion of the primary electrons would exit the section without scattering in the material. Consequently, the threshold fluence for luminescence induction
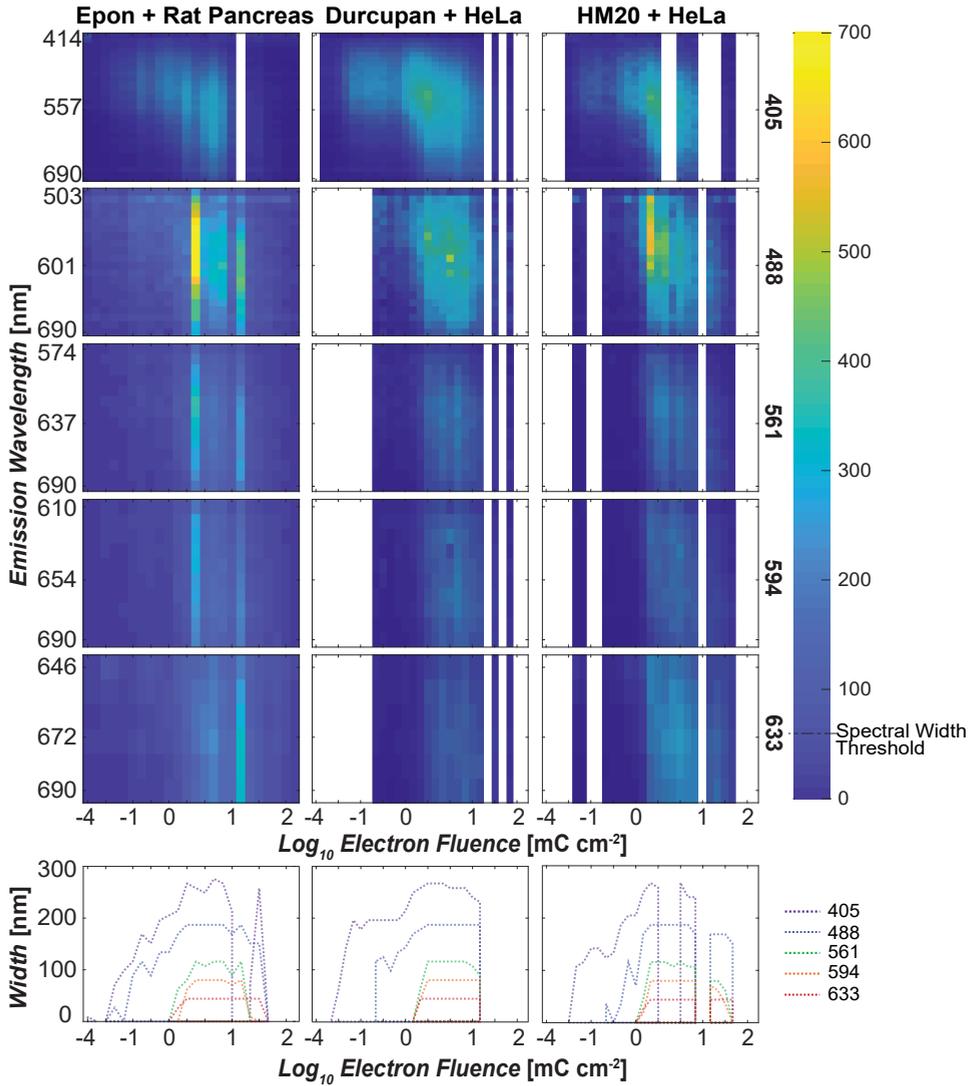
Figure 3.10: **Electron-induced luminescence spectrum shows a redshifting pattern with increasing electron fluence, also for bio-embedded resins.** (a) Luminescence emission intensity as a function of electron fluence for each of the different excitation wavelengths for Epon + rat pancreas, Durcupan + HeLa cells, and HM20 + HeLa cells. The excitation wavelengths are indicated on the right vertical axis as 405nm, 488nm, 561nm, 594nm, and 633nm, respectively. The color scale denotes intensity according to the indicated scale. Missing pixels are indicated in white. (b) Spectral width as a function of electron fluence for the respective resins in each column at varied excitation wavelengths. The intensity threshold for calculating spectral width is indicated on the color bar. Spectral behavior is similar to the results for bare resins in Figure 3.5.

would be higher. b) The backscattered electrons and SE2s will have a broader distribu-

tion area. With higher fluence, the cumulative rise in fluence in these delocalized areas will incite luminescence. The effect is thus a central bleached region, similar to that of 1 keV but with a much more diffuse and intense luminescent perimeter (See Figure 3.2). While we did not explicitly monitor the periphery, if the luminescence is a by-product of the density of low energy scattering events, it should reflect a higher fluence at which the maximum intensity is reached. Figure 3.11 indicates that this is indeed the case. A similar reasoning holds for higher energies, as seen in transmission electron microscopy (TEM), where there is minimal dose deposition within the specimen. This would consequently increase the threshold fluence for luminescence induction, especially since TEM dose rates are also considerably lower. Convergent beams in scanning transmission electron microscopy (STEM) would have comparable dose rates. The scattering cross-section would determine how the induced luminescence spectrum is offset with regard to fluence. Contrary to expectations, it is not immediately understood why bare Epon at 5 keV does not show higher UV intensities or a steep drop, as observed in Figure 3.2. The rest of the excitations follow responses as would be predicted from Figure 3.2.
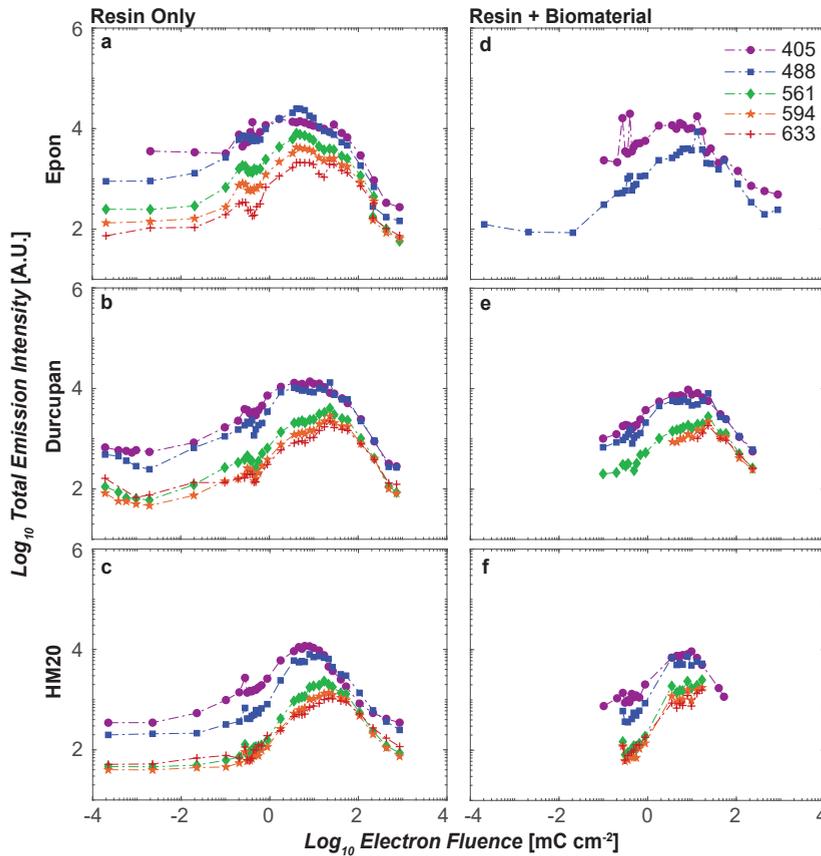
Figure 3.11: **Total electron-induced luminescence emission intensity as a function of fluence for each excitation wavelength (shown in color with varied markers) for 5 keV electron landing energy.** (a) – (c) and (d) – (f) represent the bare and bio variants respectively. Graphs are displayed in logarithmic scale. The higher landing energy compared to the data in Figure 3.2 (1 keV) results in lowered scattering in the material. The luminescence profiles hence shift to higher fluences.

BIBLIOGRAPHY

[1] A. Srinivasa Raja, P. de Boer, B. N. Giepmans, and J. P. Hoogenboom, "Electron-Beam Induced Luminescence and Bleaching in Polymer Resins and Embedded Biomaterial", *Macromolecular Bioscience*, vol. 2100192, pp. 1–10, 2021, ISSN: 16165195. DOI: 10.1002/mabi.202100192.

[2] A. J. Koster and J. Klumperman, "Electron microscopy in cell biology: Integrating structure and function", *Nature Reviews Molecular Cell Biology*, vol. 4, no. SUPPL. Pp. 6–10, 2003, ISSN: 14710072. DOI: 10.1038/nrm1194.

[3] A. Chapiro, "Chemical Modifications in Irradiated Polymers", *Nuclear Inst. and Methods in Physics Research, B*, vol. 32, pp. 111–114, 1988.

[4] J. H. O'Donnell, "Chemistry of Radiation Degradation of Polymers", pp. 402–413, 1991. DOI: 10.1021/bk-1991-0475.ch024.

[5] K. Dawes, L. C. Glover, and D. A. Vroom, "The Effects of Electron Beam and g-Irradiation on Polymeric Materials", *Physical Properties of Polymers Handbook*, pp. 867–887, 2007. DOI: 10.1007/978-0-387-69002-5{_}52.

[6] C. Kizilyaprak, G. Longo, J. Daraspe, and B. M. Humbel, "Investigation of resins suitable for the preparation of biological sample for 3-D electron microscopy", *Journal of Structural Biology*, vol. 189, no. 2, pp. 135–146, 2015, ISSN: 10958657. DOI: 10.1016/j.jsb.2014.10.009. [Online]. Available: http://dx.doi.org/10.1016/j.jsb.2014.10.009.

[7] R. Skoupy, J. Nebesarova, M. Slouf, and V. Krzyzanek, "Quantitative STEM imaging of electron beam induced mass loss of epoxy resin sections", *Ultramicroscopy*, vol. 202, no. December 2018, pp. 44–50, 2019, ISSN: 18792723. DOI: 10.1016/j.ultramic.2019.03.018.

[8] E. Kim, J. Kyhm, J. H. Kim, *et al.*, "White light emission from polystyrene under pulsed ultra violet laser irradiation", *Scientific Reports*, vol. 3, pp. 3–6, 2013, ISSN: 20452322. DOI: 10.1038/srep03253.

[9] A. Quaranta, "Recent developments of ion beam induced luminescence: Radiation hardness study of thin film plastic scintillators", *Nuclear Instruments and Methods in Physics Research, Section B: Beam Interactions with Materials and Atoms*, vol. 240, no. 1-2, pp. 117–123, 2005, ISSN: 0168583X. DOI: 10.1016/j.nimb.2005.06.098.

[10] H. Nakamura, Y. Shirakawa, S. Takahashi, and H. Shimizu, "Evidence of deep-blue photon emission at high efficiency by common plastic", *Epl*, vol. 95, no. 2, 2011, ISSN: 02955075. DOI: 10.1209/0295-5075/95/22001.

[11] C. A. Barrios, S. Carrasco, V. Canalejas-Tejero, *et al.*, "Fabrication of luminescent nanostructures by electron-beam direct writing of PMMA resist", *Materials Letters*, vol. 88, pp. 93–96, 2012, ISSN: 0167577X. DOI: 10.1016/j.matlet.2012.08.035.

[12] H. M. Lee, Y. N. Kim, B. H. Kim, S. O. Kim, and S. O. Cho, "Fabrication of luminescent nanoarchitectures by electron irradiation of polystyrene", *Advanced Materials*, vol. 20, no. 11, pp. 2094–2098, 2008, ISSN: 09359648. DOI: 10.1002/adma.200702221.

[13] P. Wang, Z. Li, L. Zhang, and L. Tong, "Electron-beam-activated light-emitting polymer nanofibers", vol. 38, no. 7, pp. 1040–1042, 2013.

[14] Y. K. Hong, D. H. Park, S. K. Park, *et al.*, "Tuning and enhancing photoluminescence of light-emitting polymer nanotubes through electron-beam irradiation", *Advanced Functional Materials*, vol. 19, no. 4, pp. 567–572, 2009, ISSN: 1616301X. DOI: 10.1002/adfm.200801088.

[15] K. Nagayama, T. Onuma, R. Ueno, K. Tamehiro, and H. Minoda, "Cathodoluminescence and Electron-Induced Fluorescence Enhancement of Enhanced Green Fluorescent Protein", *Journal of Physical Chemistry B*, vol. 120, no. 6, pp. 1169–1174, 2016, ISSN: 15205207. DOI: 10.1021/acs.jpcb.5b08138.

[16] K. Akiba, K. Tamehiro, K. Matsui, H. Ikegami, and H. Minoda, "Cathodoluminescence of green fluorescent protein exhibits the redshifted spectrum and the robustness", *Scientific Reports*, vol. 10, no. 1, pp. 1–7, 2020, ISSN: 20452322. DOI: 10.1038/s41598-020-74367-4. [Online]. Available: https://doi.org/10.1038/s41598-020-74367-4.

[17] H. Zhang, D. R. Glenn, R. Schalek, J. W. Lichtman, and R. L. Walsworth, "Efficiency of Cathodoluminescence Emission by Nitrogen-Vacancy Color Centers in Nanodiamonds", *Small*, vol. 13, no. 22, pp. 1–9, 2017, ISSN: 16136829. DOI: 10.1002/smll.201700543.

[18] S. R. Hemelaar, P. De Boer, M. Chipaux, *et al.*, "Nanodiamonds as multi-purpose labels for microscopy", *Scientific Reports*, vol. 7, no. 1, pp. 1–9, 2017, ISSN: 20452322. DOI: 10.1038/s41598-017-00797-2. [Online]. Available: http://dx.doi.org/10.1038/s41598-017-00797-2.

[19] D. R. Glenn, H. Zhang, N. Kasthuri, *et al.*, "Correlative light and electron microscopy using cathodoluminescence from nanoparticles with distinguishable colours", *Scientific Reports*, vol. 2, pp. 1–6, 2012, ISSN: 20452322. DOI: 10.1038/srep00865.

[20] W. Zhang, L. Melo, A. P. Hitchcock, and N. Bassim, "Electron beam damage of epoxy resin films studied by scanning transmission X-ray spectromicroscopy", *Micron*, vol. 120, no. December 2018, pp. 74–79, 2019, ISSN: 0968-4328. DOI: 10.1016/J.MICRON.2019.02.003. [Online]. Available: https://www.sciencedirect.com/science/article/pii/S0968432818304645.

[21] S. Bakhshandeh, H. M. Taïeb, R. Schlüßler, *et al.*, "Optical quantification of intracellular mass density and cell mechanics in 3D mechanical confinement", *Soft Matter*, vol. 17, no. 4, pp. 853–862, 2021, ISSN: 17446848. DOI: 10.1039/d0sm01556c.

[22] L. Reimer and S. E. Microscopy, "Physics of image formation and microanalysis", *Springer*, vol. 45, p. 135, 1985.

[23] Y. Kamura and K. Imura, "Fabrication method of two-photon luminescent organic nano-architectures using electron-beam irradiation", *Applied Physics Letters*, vol. 112, no. 243104, 2018, ISSN: 00029645. DOI: 10.1063/1.5025880.

[24] R. L. Clough, K. T. Gillen, G. M. Malone, and J. S. Wallace, "Color formation in irradiated polymers", *Radiation Physics and Chemistry*, vol. 48, no. 5, pp. 583–594, 1996, ISSN: 0969806X. DOI: 10.1016/0969-806X(96)00075-8.

[25] M. B. Prigozhin, P. C. Maurer, A. M. Courtis, *et al.*, "Bright sub-20-nm cathodoluminescent nanoprobes for electron microscopy", *Nature Nanotechnology*, vol. 14, no. 5, pp. 420–425, 2019, ISSN: 17483395. DOI: 10.1038/s41565-019-0395-0. [Online]. Available: http://dx.doi.org/10.1038/s41565-019-0395-0.

[26] K. Keevend, R. Krummenacher, E. Kungas, *et al.*, "Correlative Cathodoluminescence Electron Microscopy: Immunolabeling Using Rare-Earth Element Doped Nanoparticles", *Small*, vol. 16, no. 44, pp. 1–10, 2020, ISSN: 16136829. DOI: 10.1002/smll.202004615.

[27] R. I. Koning, A. S. Raja, R. I. Lane, A. J. Koster, and J. P. Hoogenboom, "Integrated Light and Electron Microscopy", *Correlative Imaging*, pp. 119–135, 2019. DOI: 10.1002/9781119086420.ch7.

[28] J.-D. .-. Acetarin, E. Carlemalm, E. Kellenberger, and W. Villiger, "Correlation of some mechanical properties of embedding resins with their behaviour in microtomy", *Journal of Electron Microscopy Technique*, vol. 6, no. 1, pp. 63–79, 1987, ISSN: 15530817. DOI: 10.1002/jemt.1060060109.

[29] A. C. Zonnevylle, R. F. Van Tol, N. Liv, *et al.*, "Integration of a high-NA light microscope in a scanning electron microscope", *Journal of Microscopy*, vol. 252, no. 1, pp. 58–70, 2013, ISSN: 00222720. DOI: 10.1111/jmi.12071.

[30] A. Ghasemi-Kahrizsangi, J. Neshati, H. Shariatpanahi, and E. Akbarinezhad, "Improving the UV degradation resistance of epoxy coatings using modified carbon black nanoparticles", *Progress in Organic Coatings*, vol. 85, pp. 199–207, 2015, ISSN: 03009440. DOI: 10.1016/j.porgcoat.2015.04.011. [Online]. Available: http://dx.doi.org/10.1016/j.porgcoat.2015.04.011.

[31] K. T. Arat, T. Klimpel, A. C. Zonnevylle, W. S. M. M. Ketelaars, H. C. T. H., and C. W. Hagen, "Charge-induced pattern displacement in E-beam lithography", *Journal of Vacuum Science & Technology B*, vol. 37, no. 5, p. 051603, 2019, ISSN: 2166-2746. DOI: 10.1116/1.5120631.

3

4

VACUUM COMPATIBLE FLUOROPHORES FOR INTEGRATED CLEM

4.1. INTRODUCTION

Integrated correlative light-electron microscopy (CLEM) unifies fluorescence (FM) and electron microscopy (EM) in a single system, which facilitates CLEM workflows by removing the need for sample transfer between different microscopes and, thus, easier region of interest retrieval [1]–[4]. Integration can be conducted such that both FM and EM share the same field of view, enabling automated and consistent registration accuracy [5]. This can be beneficial for CLEM across large scales or serial sections or for CLEM incorporating super-resolution localization [6]–[8]. However, a crucial challenge for CLEM in general, and integrated CLEM in particular, is in optimizing sample preparation protocols - to ensure adequate fluorescence preservation and electron contrast while maintaining ultrastructural fidelity.

CLEM-specific sample preparation protocols that balance fixation, EM staining, and fluorescence to reach an acceptable optimum have been developed [9]. Fluorescence from endogenous labels such as Green Fluorescent Protein can be preserved through fixation, polymer embedding, and staining [6]. Fixation and embedding resistant labels have also been reported (mEos variants, mKate, mWasabi, Staygold) [10], [11]. Post-embedding immuno-labeling with organic molecules provides an alternative route to combine EM signals and fluorescence with more traditional fixation and embedding protocols. For integrated CLEM, however, fluorescence signals are further impacted by the EM chamber's water- and oxygen-devoid vacuum, which may negatively impact the

fluorescence intensity. This is the case for proteins like the Green Fluorescent Protein, but many robust organic fluorophores also reserve their best performance to aqueous conditions.

The sensitivity of fluorophores to their environment is well documented [6]. It can be favorably exploited, for instance, by modifying its fluorescence properties in response to changes in temperature, hydration, voltage, pH, buffer media, presence of oxygen, and proximity to metals [12]–[15]. Dried, oxygen- and water-deprived conditions have typically been studied by comparing properties in a nitrogen atmosphere to those under ambient conditions. Particularly, the influence of oxygen on photobleaching, triplet, and other dark state population and depopulation dynamics has been studied in this way. However, for use in a vacuum, such as for integrated CLEM, results could be different compared to a pure nitrogen environment as water and oxygen levels at the sample may depend on the vacuum pressure. For example, Green Fluorescent Protein and Yellow Fluorescent Protein have been shown to optimally blink under a partial water vapor, permitting super-resolution localization measurements in an environmental integrated CLEM system [6]. The identification of fluorophores well-suited for vacuum and specifically for integrated CLEM has, to our knowledge, received limited attention. Karreman, Agronskaia, Van Donselaar, *et al.* [13] were the first to discuss fluorescence properties in the context of integrated CLEM, comparing the relative intensities of six commonly used fluorophores by immuno-labeling HUVEC cells and preparing them for EM by embedding and sectioning in Lowicryl, in dry N2 and wet conditions. They observed that TRITC demonstrated brighter fluorescence in N2. However, altered photobleaching and darkstate dynamics may also impact the total number of detectable photons. Rhodamine 6G, when encapsulated in a polymer matrix, offers a larger photon yield due to a lowered photobleaching rate in the absence of oxygen in a vacuum [14]. Many dyes like Alexa 488, Atto 488, Alexa 555, and Alexa 568 do not blink when devoid of oxygen [16]. At the same time, Alexa 647 does show blinking in the absence of oxygen, [16], [17], which enabled PALM imaging with an integrated FM-TEM system. However, this behavior was reported to be inconsistent across Lowicryl-embedded samples [18]. While such data has proven highly valuable to us and the integrated CLEM community, the large environment sensitivity of fluorophores complicates inference when comparing variable media and experimental settings.

Here we focus on the bare influence of vacuum on the fluorescence properties of five commonly used orange/red dyes (Atto 655, Atto 647N, Alexa 647, Alexa 594, and TRITC) at pressures of 3×10^{-5} to 7×10^{-7} mbar, which can be obtained by relatively short pumping times and is typical for, e.g., scanning electron microscopes (SEM) and thus integrated CLEM with SEM. We study the dyes at the single molecule level, directly deposited on glass, and unencumbered by additional media. Our interest is in the use of these dyes in integrated CLEM and for super-resolution techniques. Therefore, we restricted our selection to dyes with emission wavelengths > 560 nm as longer (red) emission wavelengths have reduced autofluorescence and electron-induced luminescence from embedding polymers [19]. Each of the investigated dyes also represents distinct categories of fluorophore structures, namely oxazines - Atto 655, carbopyronines – Atto 647 N, carbocyanines - Alexa 647, and rhodamines - Alexa 594 and TRITC [20]. Our results identify two dyes, Alexa 594 and TRITC, with higher photon yield and lower photo-

bleaching in a vacuum. In particular, TRITC has a three fold increase in total photon yield and ~10× longer half-life at the same excitation intensity in vacuum compared to ambient conditions. Thus, besides making this an excellent choice for integrated CLEM applications, our results also show that for applications where ambient conditions are not strictly required, photon output can be considerably improved by applying a vacuum that can be obtained with relatively straightforward experimental realization.

4.2. RESULTS AND DISCUSSION

We used an epi-fluorescence microscope with a vacuum-permissible sample chamber to directly compare fluorescence photon yield and photostability on the same sample under ambient and vacuum conditions. The chamber could be pumped up to ~10×10^{-7} mbar pressures. In practice, each dye was subjected to slightly different vacuum pressures in the range of 3×10^{-5} to 7×10^{-7} mbar owing to experimental timing. Still, the pressures remained consistent between measurements of the same dye. Spin-coated glass coverslips with a sparse dye distribution were used to localize and track single molecules. Figure 4.1 shows an example FM field-of-view of Atto 655 under a) ambient/atmospheric pressure and b) 5×10^{-6} mbar vacuum. The images show two distinct, previously unilluminated areas of the sample. While Atto 655 appears bright with a high(er) signal-to-background ratio in Figure 4.1(a), vacuum visibly reduces fluorescence intensity and the number of actively fluorescing molecules. Note that contrast and brightness settings were matched to aid visual comparison.
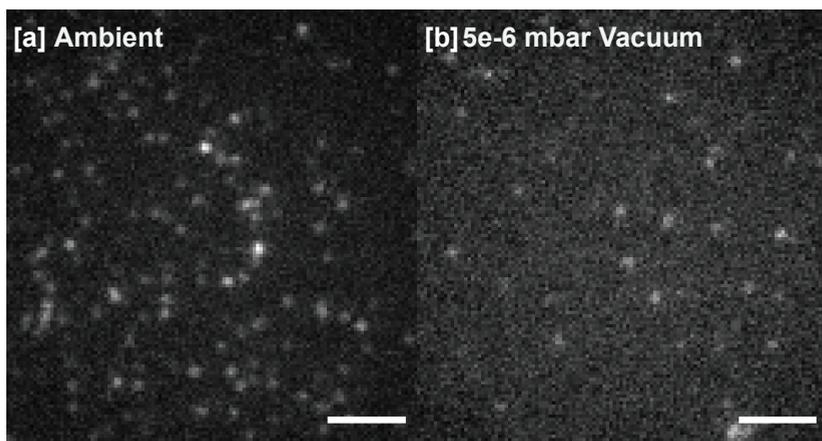

Figure 4.1: **Atto 655 shows reduced emission intensity and fewer fluorescent molecules under a vacuum.** Atto 655 molecules at (a) ambient and (b) vacuum (5×10^{-6} mbar) conditions with 638nm excitation wavelength and 185 Wcm^{-2} excitation intensity. Scale bar 5μm. Images were contrast-scaled for visibility.

CLEM experiments in our laboratory and by others [13], [21], [22] have empirically found similar fluorescence loss upon pumping to vacuum. The extent of such loss varied between dyes and their constituent biological samples, sometimes rendering them unusable for vacuum application. To this end, we evaluated the loss in fluorescence by

calculating the average photon count per molecule at measurement onset for both ambient and vacuum for all five dyes (Figure 4.2). Figure 4.2 shows that all examined dyes, except TRITC, appear dimmer in a vacuum for the same excitation intensity. Alexa 647 particularly stands out in signal loss. In this case, the excitation intensity in the vacuum needed to be roughly doubled (from 185 to 342 Wcm^{-2}) to restore the initial photon count to values measured under ambient conditions. The observations on TRITC, not suffering from this significant decrease in vacuum photon count per molecule, are in accordance with the results reported by [23], who compared the dye under dry N2 gas and wet conditions.
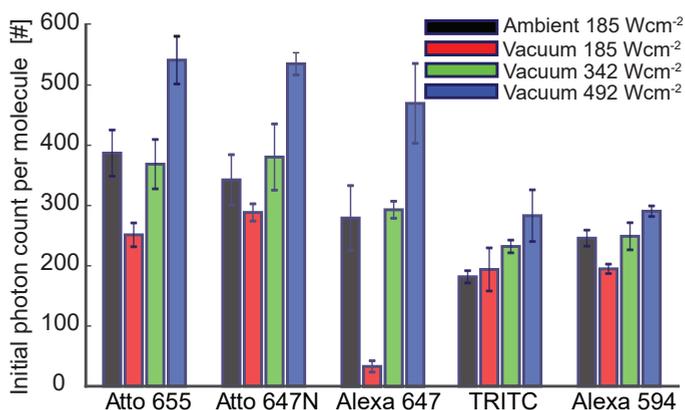

Figure 4.2: **TRITC retains photon count per molecule (at onset) in both ambient and vacuum environments.** Average photon count per molecule at onset for ambient (excitation: 185 Wcm^{-2}) and vacuum conditions (excitation: 185, 342 and 492 Wcm^{-2}). Error bars represent 95% confidence intervals.

An ideal fluorophore shows an initial high photon yield and sustains this over long image acquisition periods. As oxygen is known to be a main contributor to photobleaching, we next investigate the photo-stability for these five dyes in the dried, oxygen-absent vacuum environment. Following similar analysis as in Hulleman, Li, Gregor, *et al.* [24] Figure 4.3 shows photobleaching curves depicted by the surviving molecular fraction with time. This reveals that three out of five examined dyes, namely Alexa 594, Alexa 647, and TRITC, have slower photobleaching in vacuum than in ambient conditions.

All photobleaching curves were fit to a double exponential function as indicated in Figure 4.3. Under ambient conditions, it is clear that Atto 647N and Atto 655 are highly photostable dyes, with measured molecular half-life, i.e., the time taken to halve the fluorescing population, of 238 s and 248 s, respectively, markedly higher than those for Alexa 594 (68 s), Alexa 647 (120 s), and TRITC (144 s). Pumping to vacuum impacts the molecular survival of all dyes. Both Atto dyes bleach faster in a vacuum; while Atto 647N drops to nearly half the ambient molecular-half life, Atto 655 has a modest rise in half-life. Vacuum appears to cause a sharp initial loss of ~30% of fluorescing molecules within the first 25s. After that, the decay weakens, eventually becoming slower than the ambient curve after the point of intersection at ~210s. The rapid initial fluorophore bleaching in a vacuum is particularly clear in the photobleaching curves of Atto 655, Atto 647N,
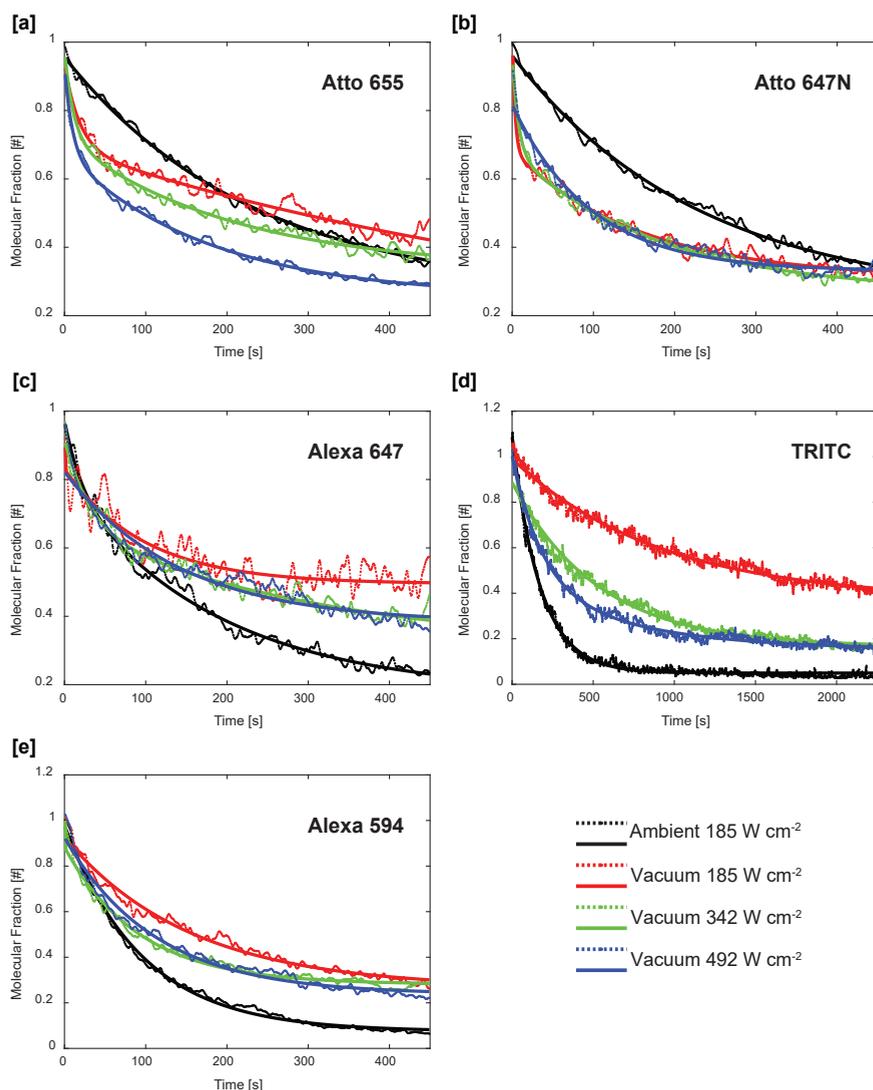
Figure 4.3: **Alexa 647, Alexa 594, and TRITC show lower photo-bleaching in a vacuum.** Photobleaching curves are represented as normalized molecular fraction vs time for (a)-(e) Atto 655, Alexa 647, Atto 647N, TRITC, and Alexa 594, respectively. Data was smoothed by a Gaussian weighted moving average filter and fit to a double-exponential function with an offset.

and Alexa 647 (Figure 4.3 a-c), suggesting more complex decay dynamics under oxygen-deprived vacuum conditions. Contrary to Atto dyes, Alexa 647, TRITC, and Alexa 594 show an increased molecular half-life in a vacuum. Whereas Alexa 647 and Alexa 594 yield 3.4× and 2.5× increase, respectively, TRITC displays a remarkable 10x (791s) improvement in molecular half-life.

Compared to results from Hulleman, Li, Gregor, *et al.* [24] , Atto 647N has a 6-fold increase in ambient half-life (132s instead of 52s) for a 1.3× lower excitation intensity (185 Wcm^{-2}instead of 240 Wcm^{-2}). The corresponding mean photon yield is also 2x higher (Figure 4.4 4.5*10^4 instead of 2.1*10^4). Alexa 647 shows a doubling of half-life time of 67 seconds at 185 Wcm^{-2}. We hypothesize that the difference in Atto 647N may stem from its sensitivity to the surface properties of the coverslip (borosilicate glass was used in our study instead of quartz), the spectral filtering of emitted fluorescence, the age and storage of the dye solution and the residual humidity in the vacuum chamber.
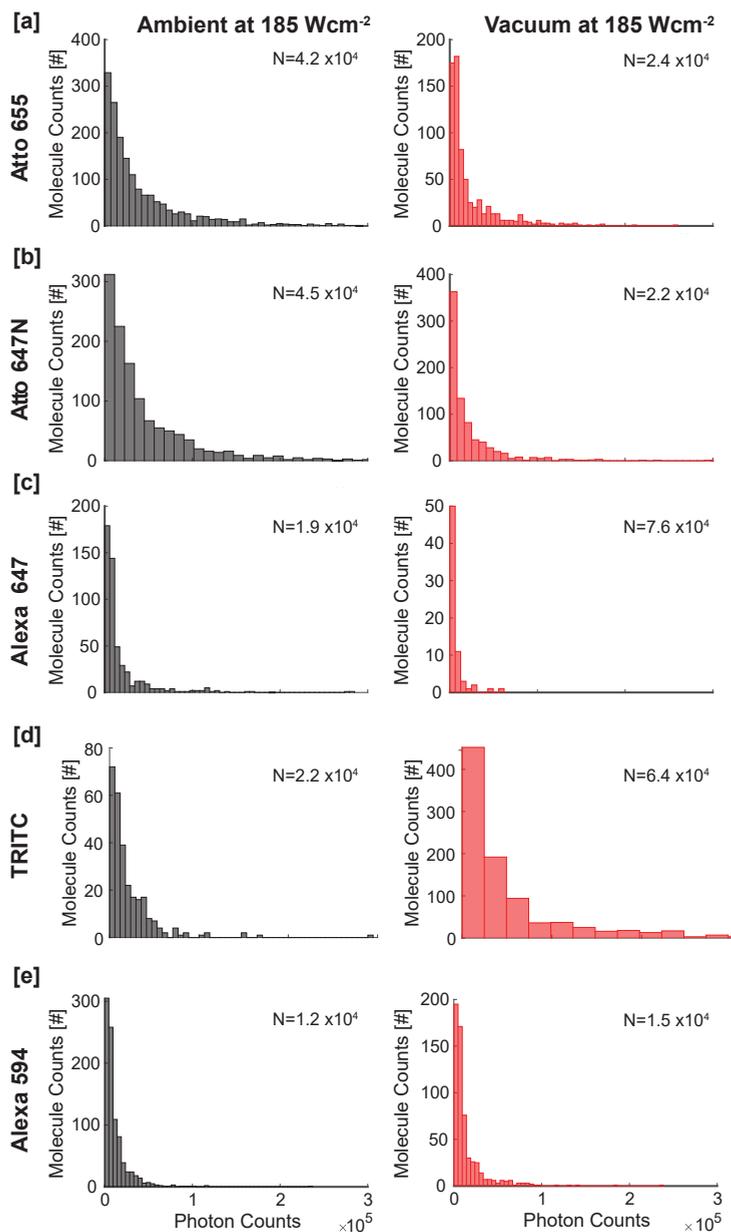
4

Figure 4.4: **TRITC shows ~3-fold increase in mean photon yield under vacuum.** Histogram of molecule versus photon counts under ambient (black) and vacuum (red) conditions at 185 Wcm^{-2} excitation intensity. (a)-(e) Atto 655, Alexa 647, Atto 647N, TRITC and Alexa 594 respectively. Legend denotes the mean photon yield as obtained from a single exponential distribution fit. Note: TRITC had a 2250s acquisition time, whereas the remaining dyes were measured for 450s.
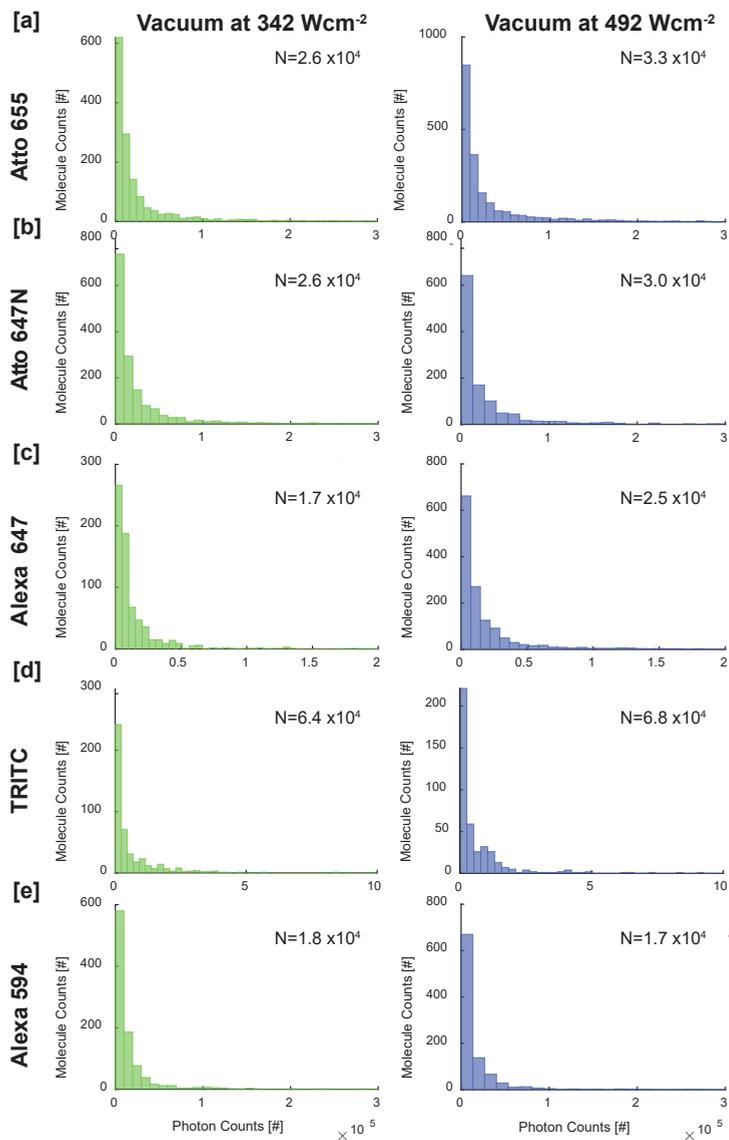
4

Figure 4.5: **TRITC shows ~3-fold increase in mean photon yield under vacuum.** Histogram of molecule versus photon counts under vacuum conditions at 342 Wcm^{-2} and 492 Wcm^{-2} excitation intensity. (a)-(e) Atto 655, Alexa 647, Atto 647N, TRITC and Alexa 594 respectively. Legend denotes the mean photon yield as obtained from a single exponential distribution fit. Note: TRITC had a 2250s acquisition time, whereas the remaining dyes were measured for 450s.

The slower photobleaching observed in a vacuum suggests that the total number of photons that can be extracted from a single dye molecule may be higher despite a lower initial photon yield. Figure 4.4 shows histograms indicating the total number of photon counts detected per molecule for all five examined dyes. The data was fit to a single exponential distribution through a maximum likelihood estimator, where the mean of the distribution reflects the mean photon yield with a 95% confidence interval. This value was also equivalent to the arithmetic mean of the respective dataset. Given the unaltered initial photon count per molecule in vacuum (Figure 4.2), TRITC stands out with a histogram shift towards higher photon counts. Figure 4.6a shows that for the same excitation intensity, Atto 655, Alexa 647, and Atto 647N show a photon budget loss of 43%, 51%, and 60%, respectively. Next to TRITC, Alexa 594 shows a gain in the total number of emitted photons before photobleaching in vacuum (25% compared to 191% for TRITC). Thus, in the case of Alexa 594, the enhanced photostability in vacuum compensates for the initial reduction in photon yield. Further, the data confirm the superior performance of TRITC in a vacuum, where roughly three times more photons can be extracted per dye molecule after pumping to a vacuum. Note that TRITC had a 2225s acquisition duration (5× longer than the rest) to account for its lowered vacuum photobleaching rates and successfully fit a biexponential decay.
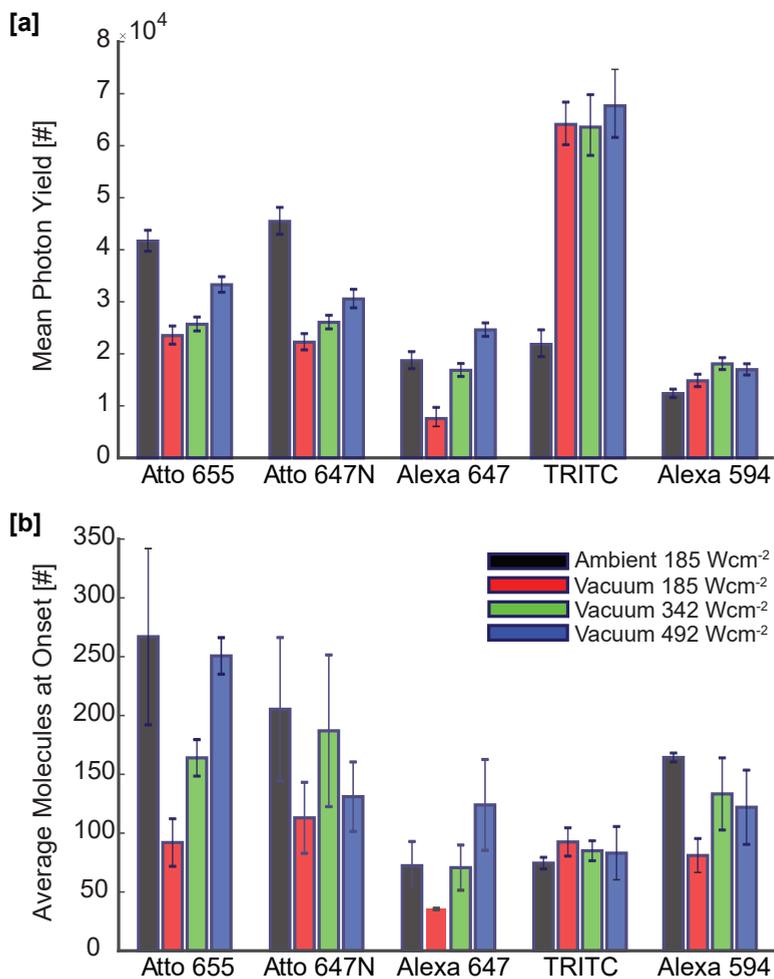
4

[a]

[b]

Figure 4.6: **TRITC stands out with three times more detected photons in vacuum for a similar number of emissive/detected molecules.** Comparative plots showing (a) mean photon yield and (b) average number of molecules at measurement onset for each of the five dyes. Error bars indicate 95% confidence intervals.

While the choice of an integrated CLEM dye is dictated by its vacuum photon yield and photostability, the relative number of emissive fluorescent molecules and their respective photon counts are also of significance. They respectively indicate changes to molecular density and image quality (signal to background) when moving from ambient to vacuum (or to higher excitations). This is relevant for integrated CLEM since samples are typically inspected under ambient conditions before the final vacuum imaging. Next to the average mean photon yield, Figure 4.6b shows the average number of molecules detected at the measurement's onset, i.e., in the first frame. If we compare this data with the average photon count per molecule at the onset of measurements (Figure 4.2), we see a correlation between lower photon count and fewer molecules passing the detection threshold. Nevertheless, some interesting additional observations can be made. First, we see that TRITC is the only examined dye to show a sustained number of emissive molecules under vacuum across environment and excitations, thus, the enhanced photostability seems a property of the entire molecular distribution. Second, Alexa 647 presents a dual case for use in a vacuum. Pumping to vacuum gives a 3.4× increase in molecular half-life (Figure 4.3c) but with a concomitant 51% loss in mean photon budget (Figure 4.6a). At the onset, Alexa 647 also has less than 50 molecules and less than 50 photons per molecule (Figure 4.6b & Figure 4.2), indicating both dismal detectable molecular density and image quality, which does not compensate for the improved survival. Statistics in vacuum at 185 Wcm^{-2} for Alexa 647 remain the poorest of all tested dyes. However, upon increasing excitation intensity by a factor of 2.7, the photon budget rises to 132% of the ambient values while still improving half-life by 1.7x. Higher photon-excitation may push dormant molecules into an emissive state, thus making it suitable for use in a vacuum if there is no excitation power limitation, i.e., if instead of standard multi-wavelength LED, which is, e.g., the workhorse in routine CLEM, laser illumination could be implemented.

Finally, our single-molecule approach allowed us to extend our analysis to the blinking behavior of the vacuum-superior dyes, Alexa 594 and TRITC. Blinking, or fluorescent intermittency, occurs when the molecule stochastically and reversibly transitions to a non-emissive or dark state. Fast, sub-millisecond blinking may occur due to triplet state population and depopulation, but longer timescale blinking, with typical lifetimes in the millisecond range [25] or even extending to seconds or longer, may occur depending on the nature of the dark state and its (de)population dynamics. While blinking complicates fluorescence interpretation, the reversible switching between distinct on and off states can be attractive for super-resolution methods [26]. Moreover, blinking kinetics can be highly sensitive to the molecular environment, particularly the presence of oxygen. Interestingly, Peddie et al. have noted that Green Fluorescent Protein displays optimized blinking conditions under a partial vacuum for super-resolution localization and exploited this in integrated CLEM [6].

We inspected two characteristics, namely T_{off}, the time spent in a non-fluorescing state, and the average number of blinks, where one blink is the complete transition from an on-off-on state during its lifetime or until the end of image acquisition. We note that our 900ms time resolution only suffices to examine the relatively long-lived dark states (in the order of seconds) and thus present underestimated blinking rates. However, we can still identify trends in the influence of vacuum and increasing excitation compared

to ambient conditions. Figure 4.7 shows that for the same excitation intensity, the average number of blinks increases under vacuum for both Alexa 594 and TRITC. This is accompanied by a reduction in T_{off}, particularly prominent for TRITC. A correlation between increased blinking and decreased T_{off} seems valid and reasonable in that shorter dark state lifetimes mean faster repopulation of the ground state from where the molecule is excitable again. However, this result is surprising for two reasons: a) it occurs in a vacuum without oxygen, and b) there is an increase in T_{off} with excitation intensity.

Firstly, oxygen can impact fluorescence as a triplet state quencher, which shortens triple state lifetimes [27], [28], but typical triplet dynamics are considered to be below our temporal resolution. As the triplet state is often considered an intermediate to a population of other dark states, increased triplet lifetimes in a vacuum may thus increase the chance for a population of longer-lived, and thus observable, dark states [29]. Furthermore, permanent bleaching may be caused by direct oxidation or indirect radical reactions [30]. Thus, oxygen removal improves photostability, as evidenced in our results. Techniques using oxygen-scavenging systems, reducing agents, antioxidants, and chemical additives to recover reactive intermediates are used to improve dye stability in liquid [29], [30]. The observation of decreasing T_{off} in a vacuum suggests the presence of a dark state that is stabilized by or populated via interaction with, e.g., oxygen.

Secondly, faster cycling between ground and excited states occurs with increasing excitation intensity. Consequently, depopulating the emissive state to higher radiative states or dark states is more likely, thereby shortening the on times. However, the excitation dependence of the off times suggests an optically excitable transition between dark states, thus increasing residence time in dark states. The observation of prolonged dye stability and increased total photon budget, which may even occur despite the dimmer appearance of a dye in a vacuum, can be interesting for applications where ambient conditions are not strictly needed, e.g., in nanophotonics. Our prime interest is in integrated CLEM, where the vacuum is a must for electron microscopy. TRITC then appears as a preferred candidate for (immuno-) labeling where the total acquirable photon budget outperforms even that under ambient conditions and more photostable Atto dyes. Thus, even for regular CLEM or another labeling of fixed materials, the use of a vacuum-optimal dye like TRITC combined with fluorescence inspection in a simple vacuum setup is attractive when photon budget matters. Our results on TRITC are in line with the work of Karreman, Agronskaia, Van Donselaar, *et al.* [13], who reported that TRITC, when used for immuno-labeling HUVECS embedded in Lowicryl, showed 1.46 ± 0.4 brightness increase in dry N2 relative to water. This is approximately half of our measured values. A direct comparison is not feasible owing to the vastly different experimental protocols. Part of the brightness reduction observed by Karreman, Agronskaia, Van Donselaar, *et al.* [13] may be caused by the embedding procedure. In this respect, our results display the bare effect of a $\sim 1 \times 10^{-6}$ mbar vacuum. They could thus pave the way to a more detailed investigation of the origins of the observed vacuum behavior of these and other dyes. For example, additional environmental factors may play a role besides oxygen deprivation, leading to slight differences between those observed here (vacuum), in [13] (dry N2), and in [16] (oxygen-scavenging system). Contrary to current observations, for TRITC, computational work has shown that of the different solvent-dependent isomeric forms, only the non-fluorescent lactone isomer is present in vacuum [31]. The

difference in initial photon yield and vacuum enhancement between TRITC, an isothiocyanate derivative of rhodamine, and Alexa 594, a sulfonated rhodamine, also calls for additional research into the origins of the observed behaviors. This would benefit further optimization of rhodamine-based or other dyes for use in a vacuum or integrated CLEM.
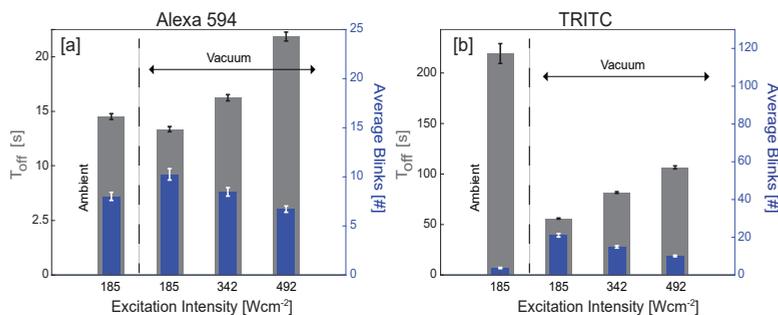

Figure 4.7: **Vacuum enhances blinking while reducing long-lived dark state residence times (T_{off}).** (a) Average time spent in non-emissive dark states (T_{off}; grey data, left axis) for Alexa 594, together with the average number of blinking events (blue data, right axis). (b) The same data for TRITC where a clear drop in T_{off} for vacuum versus ambient is observed together with increased blinking. For higher excitation intensities in a vacuum, T_{off} increases while blinking decreases.

The combination of prolonged photostability and increased blinking may benefit fluorescence super-resolution techniques based on localization approaches. For CLEM, fluorescence super-resolution can bridge the two orders of magnitude gap between intrinsic FM and EM resolution, allowing better localization of labeled target molecules within the biological ultrastructure. Conducting these super-resolution approaches in integrated CLEM offers the benefit of a consistent, high FM-EM registration accuracy, which is needed to avoid additional overlay errors to the localization inaccuracy. While our initial interest was in finding a bright and photostable dye in a vacuum for an approach where the focused electron beam is used to bleach or otherwise manipulate molecular fluorescence to achieve super-resolution (the eSRM technique, Chapter 2 in this thesis), the lab is also investigating the direct use of blinking on TRITC- or Alexa 594-labeled samples to achieve super-resolution in integrated CLEM. This could mitigate the need for adjusting vacuum partial pressure by injecting water vapor in an environmental SEM to achieve optimized blinking, as used by Peddie, Domart, Snetkov, *et al.* [6]. However, it would be at the expense of needing an immuno-labeling strategy. Concerning blinking in a vacuum, we note that the current blinking analysis evaluated a generic off-state that was longer than 17s at minimum. The intensity threshold demarcating on and off states adds additional bias, especially in low signal cases. Further investigation may thus consider higher temporal resolution, possibly followed by autocorrelation analysis to describe decay kinetics and extract on-off times.

4.3. Conclusion

We have compared five common organic dyes' fluorescence photon yield and photostability under ambient and vacuum conditions. It was found that TRITC stands out for use in a vacuum. TRITC showed unaltered brightness with improved photostability, leading to a three-fold increase in total photon counts that can be obtained in a vacuum compared to ambient conditions. The other investigated dyes dim in a vacuum, but, e.g., Alexa 594, which shows reduced photobleaching in a vacuum, can still lead to an increase in the total amount of detected photons. In addition, these dyes displayed enhanced blinking with reduced off times in a vacuum. Our results are particularly interesting for selecting dyes as labeling material in integrated CLEM and may further pave the way for new approaches to incorporate super-resolution FM within integrated CLEM. More generally, these results show that any application where an ambient or liquid environment is not per se needed, e.g., in nano- or quantum photonics, may benefit from using an ~1×10^{-6} mbar vacuum in combination with the selection of a vacuum-optimized dye to increase the total obtainable photon budget.

4.4. Experimental Methods

4.4.1. Experimental Setup

For this study, a standard epi-illumination fluorescence microscope was used. The excitation path consisted of a Cobolt C-FLEX C4 laser (Hübner Photonics) with 561nm (for Alexa 594 and TRITC) and 638nm (for the rest) lines. The laser was followed by beam steering mirrors (Thorlabs BB1-E02), a quarter-wave plate (AQWP05M-600, elliptical 3:2 polarization), beam expanders (-50mm Thorlabs LC1715-B, 150mm Thorlabs LA1433-B), and a front lens (200mm Thorlabs LB1945-B). The front lens focused the laser onto the objective's back focal plane (0.7NA Nikon CFI S Plan Fluor ELWD 60XC) via dichroic mirrors. Sample fluorescence is transmitted by the dichroic mirror, filtered by an emission filter, and focused by a tube lens (Thorlabs ITL200) onto the EMCCD detector (Andor iXON Ultra 888). The samples were held in place between magnetic snap enclosure rings inside a vacuum chamber and imaged through a 0.7mm thick quartz window. The following sets of excitation, dichroic, and emission filters were used per laser wavelength. 638nm excitation wavelength - FF01-390/482/532/640 excitation filter, Di02-R635 dichroic and FF01-446/510/581/703 emission filter. 561nm excitation wavelength - ET560/40× excitation filter, FF409/493/573/652-Di02-25x36 dichroic and ET630/75M emission filter. The vacuum chamber was pumped to pressures between 3×10^{-5} to 7×10^{-7} mbar and vented by the influx of atmospheric air. Chamber pressure typically stabilizes to 3×10^{-5} mbar within 20 minutes and progressively drops below 1×10^{-7} mbar when pumped overnight. Excitation power was measured by a power meter after the objective lens. Laser source powers were adjusted per excitation wavelength and compensated for surface reflection losses to maintain consistent powers at the sample. Excitation intensity was calculated by dividing the measured power by the illuminated area on the detector using the formula: Power density (Wcm^{-2}) = (255/Beam diameter^2(mm)) × Measured power(W). This calculation results in a small error percentage as the beam profiles were not perfectly Gaussian.

4.4.2. SAMPLE PREPARATION

12mm diameter borosilicate glass coverslips (Carl Roth GmbH + Co. KG) were sonicated for 10 minutes in >90% Acetone, followed by 99% Isopropyl alcohol (IPA) and dried in a stream of Nitrogen. Graded dilutions in IPA were prepared from the stock solutions of the following dyes: Atto 647N (—NHS ester, Sigma Aldrich—), Alexa 647 NHS Ester (—Succinimidyl Ester, Thermo Fisher Scientific—), Atto 655 NHS Ester (—Sigma Aldrich—), TRITC (—IgG conjugated Thermo Fisher Scientific—) and Alexa 594 NHS Ester (—Succinimidyl Ester, Thermo Fisher Scientific—). The final concentration was chosen to achieve a sufficient number (~100-400) of sparse single molecules within the $87{\times}87\mu m$ imaging field of view at room temperature and ambient conditions. NHS Ester dyes had a final concentration of 0.1fM (Alexa 594) and 1fM (Alexa 647, Atto 655, and Atto 647N) while IgG conjugated TRITC was ~35pM. 20μL of the final solution was deposited on cleaned glass coverslips and spin-coated at 3000rpm for 60 seconds using either static (NHS ester dyes) or dynamic dispensing (IgG conjugated TRITC with $\sim10^3$ times heavier linkers). The spin coating settings were experimentally determined to have a sparse sample (minimum distance between molecules >500nm).

4.4.3. IMAGE ACQUISITION AND ANALYSIS

ACQUISITION

For each dye, the image series was obtained under four conditions: Ambient at 185 W^{-2} and Vacuum at 185 Wcm^{-2}, 342 Wcm^{-2} and 492 Wcm^{-2}. Each measurement was repeated thrice (twice for TRITC) for statistical relevance. Images were recorded with an exposure time of 900ms, with a total measurement duration of ~37.5 minutes for TRITC (2499 frames) and ~7.5 minutes (499 frames) for the remaining dyes. Electron multiplier gain was set to 100, and the detector response included a bias/offset at 500 with a sensitivity of 1.7 photoelectrons per Analog-Digital Unit (ADU). For Atto 647N, Alexa 647, and Atto 655, the diaphragm beam shutter (Thorlabs) was manually controlled to expose the sample, whereas an automatic TTL input (~5-10ms opening time) was used for Alexa 594 and TRITC. The partially exposed frames in the case of manual control were not analyzed.

ANALYSIS

Molecules were identified and tracked in two steps using ThunderSTORM (ImageJ plugin version 1.3). Firstly, single molecules were localized by standard out-of-the-box ThunderSTORM settings using a symmetric 2D Gaussian point spread function model. Each image series is drift-corrected via cross-correlation and filtered. Multiparameter filtering is applied to eliminate outliers and poor/false localizations. Duplicate fits within a distance smaller than their respective uncertainties are filtered by retaining the molecule with the smallest uncertainty. A region of interest filter is used to account for molecules in the central illumination area (43μm, i.e., 200 pixels in the x & y dimensions). Furthermore, only molecule fits with a localization uncertainty < 100 nm, intensity >100 photons, and standard deviation < 400nm were retained, where the intensity refers to the integrated photons of the fitted Gaussian respectively. The image ADUs were converted

to photons by the following expression: Intensity (photons) = Sensitivity/EM gain (Intensity (ADU) – Offset). Note that with the Gaussian point spread function integration, one underestimates the true photon count by about 20% [32].

The above method identifies the number of active molecules and their individual photon counts per frame. Molecular fractions were calculated by normalizing the number of detected molecules per frame to the number of detected molecules at onset (i.e., t = 900 ms). The resulting curves were best fit to a double exponential decay with offset as per the following expression: $ae^{-bt} + ce^{-dt} + e$, with fit parameters a,b,c,d, and e. Secondly, fitted molecules were merged over a 2-pixel radius across frames for molecular tracking. To allow blinking, molecules were permitted to be off for the entire duration of the image series. Additionally, no limits were placed on the maximum number of consecutive on-frames. Isolated detections were omitted as they were assumed to be spurious. The resultant data shows the total photons emitted per tracked molecule before photobleaching or until the end of image acquisition. To calculate the mean photon yield, all dyes were subjected to a 2500 photon count threshold to remove spurious/weak localizations. ThunderStorm data output (individual & tracked) was exported as .csv files for further analysis in MATLAB Release R2019a (The MathWorks, Inc.).

BIBLIOGRAPHY

[1] P. de Boer, J. P. Hoogenboom, and B. N. G. Giepmans, "Correlated light and electron microscopy: ultrastructure lights up!", *Nature Methods*, vol. 12, no. 6, pp. 503–513, 2015, ISSN: 1548-7091. DOI: 10.1038/nmeth.3400. [Online]. Available: http://www.nature.com/doifinder/10.1038/nmeth.3400.

[2] A. C. Zonnevylle, R. F. Van Tol, N. Liv, *et al.*, "Integration of a high-NA light microscope in a scanning electron microscope", *Journal of Microscopy*, vol. 252, no. 1, pp. 58–70, 2013, ISSN: 00222720. DOI: 10.1111/jmi.12071.

[3] N. Liv, A. C. Zonnevylle, A. C. Narvaez, *et al.*, "Simultaneous Correlative Scanning Electron and High-NA Fluorescence Microscopy", *PLoS ONE*, vol. 8, no. 2, pp. 1–9, 2013, ISSN: 19326203. DOI: 10.1371/journal.pone.0055707.

[4] F. J. Timmermans and C. Otto, "Contributed Review: Review of integrated correlative light and electron microscopy", *Review of Scientific Instruments*, vol. 86, no. 1, 2015, ISSN: 10897623. DOI: 10.1063/1.4905434. [Online]. Available: http://dx.doi.org/10.1063/1.4905434.

[5] M. T. Haring, N. Liv, A. C. Zonnevylle, *et al.*, "Automated sub-5 nm image registration in integrated correlative fluorescence and electron microscopy using cathodoluminescence pointers", *Scientific Reports*, vol. 7, no. August 2016, p. 43 621, 2017, ISSN: 2045-2322. DOI: 10.1038/srep43621. [Online]. Available: http://www.nature.com/articles/srep43621.

[6] C. J. Peddie, M. C. Domart, X. Snetkov, *et al.*, "Correlative super-resolution fluorescence and electron microscopy using conventional fluorescent proteins in vacuo", *Journal of Structural Biology*, vol. 199, no. 2, pp. 120–131, 2017, ISSN: 10958657. DOI: 10.1016/j.jsb.2017.05.013. [Online]. Available: http://dx.doi.org/10.1016/j.jsb.2017.05.013.

[7] L. M. Collinson, E. C. Carroll, and J. P. Hoogenboom, "Correlating 3D light to 3D electron microscopy for systems biology", *Current Opinion in Biomedical Engineering*, vol. 3, pp. 49–55, 2017, ISSN: 24684511. DOI: 10.1016/j.cobme.2017.10.006. [Online]. Available: https://doi.org/10.1016/j.cobme.2017.10.006.

[8] R. I. Koning, A. S. Raja, R. I. Lane, A. J. Koster, and J. P. Hoogenboom, "Integrated Light and Electron Microscopy", *Correlative Imaging*, pp. 119–135, 2019. DOI: 10.1002/9781119086420.ch7.

[9] X. Heiligenstein and M. S. Lucas, "One for all, all for one: A close look at in-resin fluorescence protocols for clem", *Frontiers in Cell and Developmental Biology*, vol. 10, p. 1369, 2022.

[10] H. Tanner, O. Sherwin, and P. Verkade, "Labelling strategies for correlative light electron microscopy", *Microscopy Research and Technique*, 2023.

[11] R. Franzkoch, S. Wilkening, V. Liss, *et al.*, "Rapid in-epon clem: Combining fast and efficient labeling of self-labeling enzyme tags with em-resistant janelia fluor dyes and staygold", *Heliyon*, vol. 10, no. 7, 2024.

[12] B. Kozankiewicz and M. Orrit, "Single-molecule photophysics, from cryogenic to ambient conditions.", *Chemical Society reviews*, vol. 43, no. 4, pp. 1029–43, 2014, ISSN: 1460-4744. DOI: 10.1039/c3cs60165j. [Online]. Available: http://pubs.rsc.org/en/content/articlehtml/2014/cs/c3cs60165j.

[13] M. A. Karreman, A. V. Agronskaia, E. G. Van Donselaar, *et al.*, "Optimizing immuno-labeling for correlative fluorescence and electron microscopy on a single specimen", *Journal of Structural Biology*, vol. 180, pp. 382–386, 2012. DOI: 10.1016/j.jsb.2012.09.002.

[14] L. A. Deschenes and D. A. Vanden Bout, "Single molecule photobleaching: Increasing photon yield and survival time through suppression of two-step photolysis", *Chemical Physics Letters*, vol. 365, no. 5-6, pp. 387–395, 2002, ISSN: 00092614. DOI: 10.1016/S0009-2614(02)01490-2.

[15] R. J. Moerland and J. P. Hoogenboom, "Subnanometer-accuracy optical distance ruler based on fluorescence quenching by transparent conductors", *Optica*, vol. 3, no. 2, pp. 112–117, 2016.

[16] G. T. Dempsey, J. C. Vaughan, K. H. Chen, M. Bates, and X. Zhuang, "Evaluation of fluorophores for optimal performance in localization-based super-resolution imaging", *Nature Methods*, vol. 8, no. 12, pp. 1027–1040, 2011, ISSN: 15487091. DOI: 10.1038/nmeth.1768.

[17] L. Nahidiazar, A. V. Agronskaia, J. Broertjes, B. D. Van Broek, and K. Jalink, "Optimizing imaging conditions for demanding multi-color super resolution localization microscopy", *PLoS ONE*, vol. 11, no. 7, pp. 1–18, 2016, ISSN: 19326203. DOI: 10.1371/journal.pone.0158884.

[18] S. Mohammadian, A. V. Agronskaia, G. A. Blab, *et al.*, "Integrated super resolution fluorescence microscopy and transmission electron microscopy", *Ultramicroscopy*, vol. 215, no. May, p. 113 007, 2020, ISSN: 18792723. DOI: 10.1016/j.ultramic.2020.113007. [Online]. Available: https://doi.org/10.1016/j.ultramic.2020.113007.

[19] A. Srinivasa Raja, P. de Boer, B. N. Giepmans, and J. P. Hoogenboom, "Electron-Beam Induced Luminescence and Bleaching in Polymer Resins and Embedded Biomaterial", *Macromolecular Bioscience*, vol. 2100192, pp. 1–10, 2021, ISSN: 16165195. DOI: 10.1002/mabi.202100192.

[20] T. F. S. .-. US. "Fluorophores". (2023), [Online]. Available: https://www.thermofisher.com/nl/en/home/life-science/cell-analysis/fluorophores/.

[21] C. J. Peddie, K. Blight, E. Wilson, *et al.*, "Correlative and integrated light and electron microscopy of in-resin gfp fluorescence, used to localise diacylglycerol in mammalian cells", *Ultramicroscopy*, vol. 143, pp. 3–14, 2014.

[22] C. J. Peddie, N. Liv, J. P. Hoogenboom, and L. M. Collinson, "Integrated light and scanning electron microscopy of gfp-expressing cells", in *Methods in cell biology*, vol. 124, Elsevier, 2014, pp. 363–389.

[23] M. Karreman, "Lights Will Guide You - Sample Preparation and Applications for Integrated Laser and Electron Microscopy", 2013.

[24] C. N. Hulleman, W. Li, I. Gregor, B. Rieger, and J. Enderlein, "Photon Yield Enhancement of Red Fluorophores at Cryogenic Temperatures", *ChemPhysChem*, vol. 19, no. 14, pp. 1774–1780, 2018, ISSN: 14397641. DOI: 10.1002/cphc.201800131.

[25] C. E. Aitken, R. A. Marshall, and J. D. Puglisi, "An oxygen scavenging system for improvement of dye stability in single-molecule fluorescence experiments", *Biophysical Journal*, vol. 94, no. 5, pp. 1826–1835, 2008, ISSN: 15420086. DOI: 10.1529/biophysj.107.117689.

[26] J. Vogelsang, C. Steinhauer, C. Forthmann, *et al.*, "Make them blink: Probes for super-resolution microscopy", *ChemPhysChem*, vol. 11, no. 12, pp. 2475–2490, 2010, ISSN: 14397641. DOI: 10.1002/cphc.201000189.

[27] S. Van De Linde, I. Krstić, T. Prisner, S. Doose, M. Heilemann, and M. Sauer, "Photoinduced formation of reversible dye radicals and their impact on super-resolution imaging", *Photochemical and Photobiological Sciences*, vol. 10, no. 4, pp. 499–506, 2011, ISSN: 14749092. DOI: 10.1039/c0pp00317d.

[28] C. Grewer and H.-D. Brauer, "Mechanism of the triplet-state quenching by molecular oxygen in solution", *The Journal of Physical Chemistry*, vol. 98, no. 16, pp. 4230–4235, 1994.

[29] J. Vogelsang, R. Kasper, C. Steinhauer, *et al.*, "A reducing and oxidizing system minimizes photobleaching and blinking of fluorescent dyes", *Angewandte Chemie - International Edition*, vol. 47, no. 29, pp. 5465–5469, 2008, ISSN: 14337851. DOI: 10.1002/anie.200801518.

[30] A. P. Demchenko, "Photobleaching of organic fluorophores: Quantitative characterization, mechanisms, protection", *Methods and Applications in Fluorescence*, vol. 8, no. 2, pp. 0–43, 2020, ISSN: 20506120. DOI: 10.1088/2050-6120/ab7365.

[31] A. Pedone and V. Barone, "Unraveling solvent effects on the electronic absorption spectra of TRITC fluorophore in solution: A theoretical TD-DFT/PCM study", *Physical Chemistry Chemical Physics*, vol. 12, no. 11, pp. 2722–2729, 2010, ISSN: 14639076. DOI: 10.1039/b923419e.

[32] R. Ø. Thorsen, C. N. Hulleman, M. Hammer, D. Grünwald, S. Stallinga, and B. Rieger, "Impact of optical aberrations on axial position determination by photometry", *Nature methods*, vol. 15, no. 12, pp. 989–990, 2018.

4

<div style="text-align: right; font-size: 4em; font-weight: bold;">5</div>

FLUORESCENT REPORTERS FOR CHARGE TRANSPORT IN INSULATORS

5.1. INTRODUCTION

The technique of electron beam-induced fluorescence super-resolution (eSRM) involves manipulating fluorescence emission locally. The principle of eSRM has been established, and its potential for super-resolution has been demonstrated. However, our experimental observations (see Chapter 2 and below) have revealed an unexpected, long-range electron-induced bleaching effect that extends hundreds of nanometers from the stationary beam incidence. Figure 5.1 shows the influence of a focused electron beam with a 1keV landing energy and 13pA current, centrally parked in the fluorescence field-of-view FOV for 700ms. Panels (a) and (b) show wide-field fluorescence (FM) images of 50nm polystyrene microspheres before and after electron exposure. Panel (c) shows the electron microscopy image (EM) acquired immediately after the FM image in (b). The latter reveals fluorescence bleaching covering multiple central microspheres. It is evident from the EM image that the microspheres are in focus, and the probe size is small enough to resolve them. Furthermore, the central dark spot in the EM image provides a measure of hydrocarbon deposition from the stationary electron beam.

Assuming ideal experimental conditions, with a high signal-to-background specimen and a perfect detector, the tight spatial confinement of the scattering electrons would fundamentally limit the attainable (super)-resolution. A quick inspection of electron microscopy textbooks [1] or a basic Monte Carlo simulation (Figure 5.2) indicates that at 1keV energy, the interaction volume is limited to a few tens of nanometers. Thus,

(a) FM image before e-beam exposure   (b) FM image after e-beam exposure   (c) EM image acquired after FM imaging
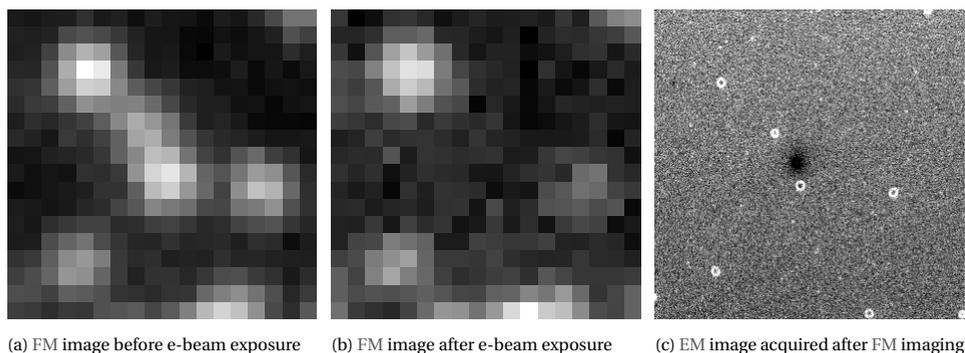
Figure 5.1: **Electron-induced fluorescence bleaching extends hundreds of nanometers from stationary electron beam impingement.** Panels (a) and (b) show FM images acquired before and after a stationary electron beam was parked in the FOV center for 700ms. Panel (c) shows an EM image acquired immediately after FM imaging, confirming that the beam was in focus. The electron beam parameters were 1keV landing energy and 13pA current. The horizontal field width in each image panel is approximately 2μm.

5

primary beam scattering cannot explain the observed bleaching length scale. Additionally, our SEM images do not display charging artifacts, indicating that beam deflection is not the predominant cause.

Describing the electron scattering volume is an extensive subject of study, particularly in lithography, and several Monte Carlo-based simulators provide acceptable results [2] for conducting/semiconducting specimens. Insulators, however, are more challenging to predict, and current research focuses on incorporating charging phenomena into physical simulation descriptors.

Net charge injection, charge carrier separation, trapping, de-trapping, the resultant localized electric fields generated in the material, consequent field-driven transport, and space charge dynamics have all been suggested to play a role in the electron irradiation of insulators [3]–[6]. Interrogating these effects in insulating or weakly conducting media is challenging, and experimental papers in this direction are scarce. To our knowledge, very few papers experimentally investigate charge migration in an insulating material. One study utilized electron beam reflection to examine the radial expansion of space charge in a polymethylmethacrylate (PMMA) film. The results indicated that the space charge region grew to 20μm in size [5]. As eSRM samples are insulating specimens, charge buildup and field-driven migration of charge carriers could contribute to the observed bleaching.

Hence, we aimed to characterize fluorescence bleaching beyond the focused electron beam's classical scattering volume. Our investigation confirms the phenomenon in three insulating systems, utilizing various sample architectures and detection techniques. Further, for a model system with a bulk fluorescent molecule layer, we determine the bleaching extent in relation to the primary electron energy, beam current, applied stage bias, field-free, and immersion lens modes. These experiments rule out potential causes such as charge-related beam defocus, deflection, and secondary electrons emanating from the chamber, thereby qualitatively indicating that the internal migra-
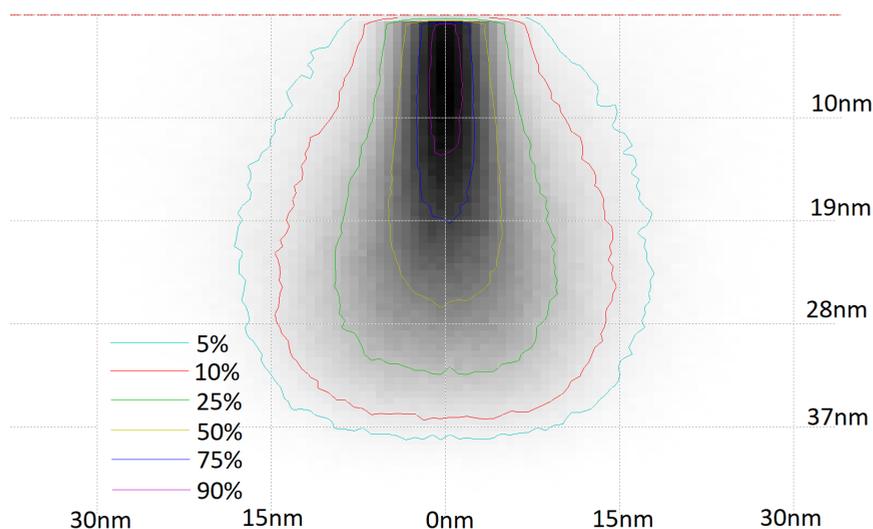
Figure 5.2: **Energy deposition of 10^5 electrons in a Polymethylmethacrylate-ITO-glass substrate (CASINO v2.3 simulation).** See main text for details on individual material thicknesses. The lines depict the distance at which a percentage of the incoming electron energy is deposited. The electrons' penetration depth and transverse spread are ~40nm and ~30nm, respectively. This is considerably smaller than that observed later in Figures 5.3a to 5.3d.

tion of electron beam-generated charge carriers may dictate the observed long-range bleaching. In addition, our results suggest that the sensitivity of molecular fluorescence to electron-induced bleaching can present a unique method to study charge carrier diffusion in weakly conducting materials.

The impact of these findings on the validity of the eSRM technique will be addressed separately in Chapter 6.

5.2. RESULTS AND DISCUSSION

5.2.1. PERYLENE DIIMIDE ON ITO-GLASS

Electron beam-induced fluorescence bleaching is demonstrated by parking a focused electron beam in the fluorescence microscope's FOV. The sample is a bulk layer (440nm) of fluorescent perylene diimide (PDI) molecules [1] on an ITO coated glass coverslip. PDI is a photostable hole acceptor [7] that can form both anions and cations. These ions do not show fluorescence at the same excitation wavelength as the neutral molecule and will, therefore, appear bleached [8], [9]. Figure 5.3a shows an FM of the sample before electron beam exposure. After that, a stationary focused electron beam (1keV landing energy, 13pA beam current) is parked at the FOV center for 60 seconds. FM images are recorded periodically to optically monitor the effects of continuous electron beam irra-

---

[1] Full molecular formula:
N,N'-bis-propyl-1,6,7,12-tetra-(4-tert-butylphenoxy) perylene-3,4:9,10-tetracarboxylic diimide

(a) No e-beam exposure   (b) 5s e-beam exposure   (c) 30s e-beam exposure   (d) 60s e-beam exposure
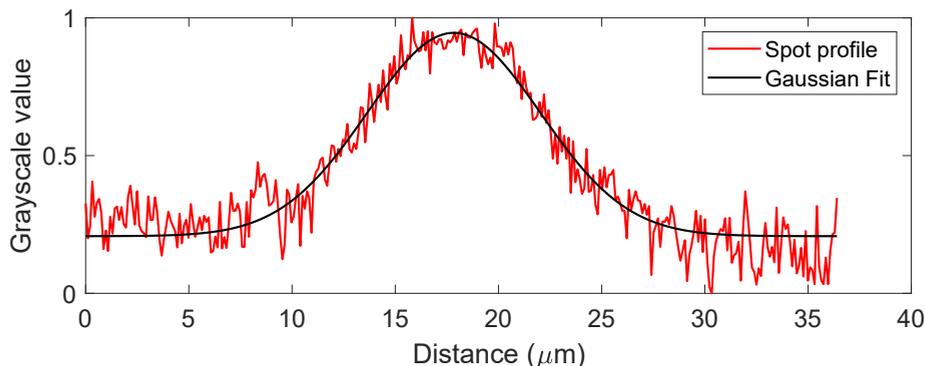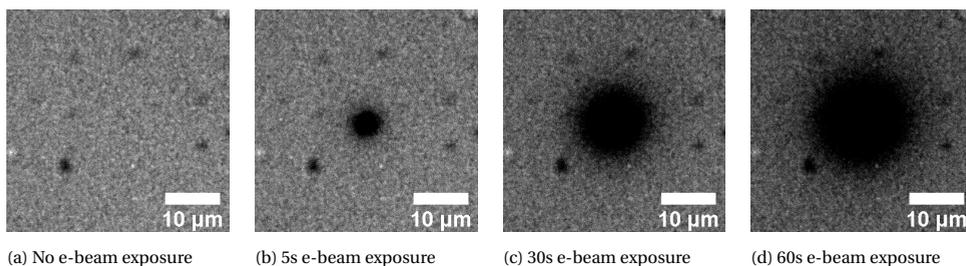
(e) A 1D Gaussian is fit to the contrast inverted spot in panel (c). The calculated standard deviation is 2.6μm.

Figure 5.3: **FM images of electron-induced bleaching in a bulk fluorescent perylene diimide layer in response to increasing electron beam exposure time.** In-situ FM imaging of a stationary focused electron beam on a 440nm layer of perylene diimide molecules on an ITO-glass coverslip. Panel (a) shows an FM image prior to electron beam exposure. Panels (b)-(d) show FM images after 5, 30, and 60 seconds of continuous electron beam exposure.

diation. Figures 5.3b to 5.3d depict the same FOV after 5, 30 & 60 seconds of electron exposure. Here, the central dark region reflects the loss of fluorescence, i.e., bleaching from the electron beam. Interestingly, this bleached region shows a near-symmetric radial growth that reaches a 3σ width (fit to a 1D Gaussian, which we define as the bleaching range) of 5μm at 5s, 12μm at 30s and finally 15μm at 60s of continuous electron exposure.

Electron irradiation can cause molecular rearrangements, structural changes, dissociation, and specimen damage, particularly in organic molecules, such as fluorophores [10]. Fluorescence loss in the electron-exposed area is thus an expected outcome. We used CASINO v2.3, a popular Monte Carlo-based electron scattering simulator, to quantify this bleaching extent for a focused electron beam. CASINO v2.3 is designed to simulate transmitted electrons, electron energy loss, backscattered electrons, and X-rays. We mimicked the perylene experiment shown in Figure 5.3 on account of layer thickness, density, and electron exposure parameters. Polymethylmethacrylate was chosen as a suitable insulator alternative with a density of 1.18g/cm3, close to that of perylene at 1.35g/cm3.

Figure 5.2 depicts electron scattering and the consequent energy deposition profile in the polymethylmethacrylate-ITO-glass system at 1keV landing energy and 10^5 primary electrons, resulting in ~40nm electron penetration depth and ~30nm maximum transverse spread. These results are not corroborated by Figures 5.3b to 5.3d. We recognize that CASINO v2.3 does not incorporate secondary electron scattering or (time-dependent) charging models, which are important for insulators. Traditional Monte Carlo simulators also do not consider electron-electron interaction or the potential for (semi-)permanent material changes from electron impingement, which can affect the scattering trajectories of subsequent incoming electrons. Recent literature reports beam deflection and charge transport in the order of tens to a few hundred nanometers. However, accurate time-dependent charge transport calculations remain prohibitory and are hard to adapt to this system [11].

In order to gain a better understanding of the phenomenon, we carried out independent experiments to assess the bleaching range in relation to the electron landing energy (with a fixed beam current), beam current (with a fixed landing energy), applied deceleration voltage on the specimen stage, and the presence of an immersion magnetic field. We used the sample system and measurement method shown in Figure 5.3 as a basis for these investigations.

INFLUENCE OF ELECTRON LANDING ENERGY

Firstly, we assessed the relationship between the deposited charge and the consequent bleaching range. We investigated this for four different electron energies while maintaining a constant current of 13pA (Figure 5.4). The primary beam scattering extent, governed by the electron landing energy, sets the floor for the expected electron-material interaction space. Based on our CASINO simulations, we considered two energies, 1 and 3keV, which completely encompass the electron scattering volume within the perylene layer. We observed similar behavior for both energies, where the bleaching range increases with the deposited charge.

The total number of electrons accumulated in the sample equals $(1 - \eta_p) \times I \times t$. Here, η_p represents the total electron emission yield, which is the sum of the secondary and backscattered electron yields of the perylene layer. I and t refer to the current and the total irradiation time. Although we do not know the exact electron yield for the perylene layer, we can infer from Figure 5.4 that the difference in η_p between 1 and 3keV is insignificant. As the charge accumulates in the sample, it generates an electric field. A quick explanation for the expanding bleaching spot could be an electric-field-induced deflection, or a primary beam defocus. It is worth noting that the bleached spot increases almost symmetrically, which makes beam deflection highly unlikely. Additionally, while we observed this long-range bleaching in eSRM experiments, we did not see any indication of charging artifacts in either the SEM or eSRM images (see the SEM image in Figure 5.1c).

We repeated the experiment for higher electron energies, namely 5 and 15keV (also shown in Figure 5.4) where the electron beam penetrates the perylene layer, crosses the thin ITO coating underneath, and hits the underlying glass substrate (see Figure 5.15 for a focused ion beam cross-section image of the sample). Glass shows strong cathodo-
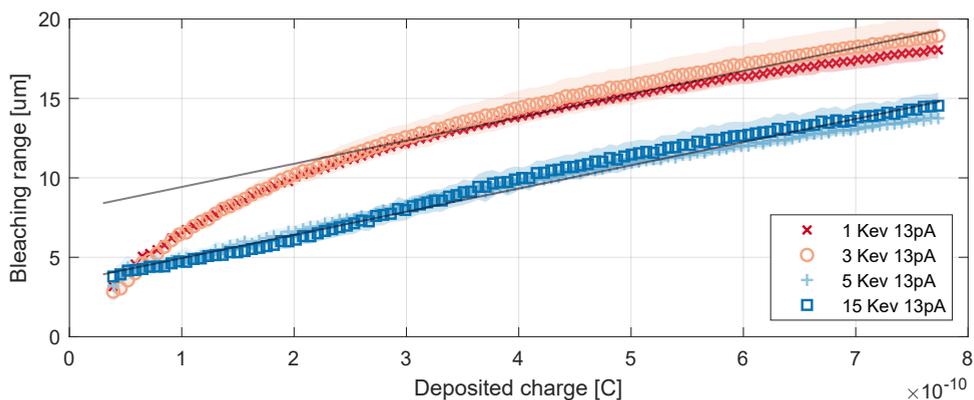
Figure 5.4: **Bleaching range as a function of deposited charge for different electron landing energies.** The bleaching range increases with the deposited charge. There is a clear distinction in energy levels between where the beam penetrates the perylene layer (5 and 15keV) to reach the conductive ITO coating and where it stops earlier (1 and 3keV). The two parallel straight lines are provided as guides to assist the eye.
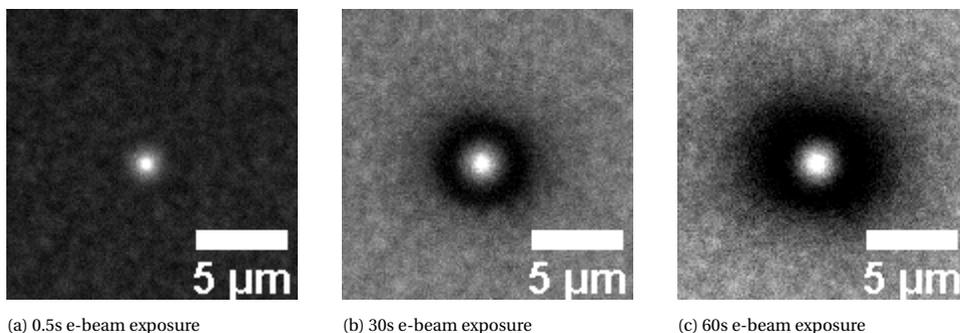

(a) 0.5s e-beam exposure   (b) 30s e-beam exposure   (c) 60s e-beam exposure

Figure 5.5: **FM images of electron-induced bleaching in a bulk fluorescent perylene diimide layer, showing a bright central CL spot.** Electron beam parameters are 15keV landing energy and 13pA current. Note that the CL spot is much smaller than the bleached region, indicating that the bleaching is not caused by charge-induced beam defocus. The contrast is adjusted to reduce CL signal clipping.

luminescence (CL), meaning it emits visible light upon electron irradiation. Indeed, at 15keV, a bright luminescent spot appears in the center of the fluorescence FOV (shown in Figure 5.5) and the bleached spot. The CL spot size gives a measure of the electron scattering volume convoluted with the point spread function of the fluorescence microscope. The observed CL spot is smaller than the bleached region, excluding beam defocus as a root cause. Furthermore, no beam drift was observed in the time series.

For both 5 and 15keV landing energies, Figure 5.4 shows that the bleaching range expands with deposited charge. However, the spatial extent is reduced compared to 1 and 3keV. This case allows most electrons to reach the ITO and glass substrate, as only a fraction are stopped by the perylene layer. Figure 5.6 depicts the normalized fraction of primary electrons that reach a maximum penetration depth at 4 and 5keV landing energies. At 4keV, the primary electrons begin to reach the ITO layer. At 5keV, a notice-

able peak forms in the ITO layer, stopping the majority of primary electrons. This can be attributed to ITO's significantly higher material density than perylene and glass.

The number of electrons injected in the perylene layer per unit time can be expressed as $(\chi - \eta_p) \times I + \beta_s \times (1-\chi) \times I + \delta_s \times \chi \times (1-\chi) \times I - \delta_s \times \eta_p \times (1-\chi) \times I$, where χ is the fraction of electrons stopped in the 440 nm perylene film, β_s is the substrate secondary electron yield, and δ_s the substrate backscattered electron yield (thus $\eta_s = \delta_s + \beta_s$). The equation's first term represents the difference between the number of primary electrons absorbed and the number of emitted electrons. The second term accounts for the secondary electrons from the substrate, which are deposited in the perylene. The third term refers to backscattered electrons from the substrate that are also deposited in the perylene. The fourth term represents the electron emission, which is, in turn, caused by the backscattered electrons from the substrate. Note that this first-order approximation assumes backscattered electrons have roughly the same energy as the primary electrons. For higher energies, χ and η_p will become negligible. The charge build-up in the perylene layer will be dominated by β_s, the secondary electron yield of the substrate, which shows limited variation with increasing energies [1]. This is consistent with the 5 and 15keV profiles in Figure 5.4, which show significant overlap.
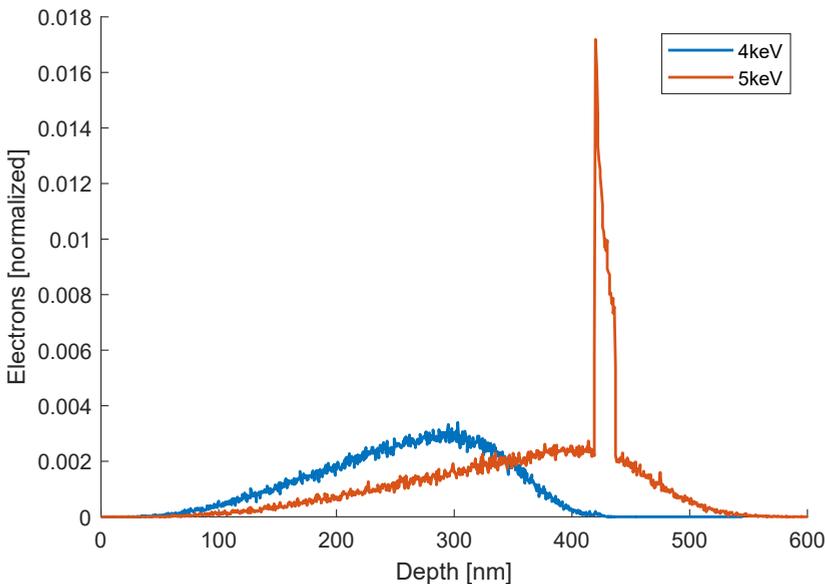

Figure 5.6: **Normalized histogram depicting the maximum penetration depth of primary electrons at 4 and 5keV landing energy, using CASINO v2.3.** Our sample scheme served as the input to the simulation with a 440nm layer of fluorescent perylene diimide on a 10nm ITO-coated glass substrate. The graphs depict the maximum depth traveled by an incoming electron at 4 or 5keV before it loses enough energy to halt in the material. At 4keV, the electrons stop in the perylene layer, while at 5keV landing energy, most scatter in the ITO layer. This is evident from the peak at 450nm due to the higher ITO density compared to that of perylene.

INFLUENCE OF BEAM CURRENT & SPOT SIZE

Next, we investigated the bleaching range at different electron currents and imaging modes, immersion and field-free. The reason for doing so is two-fold. First, we have observed that the bleaching range depends on the total charge injected into the system (Figure 5.4). However, we still need to investigate whether the rate at which this charge is injected, i.e., the current of the incoming electron beam, also impacts the bleaching range. A caveat here is that the electron probe size, i.e., the area irradiated by the beam and, thus, the size of the electron scattering volume, is not affected by the current. Second, one could argue that the bleaching range could be caused by a 'shower' of secondary electrons consisting of so-called SE3s, secondaries generated in the vacuum chamber by backscattered electrons, and potentially secondaries attracted back to the substrate due to the field created on the sample. If these effects exist, they may occur in field-free mode but not in magnetic or electrostatic immersion modes. The latter would particularly accelerate all secondaries away from the sample and into the column. [12].

Figure 5.7 shows the bleaching range for 1keV landing energy for 12, 200, and 800pA currents in field-free and magnetic immersion lens modes. The results from the immersion mode indicate that the bleaching range is not associated with a secondary electron shower. Furthermore, all three currents in the immersion mode show an increasing bleaching range with the total deposited charge without any current dependence. The field-free mode yields similar results for 200 and 800pA, except for 13pA.
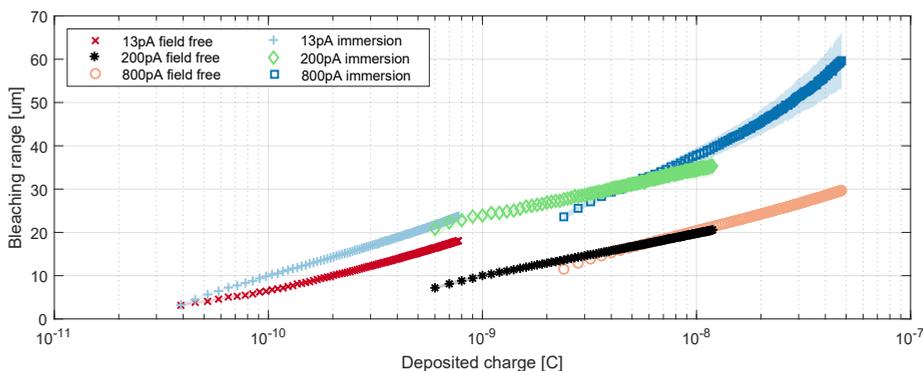

Figure 5.7: **Bleaching range as a function of deposited charge for field-free and immersion SEM lens modes for 13, 200, and 800pA currents.** For the immersion mode, all data points lie approximately on one line, whereas the field-free mode shows a difference between the low (13pA) and high currents (200 and 800pA).

We reasoned that the discrepancy in the field-free mode results could be due to variations in the electron beam spot size between both modes and different currents. At 1keV landing energy, the spot size is dominated by chromatic and spherical aberrations. The current increases as the beam opening angle increases, increasing both aberration coefficients. We quantify this effect by measuring a standard tin-ball sample's 35-65 resolution at 1keV (Figure 5.8). The immersion lens mode (also called in-lens or ultra-high resolution mode) reduces the chromatic and spherical aberrations at lower landing energies by immersing the specimen surface in the probe-forming magnetic field [1], [13].

Figure 5.8 confirms the smaller spot size in immersion mode. In immersion mode, the electron beam resolution remains relatively constant with beam current. This corresponds with the observation that the bleaching range follows the same trend for different currents. However, the resolution decreases much more with increasing current for the field-free mode. Relating Figure 5.8 to Figure 5.7 supports the finding that a smaller spot size results in a larger bleaching range. It is worth noting that the bleaching effect in immersion mode is larger for the same amount of deposited charge. We speculate that this effect may be due to the highly localized field within a smaller spot size. Electrons created in the scattering volume in immersion mode will feel a stronger field and, thus, stronger force than electrons at the same position in a situation where the scattering volume is larger (i.e., field-free). Thus, only a fraction of the charge contributes to the force the electron experiences. This initially larger electron acceleration may drive the bleaching range further for smaller spot sizes. In addition, for the measured currents, the bleaching range remains current/dose-rate independent for comparable spot sizes. This remains true for the field-free spot sizes at 200 and 800pA. Therefore, it also appears that beyond a certain maximum spot size (here at 15nm), the impact on the bleaching range is limited.
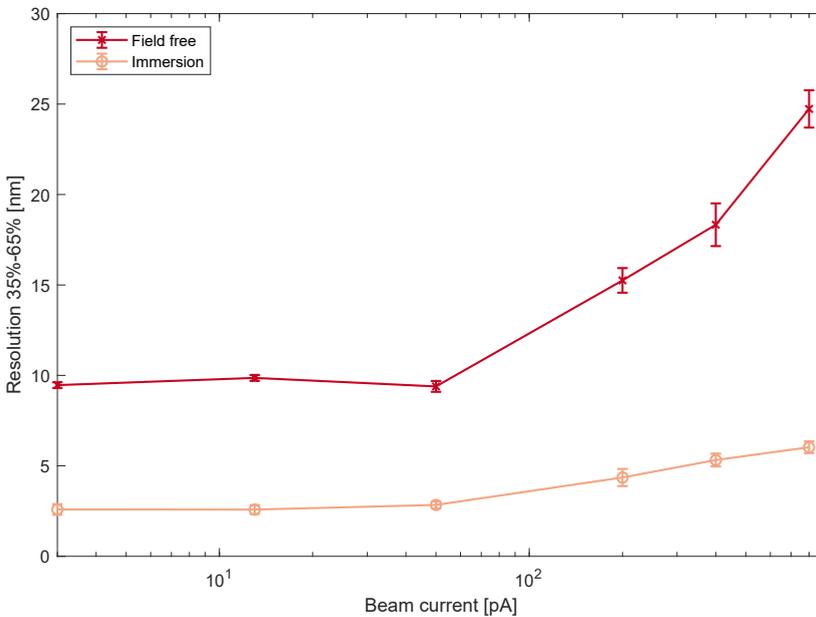
5

Figure 5.8: **Measured 35-65 electron beam resolution as a function of beam current for field-free and immersion SEM lens modes.** Immersion mode results in smaller spot sizes, which remain relatively constant with increasing current. The spot size in the field-free mode increases significantly with higher currents, 4x larger at below 50pA and up to 10x larger at 800pA.

INFLUENCE OF BEAM DECELERATION

The results from the immersion mode experiments (shown in Figure 5.7) indicated that SE3 exposure is not the cause of the observed bleaching. However, electrostatic immersion or beam deceleration can provide conclusive evidence. Decelerating the incoming electron beam using a negative specimen potential is an established method for low keV applications, especially in life sciences SEM. Low keV imaging (1-5keV) is ideal for thin, sensitive, and insulating samples as it reduces charging and optimizes the scattering volume to match the sample's thickness. By introducing beam deceleration, the probe-forming high-energy beam can be slowed down only when it reaches the sample. This helps to maintain the small spot size. Additionally, the scattered electrons leaving the sample can be accelerated toward electron detectors located close to the electron-optical axis (such as under the objective lens or in the electron column). The latter improves signal collection efficiency, which is particularly useful for weakly stained EM samples [12].

To investigate the effect of stage bias on the bleaching range, a -500V potential was applied to the perylene sample stage. The primary energy was set to 1.5keV, resulting in an effective landing energy of 1keV at the specimen surface. This decelerating field then serves to block all secondary electrons arising from the chamber, thus excluding SE3s as a causative mechanism. Figure 5.9 plots the bleaching range as a function of deposited charge for 13 and 200pA currents, with and without a -500 V bias. Figure 5.9 shows that the bleaching range is not influenced by stage bias. Minor variations are contained within the noise limits of the respective measurements. The bleaching range thus seems mediated by interactions in the specimen bulk.
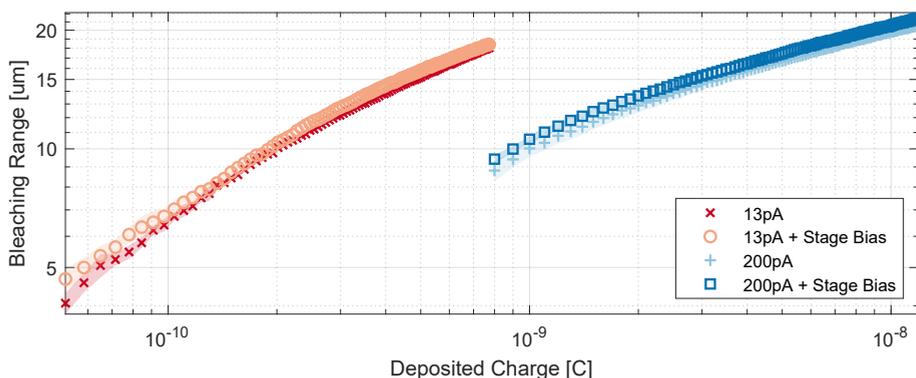

Figure 5.9: **Bleaching range as a function of deposited charge shows that the former is independent of an applied -500V stage bias.** The graphs represent 13pA and 200 pA currents for a system with and without a -500V stage bias. The effective landing energy was maintained at 1keV in both cases.

5.2.2. BLEACHING RANGE IN OTHER MEDIA

We broadened our inquiry to incorporate other insulating agents, such as a metal-coated plastic scintillator (which serves to exclude beam deflection or defocus), perylene on aluminum oxide-coated ITO-glass (to examine the influence of a strong insulator atop

the ITO layer) and finally, polystyrene microspheres (which allowed us to measure at a lower magnitude of deposited charge).

PLASTIC SCINTILLATOR

Perylene diimide molecules are commonly used as fluorescent probes. Here, we used their electron-irradiation sensitivity to track charging behavior by means of a loss in fluorescing ability (i.e., bleaching). The fact that they are insulating materials could, however, influence the electron beam (via beam deflection and defocus). Coating such samples with a conductive coating without influencing their fluorescent properties is challenging. We hypothesized that plastic scintillators could serve as a suitable medium for investigation as they are easy to coat with a conductive layer. They consist of a primary fluorescent emitter, a fluor, embedded in a polymer matrix and are routinely used as high-energy radiation detectors. Yet, their relatively low radiation resistance is disadvantageous for sustained usage. Fluors lose their scintillation ability with prolonged irradiation in a manner qualitatively similar to the fluorophore bleaching outlined above. We, therefore, set out to examine the bleaching phenomenon in a bulk (approximately 100nm thick) plastic scintillator spin-coated on an ITO-glass coverslip. The polymer base of the scintillator (polyvinyl toluene) is non-conductive and was sputter coated with a 10nm Boron layer to enable electron imaging. The latter is key to this method as the electron beam is used to measure the bleaching range rather than fluorescence. The proposed architecture thus consists of a thin conductive layer, which is followed by a bulk insulator.

Figure 5.10 shows a transmission electron image (via a multi-pixel photon counter) of the electron-irradiated scintillator. Dark spots mark scintillator bleaching from a stationary focused electron beam at 5keV landing energy. Rows 1-6 show the effect of increasing electrons injected by higher electron exposure times. Columns 1-7 show repeated exposures at the same exposure time for statistical relevance. Spots in row 6 (final row) are at a total dose of 1×10^{-11}C. Figure 5.11 shows the width of the bleached spots as a function of charge for energies 2, 3, 5, and 7keV.
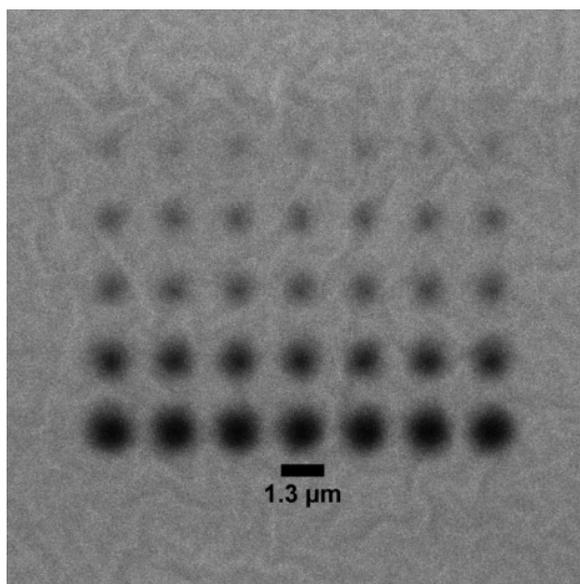
Figure 5.10: **Transmission electron imaging of an electron irradiated plastic scintillator layer. Cathodoluminescence generated therein is detected using a multi-pixel photon counter.** The rows show increasing deposited charge, and the columns depict repeated irradiation measurements for statistical significance. The sample was exposed at 5keV landing energy and 100pA current. The irradiation times increase from 500µs (row 1) to 10s (row 5).

It is visually evident from Figure 5.10 that the bleaching range increases with deposited charge. Figure 5.11 quantifies the observation. For 2, 3, and 5keV, the bleaching range increases with energy. However, at 7keV, there is a reduction similar to that observed in the perylene system. While we did not measure the scintillator thickness via focused ion beam milling as we did for perylene, we attribute it to the electron penetration depth exceeding the specimen thickness and the primary electrons reaching the ITO layer. We recognize that having a (minimally) conductive Boron layer on top of the insulating scintillator may provide a faster channel to the ground relative to the ITO. Thereby reducing the local charging impact, especially at lower landing energies. This may reflect a reduction in the bleaching range and its rate of development. However, the trends (i.e., dependence on energy and dose) were expected to be preserved. A key advantage of this method is the direct visualization of irradiation-induced specimen modification as the electron beam is used to both cause and measure the bleaching extent, now at electron beam resolution.

Furthermore, we note that the measured bleaching widths may be lower than in reality because the final electron imaging may further bleach the whole sample region. The combination of the relatively low signal-to-noise ratio and the conductive layer on the sample surface makes this mainly an illustrative measurement.
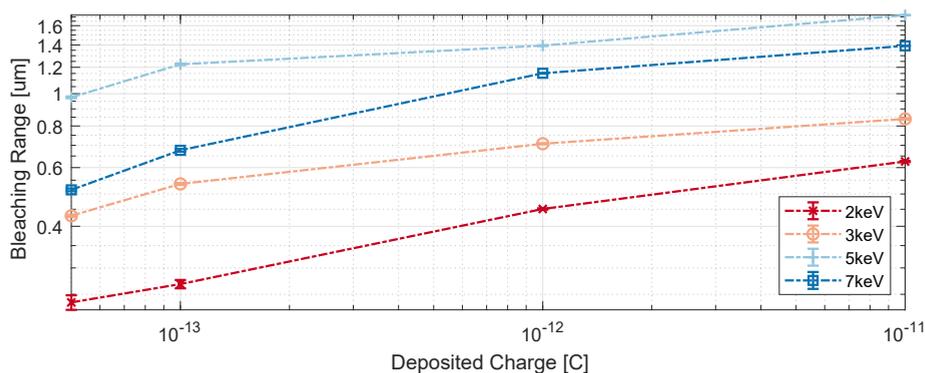
Figure 5.11: **Bleaching range as a function of deposited charge for a plastic scintillator.** Row 1 as seen in Figure 5.10 is not depicted due to a low signal-to-background ratio.

PERYLENE ON ALUMINIUM OXIDE-COATED ITO-GLASS

We next investigated the bleaching impact of a more robust insulator in the direct vicinity of the fluorescent sample. To that end, a 10nm aluminum oxide layer was deposited via atomic layer deposition on an ITO-coated glass coverslip. Following this, fluorescent perylene was spin-coated to form a bulk layer. A 1keV focused electron beam (field-free mode) was parked in the sample FOV using the same experimental protocol as the earlier perylene system. The resultant bleaching effects were similarly monitored. We reasoned that a potent insulator above the conductive ITO layer should influence the bleaching range by exacerbating charging. Results in Figure 5.12 indicate that it is indeed the case. A similar dependence was observed between the bleaching range and deposited charge. However, the bleaching range is now an order of magnitude larger than in the absence of insulating aluminum oxide in Figure 5.7. The effect is that the electrons now appear to be driven outwards, bleaching further away. For similar deposited charges, we also noticed visual charging effects (i.e., streaking) that are the more commonly recognized symptoms.

POLYSTYRENE MICROSPHERES

Fluorescent polystyrene microspheres are discrete insulating emitters. They are highly fluorescent and provide clear electron contrast, making them ideal for use in an integrated light-electron microscope. Using fluorescent microspheres to study the bleaching range has a few advantages. Firstly, the microspheres can be deposited sparsely on the ITO-glass surface, allowing each microsphere to act as an individual reporter for fluorescence bleaching while still maintaining enough density to populate the FOV. Secondly, minor decay in fluorescence can be easily detected from a bright point emitter compared to a bulk fluorescent layer. Lastly, the microspheres have electron contrast, allowing for precise distance measurements from the focused electron beam. Together, this offers higher detection sensitivity and the opportunity to measure at lower deposited charges.

For the measurements in Figure 5.14, we employed 50nm diameter polystyrene microspheres that were spin-coated on an ITO-glass coverslip. The microspheres were
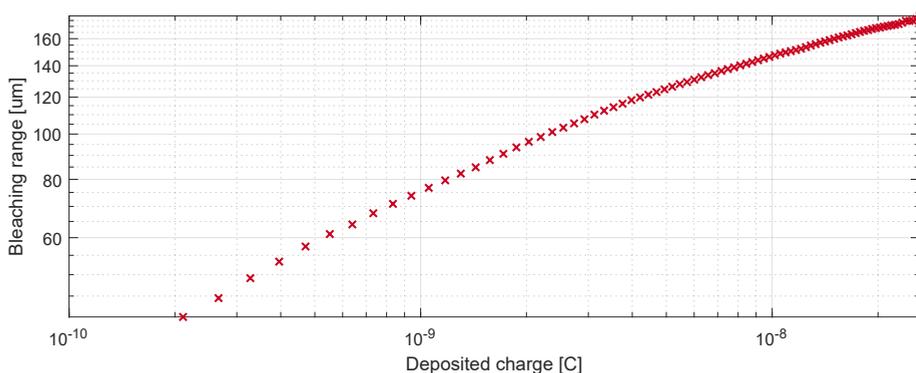
Figure 5.12: **Bleaching range increases ten-fold in the presence of aluminum oxide.** 1keV focused electron-beam irradiation of bulk perylene spin-coated on a 10nm aluminum oxide layer on ITO-coated glass. The bleaching range is depicted as a function of deposited charge for a 13pA current. Strong insulating properties of aluminium oxide result in a ten-fold increase in bleaching range for similar deposited charges as seen in Figure 5.7. The key difference is that an electrical insulator is now placed between the fluorescent layer and the conductive ITO.

5

sparsely distributed such that individual emitters could be optically identified. A focused, stationary electron beam at 1keV landing energy and 13pA current was parked at the optical FOV center for a predetermined dwell time. Fluorescence images of the sample FOV were taken before and after electron beam irradiation. Each microsphere therein reported the influence of the deposited charge at a particular distance away from initial deposition by means of fluorescence bleaching. The precise distances were calculated from a subsequent SEM image. The measurements were repeated for increasing dwell times, each time using an unexposed sample region. An example image sequence at 10s dwell time is shown in Figure 5.13.

Results in Figure 5.14 note that the deposited charge is two orders of magnitude lower than in the perylene system. The distances show similar magnitude (16μm at 10^{-10}C) as Figure 5.4. However, both systems differ in sample architecture. In the perylene system, a bulk insulator (440nm) was followed by a thin (10nm) conductive ITO on a glass substrate. At 1keV, the majority of scattering events thus occur in the fluorescent specimen. Alternatively, the microspheres formed a discrete fluorescing scheme on the ITO-glass substrate. In practice, the incident electron beam thus directly scatters in the glass (although there is a thin, optically visible residue surrounding the microspheres, likely from the surfactant in the spin-coated solution). Intuitively, the conductive layer must influence charge build-up and transport. An expected outcome is that the microspheres may report a smaller bleaching range at a similar deposited charge compared to perylene. However, decays in perylene are detected through an underlying brightly fluorescent bulk. Signal detection efficiency is lowered; thus, the tails of the bleached zone could be underestimated. Besides obvious material and specimen configuration differences, the resolution of the detection method also influences the bleaching range. Yet, the consistent trends in bleaching development across systems are remarkable and point to an underlying phenomenon that may be persistent in fluorescent insulators.
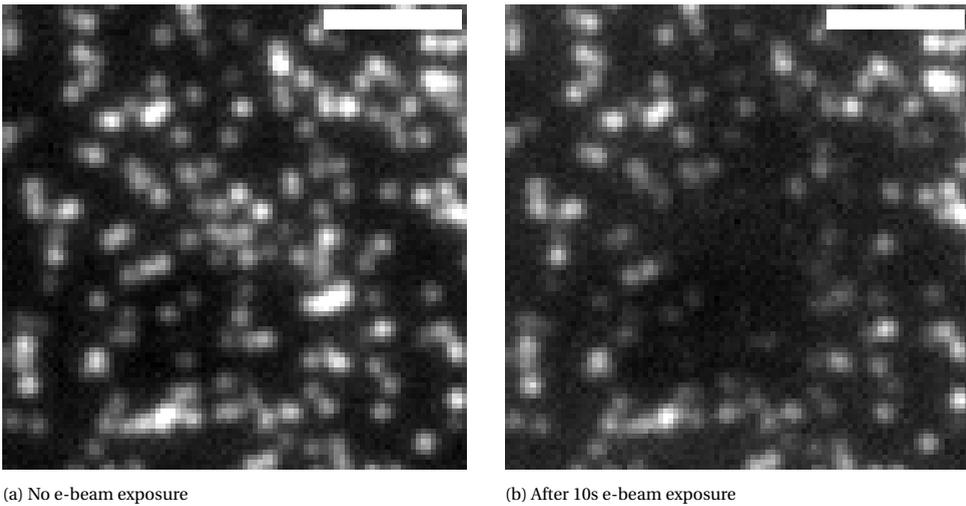
(a) No e-beam exposure   (b) After 10s e-beam exposure

Figure 5.13: **FM images of polystyrene microspheres, (a) before and (b) after 10s irradiation with a 1keV landing energy and 13pA current electron beam.** Scalebar 3 μm.
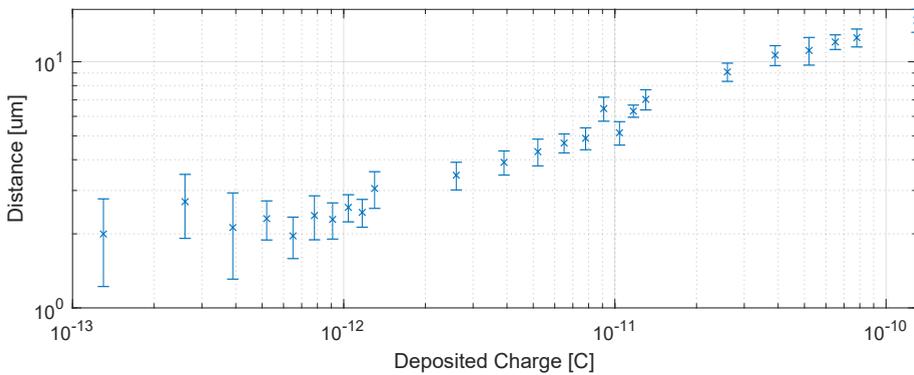

Figure 5.14: **Bleaching range as a function of deposited charge measured in a sample of fluorescent polystyrene microspheres spin-coated on an ITO-glass coverslip**. The electron beam parameters were set at 1keV landing energy and 13pA current.

5.2.3. RELATION TO LITERATURE

To our knowledge, the experimental use of fluorescence as a spatiotemporal indicator for electron behavior in insulators has not been previously reported. Understandably, it requires an integrated light-electron microscope, the possibility for simultaneous light-optical imaging, and a fluorescent sample that survives in a vacuum. All of the above are relatively modern findings that have mostly seen application in biology. However, it has long been established that irradiation of insulators with a non-penetrating electron beam results in the development of space charge.

Work that is closest 'in principle' to this manuscript involves measuring space charge

growth in polymethylmethacrylate via a reflection method (called the mirror image method). Over the course of four papers [3]–[6], the authors discuss charge trapping and its radial migration distance in bulk polymethylmethacrylate. Particularly in Gong, Song, and Ong [5], space charge dynamics is studied, which looks at the evolution of space charge range as a function of irradiation time. The goal is similar to the bleaching range experiments discussed thus far; to study the evolution of the bleaching range as a function of irradiation time or deposited charge.

Their experiment used bulk polymethylmethacrylate placed over a conductor connected to the ground through a pico ammeter. They determined the amount of trapped charge by measuring the difference in the current flowing in and out of the system. The radial space charge extent was measured using the mirror image method. Here, polymethylmethacrylate was charged using a focused stationary electron beam at a fixed landing energy (5, 10 & 15 keV) and beam current (10pA) for a set duration (in seconds). It is thereafter imaged using a 1keV electron beam. The accumulated surface charge creates an equipotential surface reflecting the imaging electron beam. The radius of this reflection zone can be measured and refers to the space charge range. Their results indicate that space charge distribution grows with irradiation time, with a steep increase in the initial 20 seconds, and eventually attains saturation. The range also increases with increasing landing energy. At 5 keV irradiation, they found that the radial distribution of the trapped charge saturates at 20 μm for a deposited charge of 2×10^{-10}C. Our measurements show similar length scales but do not show saturation. We observe that the experimental methods employed differ significantly from one another. Nevertheless, some observations can still be made. The mirror image method is a less sensitive technique than fluorescence, as only the surface spread can be measured. The bulk charge distribution can also be expected to be larger at high landing energies. Also, the edge of the reflected zone is defined by the local potential dropping below a threshold value, which cannot reflect the imaging beam. This will result in a hard cut-off region where the electrons can enter the material again. We emphasize that the exact causative agent for fluorophore bleaching, as seen above, is not understood and is beyond the scope of this work. However, the correlation between the two studies may offer insights to further investigate if space charge transport can be monitored using fluorescence.

5.3. Conclusion

We have reported electron-beam-induced fluorescence bleaching occurring several micrometers away from irradiation incidence. We hypothesize that this phenomenon is caused by the diffusion of charge carriers generated by the electron beam, driven by an electric field that develops in the material under electron beam irradiation. We have systematically analyzed the spatial extent of this bleaching as a function of deposited charge for varying currents, landing energies, applied stage bias, and beam spot size in a perylene-ITO-glass model system. We further extended our study to three other sample schemes using varied detection methods to a) better understand the phenomenon and b) rule out potential alternative explanations.

From the primary perylene-ITO-glass system, we demonstrate that the bleaching

range increases with the amount of charge deposited in the material. It increases with interaction volume, i.e., landing energy only when all deposited charge is contained in the fluorescent specimen thickness. The bleaching range will be smaller and less energy-dependent for landing energies where most of the charge is deposited outside the fluorescent specimen (ITO or glass). Further, the bleaching range is current-independent for the measured currents of 13 to 800pA. This may have a lower limit at sufficiently low currents as the sample may have time to recover between arriving electrons (i.e., the local charging may dissipate). Nevertheless, minor slope changes (i.e., the rate of increasing bleaching) can be seen at varied currents, indicating that current could be influential, even if not the dominant mechanism. The electron beam spot size influences the bleaching range. Decreasing spot size increases the bleaching range, particularly when switching from field-free to immersion mode. Lower currents in field-free mode, having (comparatively) smaller spot sizes due to fewer aberrations, show a larger bleaching range. However, beyond 15nm, increasing spot sizes do not appear to significantly impact the bleaching range. Applying a -500 V stage bias does not affect the bleaching range. Therefore, we can conclude that the bleaching range is not mainly influenced by secondary electrons originating from the chamber (which are excited by primary backscattered electrons, i.e., SE3s). Beam deflection and charging-related primary beam defocus have also been ruled out as causative agents.

Our findings indicate that in addition to the perylene system, plastic scintillators and polystyrene microspheres experience spatially expanding bleaching of a similar magnitude. In the scintillator case, this occurs even when a conductive layer is present on top, suggesting that bleaching may be predominantly driven by charging inside the insulator bulk. With these findings, we propose that our approach of using fluorescence to visualize charge dynamics inside insulators could present a new real-time experimental technique with high spatial resolution to study insulators under electron beam irradiation.

5.4. EXPERIMENTAL DETAILS

SAMPLE PREPARATION

PERYLENE DIIMIDE ON ITO-GLASS:

10µL of 60µM tetraphenoxy-perylene diimide (PDI) in toluene solution was diluted in 990µL of toluene. 200µL of the resultant 0.6µM solution was spin-coated on ITO-coated glass coverslips (no.1 thickness, Materion Balzers Optics) at 500rpm for 5 seconds and after that at 2000rpm for 60 seconds. Perylene molecules aggregate into large clusters with time, disrupting a uniform fluorescent layer. To circumvent this effect, samples were freshly prepared on the day of experimentation. PDI has a fluorescent spectrum with excitation and emission centered around 435 and 467 nm, respectively [14]. Thus, the sample architecture was a weakly conducting polymer placed on a ~10 nm conductive layer of ITO over a glass substrate (0.17mm). A focused ion beam cross-section can be seen in Figure 5.15.

The ITO layer was grounded to the central microscope ground via an aluminum sam-

ple carrier ring. The rationale behind such construction was to allow charge-buildup and transport through the 3D volume of the fluorescent molecules to reach the conducting layer and be channeled to the ground. Any volumetric fluorescence loss/bleaching due to electron irradiation could now be measured in both space and time with a diffraction-limited spatial resolution. All measurements were performed in an integrated fluorescence – scanning electron microscope (Delmic SECOM - Thermo Scientific Verios). Such an integrated system allowed registering in-situ modification of fluorescence via electron impingement.
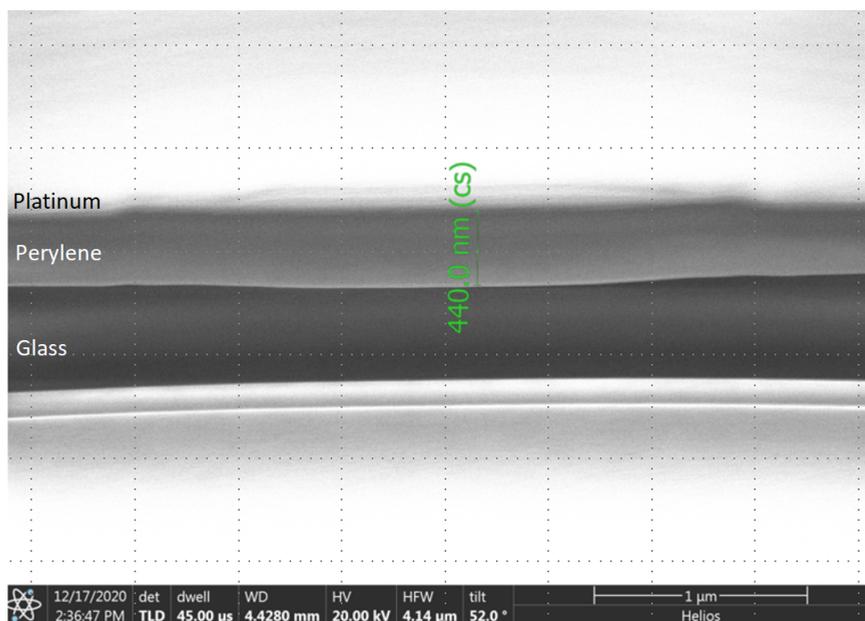
Figure 5.15: **SEM image showing a cross-section of the perylene diimide-ITO-glass sample obtained via focused ion beam milling.** The annotation shows the layer thickness (440nm) measured after focused ion beam milling. Directly below this layer is a ~10nm ITO layer (visible as a light-colored line in the SEM image) over a glass substrate. Platinum electron beam deposition was used to avoid charging.

BORON-COATED PLASTIC SCINTILLATOR ON ITO-GLASS

ITO-coated glass coverslips were spin-coated at 2000 rpm with a thin layer of EJ-296 scintillator paint (Eljen Technology) with a scintillation peak wavelength at 435 nm and a 1/e decay time of 2.5 ns. The layer was estimated to be a few 100nm thick, which was sufficient to stop electrons from reaching the ITO coating of the coverslip. The polymer base of the paint (polyvinyl toluene) was not conductive and, therefore, sputter-coated with a ~5 nm conductive Boron layer. Boron was chosen because of its low atomic number and density, giving it relatively low scattering cross sections where most electrons will reach the paint without being slowed down in the conductive coating layer.

POLYSTYRENE MICROSPHERES ON ITO-GLASS

10μL of a fluorescent polystyrene microspheres stock solution (Dragon Green, Bangs Laboratories, Inc.) was diluted with 300μL deionized water. 25μL of the resultant was spin-coated on ITO-coated glass coverslips (no.1 thickness, Materion Balzers Optics) at 3000rpm for 120 seconds. This protocol achieved sparse, evenly distributed single microsphere emitters that served as discrete nano-probes for the local charge presence.

ELECTRON IRRADIATION & IMAGE ACQUISITION

Electron irradiation and subsequent imaging (via either fluorescence or transmission electron contrast) were performed in an integrated FM-SEM setup (Thermo Scientific Verios + Delmic B.V. SECOM). All measurements have the sample grounded, except the beam deceleration experiments where a -500 V potential was externally applied to the stage. The chamber was pumped to standard SEM pressures at $\sim 10^{-6}$ mbar. The FM and EM coordinate systems were aligned via cathodoluminescence markers, following a protocol similar to [15]. For transmission electron detection in the SECOM platform, the excitation path was removed, and the system was only used for collecting scintillator-generated photons using a 0.95 NA air objective focused on a Hamamatsu multi-pixel photon counter (s13360-3050sc). The detector signal was fed directly into the SEM's external detector input. The electron beam working distance for all measurements was ~5.7 mm.

PERYLENE DIIMIDE ON ITO-GLASS

For each experiment, an unexposed fluorescent FOV was subjected to stationary focused electron beam irradiation for 60 seconds. An sCMOS detector (Andor Xyla 4.0) was used to simultaneously record FM images (excitation 505 nm; emission multi-band filters FF01-432/515/595/730-25, Semrock) with a 500ms exposure time (therein the temporal resolution of this set of experiments). The detector was triggered to begin acquisition in sync with the electron beam unblanking and to grab 5 FM frames before electron exposure. The image's pixel size was 108nm, which limits the minimum measurable bleaching range to around 300nm. We thereby investigated the spatial bleaching range as a function of electron beam parameters, namely the landing energy, current, beam deceleration, and presence of an immersion lens.

POLYSTYRENE MICROSPHERES ON ITO-GLASS

The electron beam was focused in spot mode at a fixed landing energy and current of 1keV and 13pA, respectively, in the center of an unexposed sample FOV. The effective electron fluence was varied by changing the dwell time between 300 μs and 10 seconds. For each fluence, two fluorescence images (exposure time 2 seconds) and one electron image (secondary electron contrast; dwell time 100 μs) were recorded, i.e., an FM image before and after electron irradiation, followed by a final SEM image using the through-lens detector. The rationale for 3 image acquisitions was as follows: the fluorescent polystyrene microspheres have both fluorescence and electron contrast. The FM images with sparse emitters were sufficient to report individual intensity differences. The

final SEM image allowed accurate determination of distances (compared to the optical diffraction-limited FM image) from the electron beam irradiation spot, to which the intensity differences could be attributed.

Boron-coated Plastic Scintillator on ITO-glass

A boron-coated plastic scintillator was exposed to a focused electron beam (in spot mode). For a given landing energy and beam current, the exposed FOV (horizontal field width 15μm) consisted of 5 rows and 7 columns of irradiated spots. The electron beam was steered to the location coordinates via a VI script and blanked otherwise. Each row corresponds to increasing electron fluence (from top to bottom), whereas the columns represent repeated exposures for averaging purposes. After exposure, an SEM image was acquired at 500ns dwell time using the external multi-pixel photon counter detector at the respective exposure landing energy. The low dwell time was chosen to reduce additional electron exposure at the expense of lowered signal-to-noise ratio. The impact of four landing energies (2,3,5 & 7keV) was assessed this way.

Image Analysis

Perylene Diimide on ITO-glass

Images were analyzed using Python 3. For each dataset consisting of consecutive camera frames, a reference frame before electron beam exposure was subtracted, and the image intensity was normalized by this reference frame. We cropped camera images to 500x500 pixels to exclude unaffected areas. Next, the image series was summed across the horizontal axis to create a one-dimensional dataset. We then fitted a 1D Gaussian to this dataset. In some cases, when the bleaching range and loss in fluorescence were still small at low electron doses, we found that the cropping to an area of 500×500 pixels was too large, causing the loss in fluorescence to be drowned in background fluctuations. In those cases, we cropped the first few frames to a smaller area of 90×90 pixels.

Polystyrene Microspheres on ITO-glass

The SEM image was used to find the center and radii of the polystyrene microspheres. For feature extraction, the image was subjected to a series of image processing steps: contrast enhancement, binarization, thresholding, salt and pepper noise removal, and finally, a circle Hough transform. The distance of each microsphere (with respect to its center) from the electron beam irradiation spot was determined. Similarly, the centers of the microspheres were identified in the FM image via 2D Gaussian fitting. The FM and EM coordinates were linked through a linear transformation matrix. A 5x5 pixel analysis window was applied over each microsphere feature to allow for nonlinear distortions that the previous linear transformation matrix could not correct. This ensured that the entire microsphere was within the analysis window. Feature intensities within the analysis window were measured for both FM images (before and after electron-beam exposure) after background subtraction. The difference in measured FM intensity was attributed to the respective microsphere, which in turn reports on electron beam exposure at the associated distance from the irradiation spot. While the centers and radii

of connected microspheres were individually identified, their intensity differences could not be separated within the analysis window. This resulted in repetitive values. However, only a few such occurrences were present.

BORON COATED SCINTILLATOR ON ITO GLASS

SEM images were analyzed for each row of irradiated spots, which denoted a fixed electron fluence and 7 repetitive instances. Image intensities were summed to generate a profile from which the width of the spots was extracted following background subtraction and smoothening. The resultant values were averaged over the number of instances. The spot size was found by fitting a 1D Gaussian.

5

BIBLIOGRAPHY

[1] L. Reimer and S. E. Microscopy, "Physics of image formation and microanalysis", *Springer*, vol. 45, p. 135, 1985.

[2] K. T. Arat, A. C. Zonnevylle, W. S. Ketelaars, N. Belic, U. Hofmann, and C. W. Hagen, "Electron beam lithography on curved or tilted surfaces: Simulations and experiments", *Journal of Vacuum Science & Technology B*, vol. 37, no. 5, 2019.

[3] H. Chen, H. Gong, and C. Ong, "The charging behaviour and internal electric field of pmma irradiated by a kiloelectronvolt electron beam", *Journal of Physics: Condensed Matter*, vol. 7, no. 6, p. 1129, 1995.

[4] Z. Song, C. Ong, and H. Gong, "A time-resolved current method for the investigation of charging ability of insulators under electron beam irradiation", *Journal of applied physics*, vol. 79, no. 9, pp. 7123–7128, 1996.

[5] H. Gong, Z. Song, and C. Ong, "Space-charge dynamics of polymethylmethacrylate under electron beam irradiation", *Journal of Physics: Condensed Matter*, vol. 9, no. 23, p. 5027, 1997.

[6] C. Ong, Z. Song, and H. Gong, "Dynamics aspects of the charging behaviour of polymers under focused electron beam irradiation", *Journal of Physics: Condensed Matter*, vol. 9, no. 43, p. 9289, 1997.

[7] F. Würthner, "Perylene bisimide dyes as versatile building blocks for functional supramolecular architectures", *Chemical communications*, no. 14, pp. 1564–1579, 2004.

[8] F. Würthner and A. Sautter, "Highly fluorescent and electroactive molecular squares containing perylene bisimide ligands", *Chemical Communications*, no. 6, pp. 445–446, 2000.

[9] R. S. Sánchez, R. Gras-Charles, J. L. Bourdelande, G. Guirado, and J. Hernando, "Light-and redox-controlled fluorescent switch based on a perylenediimide–dithienylethene dyad", *The Journal of Physical Chemistry C*, vol. 116, no. 12, pp. 7164–7172, 2012.

[10] J.-i. Niitsuma, H. Oikawa, E. Kimura, T. Ushiki, and T. Sekiguchi, "Cathodoluminescence investigation of organic materials", *Journal of electron microscopy*, vol. 54, no. 4, pp. 325–330, 2005.

[11] K. T. Arat, T. Klimpel, A. C. Zonnevylle, W. S. Ketelaars, C. T. H. Heerkens, and C. W. Hagen, "Charge-induced pattern displacement in e-beam lithography", *Journal of Vacuum Science & Technology B*, vol. 37, no. 5, 2019.

[12] R. Lane, Y. Vos, A. H. Wolters, *et al.*, "Optimization of negative stage bias potential for faster imaging in large-scale electron microscopy", *Journal of structural biology: X*, vol. 5, p. 100 046, 2021.

[13] A. Ul-Hamid, *A beginners' guide to scanning electron microscopy*. Springer, 2018, vol. 1.

[14] Lumiprobe. "3-ethynylperylene". (2023), [Online]. Available: `https://www.lumiprobe.com/p/3-ethynyl-perylene`.

[15] M. T. Haring, N. Liv, A. C. Zonnevylle, *et al.*, "Automated sub-5 nm image registration in integrated correlative fluorescence and electron microscopy using cathodoluminescence pointers", *Scientific Reports*, vol. 7, no. August 2016, p. 43 621, 2017, ISSN: 2045-2322. DOI: `10.1038/srep43621`. [Online]. Available: `http://www.nature.com/articles/srep43621`.

5

6

CONSIDERATIONS FOR ESRM

In Chapter 2, we discussed that eSRM relies on three factors: (a) causing a localized fluorescence decay, (b) detecting this decay over the background floor, and (c) accurately attributing the electron beam position to the associated decay for super-resolution (SR) reconstruction.

We assumed factor (a) based on well-accepted Monte Carlo simulations of electron-insulator interactions. Factor (b) was considered to be predominantly influenced by the fluorescent sample's signal-to-background ratio and the sensitivity of the light-optical detection system. Thus, eSRM implementation focused on achieving factor (c) while optimizing factor (b) using densely labeled fluorescent samples, high numerical aperture objectives, and sensitive sCMOS cameras. However, our experimental results digressed from (a) and (b), opening doors to investigate phenomena that formed the contents of Chapters 3 to 5. With these findings, we revisit the validity and considerations for eSRM.

ELECTRON BEAM INDUCED LUMINESCENCE IN EMBEDDING RESINS [CHAPTER 3]

We will address factor (b) first. The eSRM technique depends on accurately detecting electron beam-induced fluorescence decay over the background floor. This requires a sample with a high specific fluorescence photon yield (in a vacuum) coupled with a low background. Even with moderate signal photons, if the background is sufficiently low, commercially available scientific cameras can still register the intensity loss. During the development phase, the primary assumption was that the impact of the electron beam on the sample was limited to the localized bleaching of fluorophores. Therefore, the fluorescence image would not require spatial information for the eSRM measurement as long as the electron and light microscope coordinate systems were precisely aligned. The intensity in the entire fluorescent field of view would then drop each time a localized region of emitters is bleached and remain constant (within noise boundaries) otherwise. However, our experiments showed that the electron beam can also affect the background signal by inducing luminescence in the embedding resin as well as the biomaterial sam-

ple, either with or without resin.

The typical eSRM sample is one that finds application in integrated correlative light-electron microscopy CLEM. Biological samples, such as post-resin-embedding immuno-labeled tissue sections, are thus primary candidates. Investigations in Chapter 3 demonstrated that electron-induced luminescence occurs in all examined resins (epoxy and methacrylate variants), biomaterials (rat pancreas tissues, HeLa cells), and non-biological samples (styrene monomers, thermoplastic wires). In each case, electron-induced luminescence intensity increases, peaks, and bleaches with the cumulative electron fluence through the resin/material. The emission spectrum progressively broadens and redshifts, eventually spanning the measured range between 414 and 690nm. Minor variations are recorded based on specific resin/material properties, but the phenomenon persists. In order to monitor fluorescence loss with eSRM, it is essential to have a constant and low background. However, as electron irradiation continues to bleach fluorophores, the underlying sample begins to luminesce, resulting in a background with a spectrally varying intensity after each subsequent electron fluence deposition. Thereby compromising decay detection and subsequent SR reconstruction.

This can be mitigated in a few ways. Figure 3.2 in Chapter 3 showed that electron-induced luminescence is directly linked to the deposited fluence in the specimen. With very low electron fluences (reaching a maximum of 10^{-2}mC cm^{-2}), one can bypass its induction. However, this is impractical in an eSRM technique that relies on progressive electron irradiation for SR reconstruction and simultaneous electron imaging. Alternatively, induced luminescence ceases at fluences higher than 100mC cm^{-2}. However, this higher fluence causes long-range fluorescence bleaching, as seen in Chapter 5 (and discussed below), which forecloses eSRM. A possible solution is to utilize the spectral properties of electron-induced luminescence. For fluences below 5 mC cm^{-2}, there is negligible induced luminescence for orange-red excitations (561 or 633nm) (Figure 3.5 in Chapter 3), thus making low fluence examination and red-excitable fluorophores as suitable options for eSRM, irrespective of sample specifics.

Electron fluence deposition in the sample is dependent on the primary energy and the sample thickness. Higher energies that deposit most of the charge carriers in the sample support will, therefore, shift the induced luminescence spectrum to higher fluences. While this offers more room for electron irradiation without induced luminescence, it compromises localization. At 1keV primary energy, the distribution of secondary electrons and that generated by backscattered electrons, namely SE2s, is similar, thereby containing electron-induced luminescence impact to the scanned regions. The backscattered electrons and SE2s will have a broader distribution area at higher energies. With increasing fluence, the cumulative rise in fluence in these delocalized areas will incite luminescence. In addition, the sample density also influences induced luminescence. Regions with comparatively higher macromolecular density, such as the nucleus (both in tissue and whole cells), show locally higher induced luminescence intensity (Figures 3.6 and 3.7 in Chapter 3). Within flat tissue sections, these differences are unavoidable. However, this precludes using whole cells (with significant density gradients from center to end) for eSRM. Alternatively, discrete samples containing only the fluorescent regions, such as the polystyrene microspheres or microtubules (seen in

Chapter 2), could be suitable but limit the application portfolio of eSRM, particularly concerning EM-FM correlation.

Finally, HM20 shows the least electron-induced luminescence of the examined resins but comes at the cost of poorer sectioning compared to the epoxy variants. However, the differences between resins are minor, and the focus is better placed on choosing a vacuum-compatible high photon yield orange/red-emitting fluorophore while operating at low primary energy and electron fluence.

VACUUM COMPATIBLE FLUOROPHORES FOR INTEGRATED CLEM [CHAPTER 4]

Factor (b) necessitates high signal photon yield along with a low background. We addressed the latter above. The signal fluorophore must be orange/red-emitting for a low electron-induced luminescence background. In addition, the fluorophore must be compatible with vacuum conditions, with a high photon yield and low photobleaching rate. In Chapter 4, we investigated the photon yield and bleaching behavior of 5 common red-emitting fluorophores (Atto 655, Atto 647N, Alexa 647, Alexa 594, and TRITC) under standardly used SEM vacuum pressures of 3×10^{-5} to 7×10^{-7} mbar. Our results identify two dyes, Alexa 594 and TRITC, with higher photon yield and lower photobleaching in a vacuum. Notably, TRITC shows a three-fold increase in total photon yield and an approximately ten times longer half-life when exposed to the same excitation intensity (185 Wcm^{-2}) in a vacuum in comparison to ambient conditions. An integrated CLEM setup typically uses a multi-wavelength LED-based illumination system. It may not be feasible to double or triple the excitation intensity to push dormant molecules into an emissive state or increase signal photons. TRITC is thus particularly suitable for eSRM since it retains both the average number of emissive molecules and the initial photon count per molecule when pumped to vacuum pressures. Alexa 594 could be a good option to use alongside TRITC because its slow photobleaching rate can help compensate for the initial reduction in photon yield. These characteristics are particularly important for long eSRM experiments, where the entire fluorescent field of view is illuminated multiple times to generate the image series used for SR reconstruction.

FLUORESCENT REPORTERS FOR CHARGE TRANSPORT IN INSULATORS [CHAPTER 5]

Factor (a) is the primary requirement for an eSRM experiment. The electron bleaching range determines how localized the decay can be and, therefore, influences the final resolution that can be achieved in eSRM. eSRM relies on locally bleaching the fluorophores at the location of the electron beam. The interaction volume at low energies (<2keV) would not extend beyond 50nm from beam impingement. The consequent scattering and fluorophore bleaching would, therefore, remain localized within this region. This allows eSRM to use the electron beam as a nano-probe to switch off fluorophores within an area smaller than the optical diffraction limit. However, Chapter 2 revealed that fluorescence bleaching happens beyond the expected interaction volume.

A detailed investigation in Chapter 5 confirms this phenomenon in multiple insulator model systems. The bleaching range increases with the deposited charge contained in the specimen (extending to tens of micrometers), is not surface mediated, and is current-independent for the measured beam currents. To achieve a tightly localized

electron beam bleaching extent, it is recommended to use a 1keV landing energy electron beam with a low deposited charge that can achieve fluorophore bleaching and potentially generate electron contrast for real-time EM imaging. However, it is important to note that the fidelity of SR reconstruction may still be questionable. In Chapter 2, polystyrene microspheres could be localized with an accuracy of approximately 100nm (the set SR pixel size). This remained possible since the microspheres are heavily internally dyed and bleach relatively slowly until the probing electron beam hits them. However, the fidelity of SR reconstruction gets poorer the further the microsphere is in the scanning FOV.

With dedicated electron irradiation (i.e., selectively choosing to irradiate fluorescent regions and avoid the non-fluorescent regions to prevent unnecessary charge deposition), the effect can be mitigated to a certain extent in densely labeled isolated structures. However, single/few emitter localization in immunolabeled sections can be challenging. Even at low deposited charges, the fluorophore may bleach before the electron beam reaches its location. In the absence of long-range bleaching, fluorophore decay can be regarded as a false positive when the electron beam is known to be further away from the emitter than its diffraction-limited area. Due to the statistical nature of electron-induced (long-range) bleaching, there is always a chance that an emitter bleaches before direct electron irradiation, even when optimized for the smallest bleaching extent. This undermines the robustness of SR reconstruction. In the absence of electron contrast (like in insulin granules or polystyrene microspheres) for cross-confirmation, it is, therefore, impossible to determine false/missed localizations.

6

7

CONCLUSION

This thesis aimed to explore and utilize the fluorescent response to electron irradiation in integrated correlative light-electron microscopy (CLEM). Specifically, it aims to leverage the potential of integrated systems that can simultaneously perform electron microscopy (EM) and fluorescence microscopy (FM). Through the combined information from both modalities and central control over the experimental setup, the objective was to identify methods for manipulating and interpreting fluorescence data using the electron beam.

To that end, Chapter 2 introduced a super-resolution (SR) approach, termed eSRM, for application in an integrated CLEM system. The eSRM principle involves utilizing a focused electron beam to induce localized fluorescence bleaching. The resultant decrease in intensity is monitored in situ and can be attributed to the specific position of the electron beam that caused it. Chapter 2 presented the eSRM principle, detailed its implementation, and showcased proof of principle results on synthetic and biological model systems. Additionally, we demonstrated that an EM image could be generated in real-time while performing eSRM, which inherently registers the EM image to the resulting SR image. We employed a time-shared scanning method to increase throughput and reduce photobleaching. Our results revealed that while SR can be achieved, the electron beam influences the fluorescent sample in unexpected ways. It induces luminescence in resins and biomaterial, creating a spectrally varying background signal that is electron fluence dependent. Further, the electron beam bleaches fluorophores micrometers further from beam impingement, which is unexplained by the classical scattering volume in the material. In addition, while eSRM is generally applicable to any fluorophore that bleaches upon electron irradiation, we identified that certain fluorophores are particularly conducive to the oxygen and water-devoid vacuum environment in a scanning electron microscope. These findings prompted further investigation that is covered in the subsequent chapters.

In Chapter 3, we have spectrally (UV-Vis) characterized luminescence induced by

electron beam irradiation in commonly used embedding resins. We subjected two epoxy resins (Epon, Durcupan) and one methacrylate resin (HM20) to controlled electron irradiation over a wide electron fluence range, from 10^{-4} to 10^3 mC cm^{-2}, both with and without embedded biomaterial. We observed electron-induced luminescence in all three bare resins and biomaterial within the resin. Additionally, we observed luminescence in fixed, whole cells without resin. Across all samples, we reported a similar trend in luminescence: an initial increase, followed by redshifting, and finally bleaching with increasing fluence. We demonstrated that below 10^{-2} mC cm^{-2}, electron irradiation does not incite luminescence, and above 10^2 mC cm^{-2}, the emission is bleached. The induced luminescence development shifts to higher fluences for primary electron energies that predominantly scatter in the underlying substrate than in the resin/biomaterial specimen, indicating that the effect is mediated by the total deposited charge in the specimen. Our study also revealed that below an electron fluence of a few mC cm^{-2}, the induced luminescence spectrum is excited by UV-blue wavelengths, thereby allowing the possibility to spectrally bypass the effect by employing red-emitting fluorophores. With increasing electron fluence, the spectrum redshifts but also broadens to span the entire measured range between 414 and 690nm. Further, we recognized that regions with locally higher macromolecular density, such as the nucleus, can present with higher induced luminescence intensity for the same fluence, mimicking cellular contrast. Given that all examined polymer materials, whether natural or synthetic, exhibit similar electron-induced luminescence, we note that cathodoluminescence (CL) and CLEM applications must take this into account for probe selection and data interpretation. Also, since the phenomenon is highly tunable in terms of intensity and spectral behavior, it can serve to annotate specimens for CLEM and expand the range of available polymers that can be converted into luminescent nanostructures for use in materials science and nanophotonics applications.

Chapter 4 investigated the vacuum photon yield and photobleaching behavior of organic red-emitting fluorophores (ATTO 647N, Alexa 647, ATTO 655, TRITC, and Alexa 594) at the single-molecule level. We identified that TRITC excels in vacuum conditions, retaining its brightness and significantly improving photostability. This results in a three fold increase in photon count achievable in vacuum compared to ambient environments. While other dyes dim in a vacuum, for instance, Alexa 594 exhibits reduced photobleaching, contributing to an overall increase in detected photons. Moreover, both Alexa 594 and TRITC dyes show enhanced blinking and reduced off times when used in a vacuum setting. These findings hold promise for dye selection in integrated CLEM applications and potentially pave the way for integrating super-resolution fluorescence microscopy into integrated CLEM methodologies. Beyond integrated CLEM, in scenarios where an ambient or liquid environment isn't necessary—such as in nano- or quantum photonics—a vacuum environment at approximately 10^{-6} mbar coupled with the use of vacuum-optimized dyes could increase the obtainable photon budget.

In Chapter 5, we conducted experiments to investigate the electron-induced fluorescence bleaching effects extending beyond the expected interaction volume. We confirmed that long-range bleaching (in the order of tens of micrometers) occurs in multiple insulator model systems, using varying sample architecture and detection methods. The spatial bleaching extent grows radially outward with increasing deposited charge

and is independent of the rate of charge deposition. However, the electron beam size spot affects the bleaching range. As the spot size decreases, the bleaching range increases, which is particularly noticeable between immersion and field-free lens modes, suggesting the influence of field-driven charge migration. We further showed that the long-range bleaching phenomenon is not surface-mediated, mainly occurs in the specimen bulk, and is unaffected by introducing beam deceleration. Beam deflection and primary beam defocus related to charging have also been ruled out as causative agents. Based on our findings, we propose that fluorophores could act as uniquely sensitive reporters, offering a new, real-time experimental method to study electron-irradiation-induced charge carrier transport in insulators.

Chapter 6 combines the results from the investigations in Chapters 3 to 5 to discuss implications for the eSRM method presented in Chapter 2. We note that the eSRM technique is best demonstrated with densely labeled, isolated samples like the fluorescent polystyrene microspheres, followed by thin, flat, immunolabeled tissue sections. In the latter, the impact of electron-induced luminescence from the embedding resin or surrounding biomaterial can be mitigated by low electron fluence irradiation and using red-emitting fluorophores, for which TRITC is an excellent choice. Despite such optimization, the electron-induced bleaching range determines the ultimate resolution achievable by eSRM. The long-range bleaching phenomenon detailed in Chapter 5 can be limited by restricting electron irradiation to low deposited charges. However, in the absence of electron contrast, the fidelity of SR reconstruction cannot be ascertained, thereby limiting the potential of eSRM for meaningful super-resolution FM and consequent EM correlation.

7

ACKNOWLEDGEMENTS

This PhD journey has been a formative phase in my life, and I am grateful to many people for their support along the way. Firstly, my promotors. Jacob, thank you for welcoming me into the group and for your kind guidance over the years. I've always appreciated the research freedom you gave me, your keen eye for scientific writing, and, more importantly, your support through the hurdles (both experimental and otherwise). Pieter, I have indeed learned a great deal about physics from you. But what I have also learned is to put on a rational thinking hat while examining life and society. Thank you for the discussions; it has been a privilege. Kees, even while not directly involved, I deeply appreciate the interest you took in my life, the project, and the completion of this thesis.

I started this work with immense help from Lennard Voortman, who laid the foundation for the experimental implementation of eSRM. I am grateful to the Delmic team, Eric and Andries, for their crucial technical insights and to Sander for his support throughout. A special mention to our collaborators, Pascal, Anouk, Ben, and the UMCG team. Our collective work has been a pleasure, and meeting the team has been a highlight at each Dutch BioPhysics meeting. I appreciate the valuable feedback from the TTW steering committee, particularly Hans Gerritsen. Many thanks to Christiaan and Bernd; it was great to collaborate on the photobleaching project. Thanks also goes to Vladimir for the microtubule samples.

I am grateful to the numerous CPO (now MINT) colleagues who fostered my personal and scientific growth. As I write this, I realize that I need to thank many people twice, once professionally and once, for the friendships that resulted from this.

Kerim, your strong work ethic is only surpassed by your brotherly kindness. I still have that plastic pouch to put my water-damaged passport in. Wilco, what an excellent, fearless engineer you are. Our first collaboration was in quietly 'borrowing' a table fan from Pieter's office to 'cool' the camera while avoiding vibrations (which Anjella quickly reclaimed). It's a shame it worked, as did many other rogue experiments. Without your transmission imaging help, I might have been convinced I was imagining the long-range bleaching. Much of the first year was spent troubleshooting the SEM (it clearly continued for many years after), for which Gman, you gave me company in the evenings and the weekends. I loved having a friend to speak Tamil with, going on fruitless shopping trips, and discussing all things Tamil cinema and culture. Together with Sangeetha and Shammi, we had a lovely Indian community to be part of. Thank you all (and Naren) for the many invitations home, great food, and conversations. Life's (been) good in CPO, thanks to Gerward - it's always fun when you come to visit us. Robert, thank you for your friendship and all kinds of optics help. Together, our Friday dinners were the perfect end to the work week (until Wilco hijacked it and replaced it with Locus). From EMC Lyon (where we both failed to cook an egg) to discussing corporate life and being parents, I

CURRICULUM VITÆ

Aditi SRINIVASA RAJA

21-02-1990   Born in Chennai, India.

EDUCATION

2007–2011   B.Tech. Biomedical Engineering
                        SRM University, Chennai, India

2013–2015   MSc. Optics & Photonics
                        Karlsruhe Institute of Technology, Germany
                        Aix-Marseille University, France

2016–2024   PhD. Applied Physics
                        Delft University of Technology, The Netherlands

WORK HISTORY

2021–2024   Applications Engineer
                        ASML, The Netherlands

LIST OF PUBLICATIONS

5. **Srinivasa Raja, A. , Vos Y. et al.**, *Fluorescent reporters for charge transport in insulators, Manuscript in preparation.*

4. **Srinivasa Raja, A. , Hulleman, C.N. et al.**, *Single-molecule fluorophore behavior under vacuum conditions, Manuscript in preparation.*

3. **Srinivasa Raja, A. , de Boer, P. , Giepmans, B.N.G. & Hoogenboom, J.P.** , *Electron-Beam Induced Luminescence and Bleaching in Polymer Resins and Embedded Biomaterial*, Macromolecular Bioscience 21, No 11,2100192 (2021).

2. **Hoogenboom, J.P. , Srinivasa Raja, A. , den Hoedt, S.V. & Lane, R.I.**, *Method for integrated acquisition and registration of large-scale microscopy image data*, Patent:OCT-19-014 (2021).

1. **Koning, R.I.,Srinivasa Raja, A., Lane, R.I., Koster, A.J., & Hoogenboom, J.P.**, *Integrated light and electron microscopy* , Correlative Imaging: Focusing on the Future, 119-135 (2015).